FERMILAB-THESIS-2022-16

Sterile Neutrino Search with the NOvA Detectors

by

Harry R. Hausner

A dissertation submitted in partial fulfillment of
the requirements for the degree of

Doctor of Philosophy

(Physics)

at the

UNIVERSITY OF WISCONSIN–MADISON

2022

Date of final oral examination: 08/23/2022

The dissertation is approved by the following members of the Final Oral Committee:
Brian Rebel, Professor, Physics
Kevin Black, Professor, Physics
Keith Bechtol , Assistant Professor, Physics
Ellen Zweibel, Professor, Astronomy

To Miranda, whose love has kept me going

Acknowledgments

> *There is no royal road to science, and only those who do not dread the fatiguing climb of its steep paths have a chance of gaining its luminous summits.*
>
> — Karl Marx (1872)

Science is the processes in which the accumulated knowledge of generations is distilled to tackle new problems. As such no scientific result can ever be attributed to a sole scientist. This work is no exception. While what follows is the fruit of my research none of it would have been possible without the help and support of my friends and mentors.

Firstly I would like to thank the whole of the NOvA Collaboration. It should go without saying that there can be no analysis without data, and there would be no data without the tireless work of the entire Collaboration working to ensure the NOvA detectors function around the clock. Every scientist on NOvA spends time monitoring the detectors for anything which would interrupt data collection, and so every NOvA collaborator has played a part in making this research possible.

Additionally many in the NOvA Collaboration took the time to personally advise me my research as it progressed. In particular the conveners of the NuX working group, Professors Adam Aurisano, Gavin Davies, and my PhD supervisor Brian Rebel, were invaluable in helping me along the path to this dissertation. The feedback I received during the NuX group meetings prevented me from going down many wrong roads and point me in better directions.

At the University of Wisconsin–Madison, the postdocs in my research group, Doctors Thomas Carroll and Adam Lister, provided much needed advice in how to become a career scientist, and wisdom in how to survive in a PhD program. Professor Jennifer Thomas provided great feedback on my work during group meetings and gave me the amazing opportunity to get a hands-on experience helping to assemble the CHIPS detector in Hoyt Lakes, Minnesota.

My friends deserve thank for keeping me sane during these past years. Joel Siegel, Andrew Loeliger, Jocelyn Bock, Shoshana Rudin, and Michael Cervia all help remind me that there was beauty that lay outside of physics, and their companionship brought me countless hours of joy.

Finally, I would not be here without the love and support of my family. In particular my wife Miranda, who has been by my side throughout this entire process.

Contents

Contents iv

List of Tables vii

List of Figures viii

Abstract xxii

1 Introduction 1

1.1 *Proposal & Discovery* 1

1.2 *Standard Model* 3

1.3 *Solar Neutrino Problem* 5

1.4 *Atmospheric Neutrino Problem* 7

1.5 *Evidence of Neutrino Oscillations* 9

1.6 *Beyond Standard Oscillations* 11

1.7 *Personal Contributions to the Analysis* 12

2 Neutrino Oscillations 13

2.1 Oscillations in Vacuum 14

2.2 Oscillations in matter 33

2.3 Analysis Phenomenological Framework 41

3 The NOvA Experiment 42

3.1 The NuMI Beam 43

3.2 The NOvA Detectors 46

4 Energy Calibration 51

4.1 Standard Candle 52

4.2 Event Selections 55

4.3 Tricell Method 57

4.4 Trajectory Method 59

4.5 Method Comparisons 59

4.6 Applying the Calibration 64

5 Event Selection 74

5.1 Neutral Current Selection 76

6 Neutral Current Event Energy Estimation 94

6.1 Candidate Energy Estimators 96

6.2 Summary 120

7 Covariance Matrix Fitting 123

7.1 Principals of Covariance 125

7.2 Covariance Matrix Generation 131

7.3 Covariance Matrix Test Statistic 133

7.4 Covariance Matrix In Use 136

7.5 Data Fit 143

8 Conclusion 148

Colophon 150

Bibliography 151

List of Tables

7.1 Oscillation parameters varied to create the library of predicted spectra for the four-flavor analyses [48]. The points for Δm^2_{41}, θ_{24}, and θ_{34} are evenly spaced in $\log(\Delta m^2_{41})$, $\log(\sin^2\theta_{24})$, and $\log(\sin^2\theta_{34})$. The points for the remaining parameters are evenly spaced within each range. The degenerate values of θ_{23} are only used in the region of parameter space where $\sin^2\theta_{24} > 0.1$ and $\Delta m^2_{41} < 0.01\,\mathrm{eV}^2$. 137
7.2 The number of events predicted in each sample under the three flavor model and the number of observed events in data. Note that we do not have the number of cosmic background events in the data as such events would be part of the data samples. . . . 146
7.3 The parameters obtained from the best fit of the data spectra. . 146

List of Figures

1.1 An example of a Charged Current interaction. 5

1.2 An example of a Neutral Current interaction. 5

2.1 The probability of measuring a ν_β of energy E a distance $L = 810\,\mathrm{km}$ away from a ν_β source. This figure assumes two flavor mixing with a mixing angle of $\theta = \pi/4$ and a mass-squared splitting of $\Delta m^2_{21} = 2.5 \times 10^{-3}\,\mathrm{eV}^2$. The probability oscillates rapidly as the neutrino's energy approaches zero. 22

3.1 A schematic diagram of the NuMI beam which shows the target, magnetic horns, decay pipe, and absorbers [24]. 44

3.2 A schematic diagram of a single NOvA cell. Shown in green is the wavelength shifting fiber contained in the scintillation mixture. The width W and depth D are 3.56 cm and 5.59 cm respectively, while the length L depends on which detector the cell is in. For the ND $L = 3.9$ m and $L = 15.5$ m for the FD. Also shown is the scintilation light (blue) generated by a charged particle (black dashed) traveling through the cell [28]. 48

4.1 The stopping power of benzene on an impinging muon as calculated using equation (4.1). The parameters for the Bethe-Bloch equation were taken from the Particle Data Group [16]. 53

4.2 The stopping power of benzene on an impinging muon, obtained using equation (4.1), as a function of distance from the end of the muon's track, L. The distance was obtained by numerically integrating (4.1). 55

4.3 A schematic depiction of a cell hit valid for the tricell method within a y-plane. By requiring activity to occur in all three red cells, we know that the muon must have crossed the two walls of the dark red cell, which are on separated by the interior cell width L_y, which is on average 3.56 cm, and the path through the cell can be estimated as $L = L_y/c_y$. The activity in the dark red cell is then suitable for the tricell calibration. [30] 58

4.4 A diagram illustrating the trajectory reconstruction. Here a muon is reconstructed as having passed through the location p_1 inside a cell, and p_2 is the subsequent trajectory point. The trajectory reconstruction draws the line containing p_1 and p_2 and estimates the muon path length in the cell consisting of the segment of that line contained withing the walls of the cell. This segment is shown in red on the diagram. Note that the trajectory point p_0 which precedes p_1 does not factor into the reconstruction. 60

4.5 The ratio of the number of simulated cell hits in the NOvA Far Detector which can be reconstructed with the trajectory to the numberused with the tricell method. Each bin corresponds to one cell specified by the location of the cell in the plane and the plane in the detector. 61

4.6 The fractional difference in the the path reconstruction as a function of reconstructed path with the tricell method for x-view cells (a) and y-view cells (b). The black lines show the mean error for each length. Note there are no tricell hits with a path less than 3.56 cm as the reconstruction is limited by the physical widths of the cells. 62

4.7 The fractional difference in the the path reconstruction as a function of reconstructed path with the trajectory method for x-view cells (a) and y-view cells (b). The black lines show the mean error for each length. 63

4.8 The number of simulated cell hits which can be used for calibration as a function of the reconstructed path reconstruction as a function of reconstructed path length with the trajectory method for x-view cells (a) and y-view cells (b). Note there are no tricell hits with a path less than 3.56 cm as the reconstruction is limited by the physical width of the cells. 65

4.9 The average detector response for the ND (a) and FD (b), separated into x—view (red) and y—view cells (blue). Note that detector response is higher for large w as we a closer to the cell readout [32]. 67

4.10 Average threshold and shielding correction factor T as a function of position in the cell w. The red curves show are average over all x-view cells, while the blue is averaged over y-view cells. Note that low w corresponds to the end of the cell farthest from the readout, and so those ends require a stronger correction to deal with threshold effects [32]. 69

4.11 An example of the attenuation fit for ND cell 81 in plane 48. The dashed lines show the physical boundaries of the cell. Note that as the distance from the center of the cell, w, is a reconstructed quantity some cell hits are reconstructed with unphysical w. The red curve shows the result of fitting the data with Equation (4.5) for $-150\,\mathrm{cm} < w < 150\,\mathrm{cm}$. The ratio of the data to red curve is then fit with a twenty point tri-cubic local regression to obtain a second order correction. The full fit including this correction is shown in blue [32]. 71

4.12 The distribution of reconstructed $\frac{\mathrm{d}E}{\mathrm{d}x}$ for tricell hits in the penultimate meter of a stopping muon track for data (black) and MC (red) in the ND (a) and FD (b) [33]. The plots have been normalized so there are the same number of events in the data and MC. The data and MC agree on the mean of the distributions to within 2% for both detectors [34]. 72

5.1 Comparisons of data and simulation for the ND quality requirements. The true NC events are highlighted in blue, and the removed regions are shown as grey boxes. The simulation is normalized to have the same number of events as the data. 78

5.2 Comparisons of data and simulation for the ND vertex positions, with the NC signal events in blue. Note that the simulation has been normalized to match the number of events in the data. The removed regions are shown as grey boxes. These plots have the quality requirements outlined in §5.1.1.1 already applied. 80

5.3 The average fraction of $\mathrm{E}_{\mathrm{vis}}/\mathrm{E}_{\mathrm{dep}}$ in our ND simulation as a function of the minimum distance of the prongs from each detector edge. Note that there are negative values of the prong distance to edge due to errors in the prong reconstruction. 82

5.4 Comparisons of data and simulation for the minimum distance of any prong to each detector edge. Here, the true NC events are in blue, and the removed regions are shown as grey boxes. Note that the simulation has been normalized to have the same number of events as the data. In these plots, the event quality requirements of §5.1.1.1 and vertex position demands have been applied. 83

5.5 Comparisons of data and simulation for the CVN score for the ND. Here, the true NC events are in blue, and the removed region is shown as a gray box. Note that the simulation has been normalized to have the same number of events as the data. These plots have the event quality and containment requirements applied as outlined in §5.1.1.1 and §5.1.1.2 respectively. 84

5.6 Distributions for the variables used in the FD event quality requirements. The true NC events are highlighted in blue, and the removed regions are shown as grey boxes. 85
5.7 The average fraction of E_{vis}/E_{dep} in our FD simulation as a function of the minimum distance of the prongs from each detector edge. Note that there are negative values due to errors in the prong reconstruction. 87
5.8 Distributions for the minimum distance of any prong to each edge of the FD. Here, the true NC events are in blue, and the removed regions are shown as grey boxes. In these plots, the quality requirements of §5.1.2.1 have been applied. 88
5.9 Variables 1 through 7 and 14 used in the BDT training. These distributions are normalized to have one event and have requirements described in §§5.1.2.1-5.1.2.2 applied to them. 90
5.10 Variables 8 through 13 used in the BDT training. These distributions are area normalized and have requirements described in §§5.1.2.1-5.1.2.2 applied to them. 91
5.11 Distributions for the FD CVN and cosmic rejection BDT scores. Here, the true NC events are in blue, the cosmic background events are shown in orange, and the removed regions are shown as grey boxes. These events have the requirements described in §§5.1.2.1-5.1.2.2 applied to them. 93

6.1 The distribution of $\Delta E_{\text{dep,cal}}/E_{\text{dep}}$, for true NC events passing the full selection and having an interaction vertex inside the detector for the ND (blue) and FD (red). An accurate, unbiased estimator would result in a symmetric distribution peaked at zero. Clearly, E_{cal} underestimates E_{dep}. 97

6.2 Distributions of simulated events showing E_{dep} as a function of E_{cal} for the ND (left) and FD (right). The black points are $\langle E_{\text{dep}}\rangle$ for each bin of E_{cal}, and the red lines are the linear fits to these averages. The fits are performed over the range of 0 to 10 GeV. The fit in the ND is $\langle E_{\text{dep}}\rangle_{\text{ND}} = (0.034 \pm 0.001)\,\text{GeV} + (1.168 \pm 0.001) \times E_{\text{cal}}$, and the fit in the FD is $\langle E_{\text{dep}}\rangle_{\text{FD}} = (0.070 \pm 0.001)\,\text{GeV} + (1.170 \pm 0.001) \times E_{\text{cal}}$. 100

6.3 Distributions of $\Delta E_{\text{dep,L}}/E_{\text{dep}}$ for the ND and FD events dominated by electromagnetic energy (top) and events dominated by hadronic energy (bottom). 101

6.4 The distribution of of the $\Delta E_{\text{dep,cal}}/E_{\text{dep}}$ in the ND. The sample is split into events which produce at least one neutron in the final state (red) and those which have none (blue). Also shown is the split into events with $E_{\text{Orph}} < 0.01$ GeV (cyan) and events with $E_{\text{Orph}} > 0.01$ GeV (magenta). 103

6.5 Distributions of simulated ND events with $E_{\mathrm{Orph}} < 0.01\,\mathrm{GeV}$ (left) and $E_{\mathrm{Orph}} > 0.01\,\mathrm{GeV}$ (right). The black points are $\langle E_{\mathrm{dep}} \rangle$ vs E_{cal}, and the red lines are the linear fits to these averages, with a fit range of 0 to 2 GeV for $E_{\mathrm{Orph}} < 0.01\,\mathrm{GeV}$ and a fit range of 0 to 10 GeV for $E_{\mathrm{Orph}} > 0.01\,\mathrm{GeV}$. The fit is $\langle E_{\mathrm{dep}} \rangle = (0.211 \pm 0.002)\,\mathrm{GeV} + (0.905 \pm 0.002) \times E_{\mathrm{cal}}$ for $E_{\mathrm{Orph}} < 0.01\,\mathrm{GeV}$, and $\langle E_{\mathrm{dep}} \rangle = (0.062 \pm 0.001)\,\mathrm{GeV} + (1.189 \pm 0.001) \times E_{\mathrm{cal}}$ for $E_{\mathrm{Orph}} > 0.01\,\mathrm{GeV}$. 104

6.6 Distributions of simulated FD events with $E_{\mathrm{Orph}} < 0.01\,\mathrm{GeV}$ (left) and $E_{\mathrm{Orph}} > 0.01\,\mathrm{GeV}$ (right). The black points are $\langle E_{\mathrm{dep}} \rangle$ vs E_{cal}, and the red lines are the linear fits to these averages, with a fit range of 0 to 2 GeV for $E_{\mathrm{Orph}} < 0.01\,\mathrm{GeV}$ and a fit range of 0 to 10 GeV for $E_{\mathrm{Orph}} > 0.01\,\mathrm{GeV}$. The fit is $\langle E_{\mathrm{dep}} \rangle = (0.205 \pm 0.004)\,\mathrm{GeV} + (0.971 \pm 0.004) \times E_{\mathrm{cal}}$ for $E_{\mathrm{Orph}} < 0.01\,\mathrm{GeV}$, and $\langle E_{\mathrm{dep}} \rangle = (0.100 \pm 0.001)\,\mathrm{GeV} + (1.167 \pm 0.001) \times E_{\mathrm{cal}}$ for $E_{\mathrm{Orph}} > 0.01\,\mathrm{GeV}$. 105

6.7 Distribution of $\Delta E_{\mathrm{dep,Est}}/E_{\mathrm{dep}}$, where E_{Est} is either E_{L} or E_{O}, for ND events with $E_{\mathrm{cal}} < 2\,\mathrm{GeV}$ using the linear estimator (blue) and the orphaned energy estimator (red). 106

6.8 Distribution of $\langle E_{\mathrm{dep}} \rangle$ (on the color scale) as a function of E^{r}_{EM} and E^{r}_{Had} for the ND (left) and FD (right). 108

6.9 Distributions of the number of events (on the color scale) for the ND (left) and FD (right). The color axis is capped at 20 events so that dark red bins have at least 20 events. The fit of $\langle E_{\rm dep} \rangle$ vs $E^{r}_{\rm EM}$ and $E^{r}_{\rm Had}$ is done only for bins with at least 20 events. 108

6.10 Distributions of $\Delta E_{\rm dep,cal}/E_{\rm dep}$ for electromagnetic energy dominated events (top row) and hadronic energy dominated events (bottom row), for the ND (left column) and FD (right column). In red are Gaussian fits to the region above 75% of the maximum value. The means from the Gaussian fits are used to obtain correction factors to scale $E^{r}_{\rm EM}$ and $E^{r}_{\rm Had}$ to better match the deposited energy. The results of the fit indicate that electromagnetic energy dominated events tend to be overestimated by $(4.9 \pm 0.3)\%$ in the ND and $(2.5 \pm 0.3)\%$ in the FD, while the hadronic energy dominated events are underestimated by $(20.5 \pm 0.2)\%$ and $(20.3 \pm 0.1)\%$ in the ND and FD respectively. 110

6.11 The distribution of $\Delta E_{\rm dep,S}/E_{\rm dep}$ for ND events with $E_{\rm cal} < 2.5$ GeV. In red is the Gaussian fit to the distribution in the region above 90% of the maximum value of the distribution. The mean from this Gaussian fit is 4.5%. 111

6.12 The biases in $E_{\rm cal}$ (top), $E_{\rm L}$(middle left), $E_{\rm O}$ (middle right), $E_{\rm Q}$ (bottom left), and $E_{\rm S}$ (bottom right) for ND events. In red are the best fits of the biases to the function defined in equation (6.13). . 112

6.13 The biases in E_{cal} (top), E_L(middle left), E_O (middle right), E_Q (bottom left), and E_S (bottom right) for FD events. In red are the best fits of the biases to the function defined in equation (6.13). . 113

6.14 The biases in E_{Est} for the calorimetric, linear, orphaned energy, quadratic, and scaling estimators for ND (top) and FD (bottom) events. Also shown is the cumulative fraction of events bellow E_{cal}, shown with the dashed line. 115

6.15 The remaining biases in E_{Est} after bias correction for the calorimetric, linear, orphaned energy, quadratic, and scaling estimators for ND (top) and FD (bottom) events. Also shown is the cumulative fraction of events bellow E_{cal}, shown with the dashed line. The inlays show a zoomed in view of the region $E_{\text{cal}} < 3\,\text{GeV}$. 119

6.16 Distributions of $\Delta E_{\text{dep,Est}}/E_{\text{dep}}$ for the bias corrected calorimetric, linear, orphaned energy, quadratic, and scaling estimators for ND (top) and FD (bottom) events. 121

7.1 The value of $\sin^2\left(\Delta m^2_{41}\frac{Lc^3}{4E\hbar}\right)$ at the distance of the NOvA ND, $L = 1\,\text{km}$, for the energy peak of the neutrino beam, $E_\nu \approx 1.8\,\text{GeV}$. For $\Delta m^2_{41} \lesssim 0.5\,\text{eV}^2/\text{c}^4$ the term is negligible and we can ignore sterile oscillations in the ND. Larger values of Δm^2_{41} necessitate accounting for oscillations in the ND. 124

7.2 Example distributions with different values of $\mathrm{Cov}(X, Y)$. Each point shows the values x_i and y_i from a single experiment. Figure 7.2a has $\mathrm{Cov}(X, Y) = 0.110453$, Figure 7.2b has $\mathrm{Cov}(X, Y) = -0.166053$, and Figure 7.2c has $\mathrm{Cov}(X, Y) = 0.000986901$. 127

7.3 An example of data distibuted about the circle $X^2 + Y^2 = 1$. Each point shows the values x_i and y_i from a single experiment. The X and Y variables have no relation and have a covariance of -0.00143745. 129

7.4 The logically binned spectrum for the Asimov spectra generated with nominal three flavor oscillation parameters. Bins 0 to 18 are bins for the ND ν_μCC selection, 19 to 33 are the ND NC selection, 34 to 52 are for the FD ν_μCC selection, and 53 to 66 are for the FD NC selection. 132

7.5 The total fractional covariance matrix. The solid lines separate the ND bins (left/down) from the FD bins (right/up). The dashed lines divide the ν_μCC and NC events in each detector with the former on left/lower side and the later on the right/upper side. . 134

7.6 The 90% confidence level contour and $\Delta\chi^2$-values for a fake data spectrum without sterile neutrinos. The color scale shows the value of $\Delta\chi^2$ for each point of $\sin^2\theta_{24}$-Δm^2_{41} from the values in Table 7.1. The black line is the Wilks' 90% confidence level contour. 138

7.7 The median 90% confidence level contour and $\Delta\chi^2$-values from 500 statistically and systematically fluctuated fake data spectra without sterile neutrinos. The color scale shows the value of $\Delta\chi^2_{\text{Median}}$ for each point of $\sin^2\theta_{24}$-Δm^2_{41} from the values in Table 7.1. The black line is the Median 90% confidence level contour drawn from the median value of $\Delta\chi^2$ at each grid point. 139

7.8 The median 90% confidence level contour and the number of statistically and systematically fluctuated fake data spectra without sterile neutrinos for which that grid point is allowed within the Wilks' 90% confidence level. The black line is the Median 90% confidence level contour drawn from the median value of $\Delta\chi^2$ at each grid point. 140

7.9 Averaged probability that muon neutrinos do not oscillate to the sterile flavor for $\Delta m^2_{41} = 0.05\,\text{eV}^2/\text{c}^4$, $0.5\,\text{eV}^2/\text{c}^4$, and $5\,\text{eV}^2/\text{c}^4$. The probabilities are averaged over the neutrino energy to mimic the effect of our limited energy resolution. Note that the probabilities are nearly identical in the region of L/E_ν that the FD sees. Image courtesy of the NOvA Collaboration. 142

7.10 The data spectra for this analysis. Note that the ν_μCC spectra are normalized by the 0.1 GeV bin width while the NC spectra are normalized by a 1 GeV bin width. Additionally the NC spectra are presented with the energy on a logarithmic scale. 144

7.11 The data spectra for the ND/FD ν_μCC/NC selection. These spectra are compared to MC generated with the best fit oscillation parameters. Because our method does not fit for systematic parameters the MC was generated with the central values for all systematic parameters. 145

7.12 The Wilkes' Theorem 90% C.L. contours from our data fit and the location of the best fit point. The region to the right of the contour is excluded at the 90% confidence level apart from the region near $\sin^2(\theta_{24}) = 0.4, \Delta m^2_{41} = 5 \times 10^{-3}\,\mathrm{eV}^2/c^4$. This island of inclusion is due to the potential for degeneracy between Δm^2_{41} and Δm^2_{32}. 147

Abstract

NOvA is a two-detector experiment designed to observe neutrino oscillations from ν_μ to ν_e flavor states. Additionally, the location of the NOvA Near Detector is well situated to additionally observe short baseline oscillations to sterile neutrino states. We expand upon previous NOvA sterile neutrino searches by using a covariance matrix fitting technique. This analysis is the first with NOvA to directly include neutrino interactions in the Near Detector while fitting the data. The NOvA Near Detector's greater statistics to better constrain our Far Detector uncertainties in addition to increasing the range of Δm^2_{41} to which we are sensitive.

Chapter 1

Introduction

1.1 Proposal & Discovery

The history of the neutrino is as much about its absence as it is its existence. First conceived by Wolfgang Pauli in 1930, the neutrino was purposed to explain why observed beta decays did not obey our standard laws governing the conservation of energy, momentum, and angular momentum. At the time, beta decay was understood as a nucleus N, converting a neutron to a proton (or vice versa) via emitting an electron (positron), $e^{-(+)}$,

$$\mathrm{N} \rightarrow \mathrm{N}' + e^{-} \quad \text{or} \quad \mathrm{N} \rightarrow \mathrm{N}' + e^{+}. \tag{1.1}$$

However, it was observed that in the decay, the daughter nucleus and electron had less energy than the parent nucleus. Furthermore, the missing energy could take on any value along the continuum bounded by zero and the difference in the rest energy of N and $\mathrm{N}' + e^{-(+)}$. As there were no other particles observed in the decay, this seemed to be a violation of the well established law of conservation of energy. Pauli, rather than giving up conservation of energy, proposed that there was an undetected, electrically neutral particle produced in beta decay which would account for the missing energy. The proposed decays,

$$\mathrm{N} \to \mathrm{N}' + e^- + \bar{\nu} \quad \text{or} \quad \mathrm{N} \to \mathrm{N}' + e^+ + \nu, \tag{1.2}$$

were the first introduction of the (anti-)neutrino, $\nu(\bar{\nu})$ [1].

Despite this tidy explanation, the neutrino remained undetected for over twenty years after it was first proposed. It took until 1956, when Project Poltergeist, headed by Frederick Reines and Clyde Cowan, announced the detection of neutrinos produced in a nuclear reactor [2]. To detect the neutrinos, the collaboration behind Project Poltergeist placed a tank of water doped with cadmium chloride near the reactor. The neutrinos produced in the nuclear processes in the reactor were captured in the inverse of the beta decay described in Equation (1.2). The neutrino is captured by a proton, which converts into a neutron with the emission of a positron:

$$p + \bar{\nu} \to n + e^+. \tag{1.3}$$

The positron would quickly annihilate with an electron, emitting two 0.5 MeV photons in opposing directions. Additionally, the neutron would be absorbed by the cadmium, which would then emit a photon 5×10^{-6} s later. The photons were detected by photomultiplier tubes which surrounded the tank, and the signal of two 0.5 MeV photons followed by a second photon 5×10^{-6} s later was proof of a neutrino interaction.

1.2 Standard Model

Neutrinos now form a core component of what is known as the Standard Model (SM) of particle physics [3]. In the Standard Model, there are three *flavors* of neutrinos. Each flavor of neutrino is associated with an electrically charged particle of the same flavor: the electron (e^-), the muon (μ^-), and tau (τ^-) are associated with the electron neutrino, muon neutrino, and tau neutrino which are labeled as ν_e, ν_μ, and ν_τ respectively. Together these six particles are called *leptons*. The leptons are also joined by their antimatter doppelgängers the positron (e^+), the anti-muon (μ^+), anti-tau (τ^+), the electron anti-neutrino ($\bar{\nu}_e$), muon anti-neutrino ($\bar{\nu}_\mu$), and tau- anti-neutrino ($\bar{\nu}_\tau$).

In the Standard Model neutrinos are massless, electrically neutral particles which interact only via the Weak Force, which derives its name from the low strength of its interactions. As neutrinos are only sensitive to the Weak Force, and are unaffected by the other two fundamental forces described by the Standard Model, the Electromagnetic and Strong Forces, they interact very rarely. In fact, neutrinos interact so rarely that despite over trillions of solar neutrinos passing through your body every second, it is unlikely that more than one will ever interact [4].

Neutrino interactions can be divided into two categories: *charged current* (CC) and *neutral current* (NC). Charged current interactions proceed by the exchange of a charged boson, either the W^+ or the W^-, and can convert a neutrino into a charged lepton or a charged lepton into a neutrino. Neutral current interactions preserve the type of the leptons involved and are governed by the exchange of a neutral Z^0 boson. Examples of CC and NC interactions can be found in Figures 1.1 and 1.2 respectively.

Importantly, neither CC nor NC interactions can change the flavor of a lepton. If, for example, a neutrino scatters off of an electron, then the Standard Model dictates that the outgoing neutrino must be of the same flavor as the original. Since Standard Model neutrinos only interact via these two interaction modes, the flavor of a neutrino will never change.

Yet the Standard Model has not been the final word on the physics of neutrinos. Since their discovery, there have been numerous experiments probing the properties of neutrinos, many of which have challenged the foundations of the Standard Model.

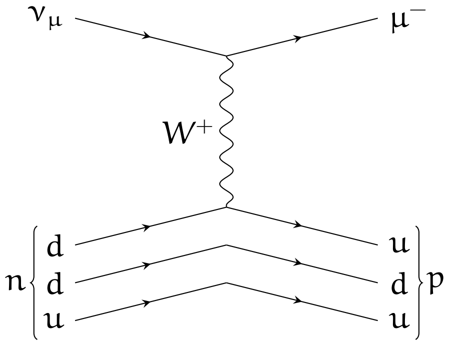

Figure 1.1: An example of a Charged Current interaction.

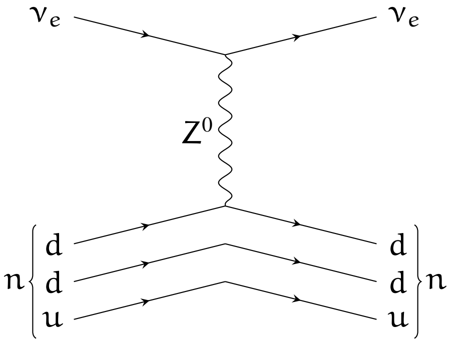

Figure 1.2: An example of a Neutral Current interaction.

1.3 Solar Neutrino Problem

The first detection of neutrinos opened up the scientific community to a whole range of experiments to look for neutrinos. As neutrinos are produced in nuclear reactions, researchers sought out natural nuclear reactors. This lead them to look for neutrinos produced by the Sun. The amount of solar neutrinos which reach the Earth per second per square-meter, the *solar neutrino flux*, can be predicted from our understanding of the Sun: from the temperature and pressure of the Sun's core, we can estimate the rate of nuclear processes in the Sun which produce neutrinos. From this production rate we can readily calculate what fraction of those will reach some surface area on Earth.

In 1964, John Bahcall had modeled the solar neutrino flux and determined that the reaction

$$\nu_e + {}^{37}\mathrm{Cl} \rightarrow {}^{37}\mathrm{Ar} + e^- \tag{1.4}$$

would be sensitive to the energies of solar neutrinos, predicting there would be $(4 \pm 2) \times 10^{-35}\,\mathrm{Sec}^{-1}$ neutrinos captured per atom of chlorine [5]. An experiment set up by Ray Davis in the Homestake mine in South Dakota, consisting of a 380 cubic meter tank of perchloroethylene (Cl_2C) 1487 meters underground, was determined to have low enough backgrounds to be capable of measuring this flux [6]. By extracting the argon atoms every few weeks, the rate of solar neutrino interactions could be measured.

However, the Homestake experiment measured only one third as many solar neutrinos as were expected from Bahcall's model. At first this deficit was thought to be due to a mismodeling of the Sun, but that idea was ruled out by other measurements. The mystery behind the dearth of solar neutrinos became known as the Solar Neutrino Problem.

1.4 Atmospheric Neutrino Problem

Neutrinos were not only missing from solar observations; at the same time there was a conspicuous absence of neutrinos produced by cosmic rays. Cosmic rays are particles which crash into our atmosphere, and in the process produce many particles, some of which are neutrinos. Because these neutrinos are produced in the atmosphere, they are called atmospheric neutrinos. For example, charged pions, which are produced in large quantity by cosmic rays, primarily decay by

$$\begin{aligned} \pi^+ &\rightarrow \nu_\mu + \mu^+ \\ &\qquad\quad \Lsh \bar{\nu}_\mu + \nu_e + e^+, \quad \text{and} \qquad (1.5a) \\ \pi^- &\rightarrow \bar{\nu}_\mu + \mu^- \\ &\qquad\quad \Lsh \nu_\mu + \bar{\nu}_e + e^-. \qquad (1.5b) \end{aligned}$$

It was thus expected that there would be a consistent 2:1 ratio of muon (anti-)neutrinos to electron (anti-)neutrinos. As it turned out, much like in the Solar Neutrino Problem, observations showed that some neutrinos were going missing.

Early detections of the atmospheric neutrino flux were made by the Irvine-Michigan-Brookhaven detector (IMB) and Kamioka Nucleon Decay Experiment (KamiokaNDE) [7, 8]. These experiments were both designed to observe proton decays, and consisted of large tanks of water surrounded by photomultiplier tubes. The idea was that if a proton in the water were to decay, it would produce fast moving charged particles which would then emit Cherenkov radiation. This radiation would be picked up by the photomultiiplier tubes and be seen as a proton decay. However, this design was also quite effective at detecting the charged leptons produced by high energy CC interactions. Additionally, because Cherenkov radiation is emitted in the direction of motion, information about the neutrino's trajectory can also be obtained.

The atmospheric neutrino measurements by IMB, KamiokaNDE, and KamiokaNDE's successor experiment, Super-Kamiokande, saw that while the number of electron neutrinos events matched well with the theoretical predictions, there were fewer muon neutrinos than expected [9]. Furthermore, this effect seemed to be dependent on the energy of the neutrinos, as at higher neutrino energies the ratio of 2:1 muon to electron neutrinos was observed, but broke down at lower energies.

A directional dependence in flux of neutrinos was observed, with the ratio of election to muon neutrinos being greater when looking at those traveling upwards through the Earth when compared to those going downwards directly from the atmosphere. Since cosmic rays were known to be isotropic and be no different on one side of the Earth compared to the other, this disappearance in atmospheric neutrinos could not be explained with physics as was understood by the Standard Model.

1.5 Evidence of Neutrino Oscillations

The mysterious absence of neutrinos from multiple sources had become evidence for physics beyond the Standard Model, as there was no SM mechanism whereby neutrinos could simply disappear. In response to this mystery, physicist set for novel theories with which to explicate the anomaly. One hypothesis was that of *neutrino oscillations*. This theory posited that, in contrast to the Standard Model, neutrinos in fact had non-zero masses and moreover that the difference in flavors of neutrinos were actually superpositions of different mass states. The mechanism will be explained in detail in Chapter 2, but suffice it to say that because of this super-position, neutrinos could be produced in one flavor state, but later be detected in another, different flavor state. The hypothesis stated that a neutrino produced in one flavor would have some probability of being detected in another, with this probability being dependent on the energy of the neutrino and the distance it had traveled.

The Homestake experiment was looking for electron neutrinos, and their absence could be explained if, as neutrino oscillations posited, the electron neutrinos produced by the Sun "oscillated" into other flavors to which the experiment was not sensitive. Similarly, the atmospheric neutrino asymmetry could be explained as there had already been a demonstrated energy dependence in the discrepancy and the up-down asymmetry could be understood as the upwards traveling neutrinos having traversed a greater distance to reach the detector. All these results made for compelling evidence of neutrino oscillations, but it remained to show that the missing, "oscillated" neutrinos were still there.

The conclusive evidence that the missing neutrinos were not in fact missing came from the Sudbury Neutrino Observatory (SNO), an underground container of 1000 metric tons of heavy water surrounded by photomultiplier tubes [10]. Heavy water had been proposed [11] for the measurement of the solar neutrino flux by way of the NC interaction

$$\nu_x + {}^2\text{He} \rightarrow \nu_x + p + n \tag{1.6}$$

where ν_x represents a neutrino of any flavor. As a NC interaction, the process in Equation (1.6) can be seen for any flavor of neutrino. With this interaction, even if the solar neutrinos oscillated away from the electron flavor, they could still be detected.

The SNO experiment thus had multiple handles on the solar neutrino flux: one flavor dependent via CC interactions, and one flavor independent with NC interactions. SNO saw the rate of CC neutrino events was consistent with earlier observation which showed a deficit, but that the rate of NC events was consistent with the expected neutrino flux predicted by solar models. Thus, it demonstrated that the neutrinos were not disappearing, but simply changing. For the discovery of neutrino oscillations, researchers Takaaki Kajita and Arthur B. McDonald were jointly awarded the 2015 Nobel

Prize in Physics for their work as part of the Super-Kamiokande and SNO collaborations, respectively.

1.6 Beyond Standard Oscillations

Despite these observations winning a Nobel Prize, the book was not yet closed on neutrino oscillations. There were further results from experiments such as the Liquid Scintillator Neutrino Detector (LSND) which could not be explained with neutrino oscillations as were understood to explain the solar and atmospheric neutrino anomalies [12]. Both the SNO and Super-Kamiokande experiments found evidence for neutrino oscillations which could be explained with three mass states, but the anomaly observed by LSND could not be explained without an additional mass state.

As will be explained in Chapter 2, neutrino oscillations depend on the difference in neutrino masses. The observations of the SNO and Super-Kamiokande experiments could be explained by two separate mass differences, and hence three neutrino masses. This matched well with the known three flavors of neutrinos, as any additional neutrino masses would require a fourth flavor. Measurements of Z^0 boson decays at the Large Electron-Positron (LEP) collider put strict requirements on what a potential fourth flavor of neutrino could look like: it needed to be either heavier than half the mass of the Z^0 boson, or it needed not interact via the Weak Force [13]. As ordinarily neutrinos interact only via the Weak Force, a neutrino which did not would be inert to all of the forces described by the Standard Model. Such neutrinos are called *sterile*, and since the LSND experiment much effort has been spent try to prove or disprove their existence.

1.7 Personal Contributions to the Analysis

In a large collaboration it is rare that any individual contribute to every aspect of an analysis. Therefore it is worthwhile to highlight the aspects of the following analysis where my contributions were most significant. In Chapter 4 I was personally responsible for the comparison of the tricell and trajectory calibration methods mentioned in §§ 4.3-4.5. I contributed to the NC selection described in Chapter 5, in particular by developing ways of quantifying event containment and using those criteria to design the event containment requirements. I designed the NC energy estimator, with Chapter 6 being an edited version of a previous technical note I wrote describing its development [14]. Finally I played a major roll in the development of the covariance matrix fitting technique used in this analysis which is described in detail in Chapter 7.

Chapter 2

Neutrino Oscillations

One of the simplest extensions of the Standard Model is the addition of neutrino masses, but despite its simplicity it is an extension with profound implications. If there are neutrinos of different masses then an interesting effects occurs whereby a neutrino may be produced as one flavor, but later observed as another. This phenomenon is known as neutrino oscillation because the probability for observing a particular neutrino flavor state "oscillates" as a function of the neutrino's energy and distance traveled.

These oscillations may also violate Charge-Parity (CP) symmetry, wherein fundamental particles behave differently than their anti-matter counterparts would in a mirrored universe. By measuring the oscillation probabilities for neutrinos and anti-neutrinos separately we can determine the extent to which neutrino oscillations violate CP. It is also possible that neutrino oscillations could provide evidence of Charge-Parity-Time (CPT) symmetry violation, where CPT-symmetry says that physics behaves the same under a CP transformation coupled with time reversal [15]. However, CPT-violation is beyond the scope of this thesis.

For the inherent CP-violation in neutrino oscillations to be measured we must also account for the interactions between neutrinos and the matter through which they propagate. Neutrinos and anti-neutrinos scatter differently off of the electrons in matter leading to a non-CP symmetric effect on (anti-)neutrino oscillation measurements. Understanding this effect is key to detecting CP-violation in neutrinos.

Furthermore, the oscillation of neutrinos can provide us a way of searching for non-weakly interacting flavors of neutrinos. Since such neutrinos would only interact via the relatively weak force of gravity we cannot search for them via direct detection. However, the nature of neutrino oscillations means that it is possible for a neutrino to oscillate into one such undetectable flavor and lower the overall probability of neutrino detection. It is through this absence that we may find evidence of sterile neutrinos.

2.1 Oscillations in Vacuum

2.1.1 Neutrino Mixing

It is the fact that neutrinos have mass which allows for neutrino oscillations. To see this we can consider the propagation of a single neutrino with mass m and energy E. If the neutrino is initially in a state $|\nu\rangle$, then the final state after some time t is given by.

$$|\nu\rangle_{\text{final}} = e^{-iHt/\hbar}\,|\nu\rangle\,, \tag{2.1}$$

where H is the Hamiltonian operator. In the rest frame of the neutrino, the Hamiltonian is simply mc^2, and so the final state, $|\nu\rangle_{\text{final}}$, is

$$|\nu\rangle_{\text{final}} = P(\tau)\,|\nu\rangle = e^{-imc^2\tau/\hbar}\,|\nu\rangle\,, \tag{2.2}$$

where $P(\tau)$ is the propagation operator, or propagator and τ is the time which has passed in the neutrino's rest frame.

We can express the proper time in terms of the laboratory time t it took the neutrino to propagate a distance L by

$$\tau = \gamma\left(t - \frac{\upsilon L}{c^2}\right), \tag{2.3}$$

where $\upsilon = L/t$ and γ is the Lorentz factor

$$\gamma = \frac{1}{\sqrt{1 - \frac{\upsilon^2}{c^2}}}. \tag{2.4}$$

From equations (2.2) and (2.3) we can express the final state in terms of laboratory observables as

$$|\nu\rangle_{\text{final}} = e^{-i(\gamma mc^2 t - \gamma m\upsilon L)/\hbar}\,|\nu\rangle\,. \tag{2.5}$$

The quantities γmc^2 and $\gamma m v$ are the energy, E, and momentum p of the neutrino respectively. Assuming the neutrino's mass is much smaller than it's energy, *i.e.*, assuming that the neutrino is highly relativistic, then the momentum is approximately

$$p = \sqrt{E^2/c^2 - m^2c^2} = E/c - \frac{m^2c^3}{2E} + \mathcal{O}(m^4). \tag{2.6}$$

Thus the final state is approximately

$$|\nu\rangle_{\text{final}} \approx e^{-iE(t-L/c)/\hbar + im^2\frac{Lc^3}{2E\hbar}} |\nu\rangle \,. \tag{2.7}$$

Suppose we have N different flavors of neutrinos and N different mass states. Consider sets $\mathcal{F}$ and $\mathcal{M}$ of N indices such that we label the flavor states ν_α with Greek indices $\alpha \in \mathcal{F}$ and the mass states ν_j with Latin indices $j \in \mathcal{M}$. The mass of ν_j will be labeled m_j. The sets $\{\nu_\alpha\}_{\alpha\in\mathcal{F}}$ and $\{\nu_j\}_{j\in\mathcal{M}}$ each form a basis for the N-dimensional vector space of all possible neutrino states. Since $\{\nu_j\}_{j\in\mathcal{M}}$ spans the space of all neutrinos we can express each neutrino flavor ν_α as a linear combination

$$|\nu_\alpha\rangle = \sum_{j\in\mathcal{M}} U_{\alpha,j} |\nu_j\rangle \,, \tag{2.8}$$

where the coefficients $U_{\alpha,j}$ form a matrix called the neutrino mixing matrix.

Similarly we can express each mass state as

$$|\nu_j\rangle = \sum_{\alpha \in \mathcal{F}} U^*_{\alpha,j} |\nu_\alpha\rangle \,. \tag{2.9}$$

Assuming the flavor and mass states are orthonormal we have

$$\delta_{\alpha,\beta} = \langle \nu_\alpha | \nu_\beta \rangle = \sum_{j \in \mathcal{M}} \sum_{k \in \mathcal{M}} U^*_{\alpha,j} U_{\beta,k} \langle \nu_j | \nu_k \rangle = \sum_{j \in \mathcal{M}} U^*_{\alpha,j} U_{\beta,j}, \tag{2.10}$$

ie, U is a unitary matrix. Since there has been no evidence that neutrino flavor states are not orthogonal [16] we will assume that this assumption holds. Similarly we assume that the mass states are also orthonormal.

Using equation (2.7), we can see that the effect of the propagator on a neutrino in flavor state $|\nu_\alpha\rangle$ with energy E is

$$e^{-iH\tau/\hbar} |\nu_\alpha\rangle = e^{-iE(t-L/c)/\hbar} \sum_{j \in \mathcal{M}} U_{\alpha,j} e^{i m_j^2 \frac{Lc^3}{2E\hbar}} |\nu_j\rangle \tag{2.11}$$

from which it follows that the probability of measuring a ν_β of energy E

from a ν_α source a distance L away is

$$\begin{aligned}
P(\nu_\alpha \to \nu_\beta) &= \left|\langle\nu_\beta|\, e^{-iH\tau/\hbar}\, |\nu_\alpha\rangle\right|^2 \\
&= \left|\sum_{j\in\mathcal{M}}\sum_{k\in\mathcal{M}} U^*_{\beta,j} U_{\alpha,k} e^{im_k^2\frac{Lc^3}{2E\hbar}} \langle\nu_j|\nu_k\rangle\right|^2 \\
&= \left(\sum_{j\in\mathcal{M}} U^*_{\beta,j} U_{\alpha,j} e^{im_j^2\frac{Lc^3}{2E\hbar}}\right)\left(\sum_{k\in\mathcal{M}} U_{\beta,k} U^*_{\alpha,k} e^{-im_k^2\frac{Lc^3}{2E\hbar}}\right) \\
&= \sum_{j\in\mathcal{M}}\sum_{k\in\mathcal{M}} U^*_{\beta,j} U_{\alpha,j} U_{\beta,k} U^*_{\alpha,k} e^{i\Delta m^2_{jk}\frac{Lc^3}{2E\hbar}} \\
&= \frac{1}{2}\sum_{j\in\mathcal{M}}\sum_{k\in\mathcal{M}} \Big(U^*_{\beta,j} U_{\alpha,j} U_{\beta,k} U^*_{\alpha,k} e^{i\Delta m^2_{jk}\frac{Lc^3}{2E\hbar}} \\
&\qquad\qquad + U^*_{\beta,k} U_{\alpha,k} U_{\beta,j} U^*_{\alpha,j} e^{-i\Delta m^2_{jk}\frac{Lc^3}{2E\hbar}}\Big) \\
&= \sum_{j\in\mathcal{M}}\sum_{k\in\mathcal{M}} \mathcal{R}\big(U^*_{\beta,j} U_{\alpha,j} U_{\beta,k} U^*_{\alpha,k}\big)\cos\left(\Delta m^2_{jk}\frac{Lc^3}{2E\hbar}\right) \\
&- \sum_{j\in\mathcal{M}}\sum_{k\in\mathcal{M}} \mathcal{I}\big(U^*_{\beta,j} U_{\alpha,j} U_{\beta,k} U^*_{\alpha,k}\big)\sin\left(\Delta m^2_{jk}\frac{Lc^3}{2E\hbar}\right) \qquad (2.12)
\end{aligned}$$

where $\mathcal{R}$ and $\mathcal{I}$ denote the real and imaginary components respectively and we have defined the mass-squared splittings $\Delta m^2_{jk} = m_j^2 - m_k^2$. In the fifth line of equation (2.12) we have symmetrized $\Delta m^2_{jk} = -\Delta m^2_{kj}$. We then make use of the fact that $U^*_{\beta,k} U_{\alpha,k} U_{\beta,j} U^*_{\alpha,j} = \big(U^*_{\beta,j} U_{\alpha,j} U_{\beta,k} U^*_{\alpha,k}\big)^*$ to cancel the imaginary parts of both terms. Note that if all of the masses m_j are equal, including the case where they are all zero

$$P(\nu_\alpha \to \nu_\beta) = \sum_{j\in\mathcal{M}}\sum_{k\in\mathcal{M}} U^*_{\beta,j} U_{\alpha,j} U_{\beta,k} U^*_{\alpha,k} = \delta_{\alpha,\beta} \qquad (2.13)$$

because of the unitary of U, and so neutrino oscillations only occur when there are non-zero, non-degenerate neutrino masses.

Assuming the laws of physics obey CPT-symmetry, the probability for neutrino oscillations from flavor α to flavor β, $P(\nu_\alpha \to \nu_\beta)$, must be identical to the probability for anti-neutrino oscillations from flavor β to flavor α, $P(\bar{\nu}_\beta \to \bar{\nu}_\alpha)$, and so

$$\begin{aligned}
P(\bar{\nu}_\alpha \to \bar{\nu}_\beta) &= \sum_{j\in\mathcal{M}}\sum_{k\in\mathcal{M}} \mathcal{R}(U^*_{a,j}U_{b,j}U_{a,k}U^*_{b,k}) \cos\left(\Delta m^2_{jk}\frac{Lc^3}{2E\hbar}\right) \\
&- \sum_{j\in\mathcal{M}}\sum_{k\in\mathcal{M}} \mathcal{I}(U^*_{a,j}U_{b,j}U_{a,k}U^*_{b,k}) \sin\left(\Delta m^2_{jk}\frac{Lc^3}{2E\hbar}\right) \\
&= \sum_{j\in\mathcal{M}}\sum_{k\in\mathcal{M}} \mathcal{R}((U^*_{b,j}U_{a,j}U_{b,k}U^*_{a,k})^*) \cos\left(\Delta m^2_{jk}\frac{Lc^3}{2E\hbar}\right) \\
&- \sum_{j\in\mathcal{M}}\sum_{k\in\mathcal{M}} \mathcal{I}((U^*_{b,j}U_{a,j}U_{b,k}U^*_{a,k})^*) \sin\left(\Delta m^2_{jk}\frac{Lc^3}{2E\hbar}\right) \\
&= \sum_{j\in\mathcal{M}}\sum_{k\in\mathcal{M}} \mathcal{R}(U^*_{b,j}U_{a,j}U_{b,k}U^*_{a,k}) \cos\left(\Delta m^2_{jk}\frac{Lc^3}{2E\hbar}\right) \\
&+ \sum_{j\in\mathcal{M}}\sum_{k\in\mathcal{M}} \mathcal{I}(U^*_{b,j}U_{a,j}U_{b,k}U^*_{a,k}) \sin\left(\Delta m^2_{jk}\frac{Lc^3}{2E\hbar}\right) \qquad (2.14)
\end{aligned}$$

The oscillation probabilities for anti-neutrinos are thus the same as those for neutrinos but with the substitution $\sin\left(\Delta m^2_{jk}\frac{Lc^3}{2E\hbar}\right) \to -\sin\left(\Delta m^2_{jk}\frac{Lc^3}{2E\hbar}\right)$.

Since the probability in Equation (2.12) is the sum of trigonometric functions of L/E, we say that the probability *oscillates* and refer to the phenomenon of measuring non-α-flavored neutrinos from an α-flavored source as neutrino oscillation.

Since a(n) (anti-)neutrino which is produced in a flavor α must oscillate into some flavor $\beta \in \mathcal{F}$ we have

$$\sum_{\beta \in \mathcal{F}} P(\nu_\alpha \to \nu_\beta) = 1, \tag{2.15}$$

$$\text{and} \quad \sum_{\beta \in \mathcal{F}} P(\bar{\nu}_\alpha \to \bar{\nu}_\beta) = 1, \tag{2.16}$$

for all $\alpha \in \mathcal{F}$. Additionally, since $P(\nu_\alpha \to \nu_\beta) = P(\bar{\nu}_\beta \to \bar{\nu}_\alpha)$ equations (2.15) and (2.16) imply

$$\sum_{\beta \in \mathcal{F}} P(\nu_\beta \to \nu_\alpha) = 1, \tag{2.17}$$

$$\text{and} \quad \sum_{\beta \in \mathcal{F}} P(\bar{\nu}_\beta \to \bar{\nu}_\alpha) = 1, \tag{2.18}$$

for all $\alpha \in \mathcal{F}$. These equations mean that to fully describe all oscillation probabilities for N flavors of neutrino we need only write down $\frac{1}{2}N(N-1)$ equations.

2.1.2 Two Flavor Mixing

We can gain intuition for how these oscillation probabilities function by limiting ourselves to case of only two neutrino flavor and mass states. Let $\mathcal{F} = \{\alpha, \beta\}$ and $\mathcal{M} = \{1, 2\}$. Assuming the flavor states and the mass states both form orthonormal bases for the vector space of neutrino states we can switch between the bases by rotating through an angle θ

$$|\nu_\alpha\rangle = \sin(\theta)\,|\nu_1\rangle + \cos(\theta)\,|\nu_2\rangle\,, \tag{2.19a}$$

$$|\nu_\beta\rangle = \cos(\theta)\,|\nu_1\rangle - \sin(\theta)\,|\nu_2\rangle\,. \tag{2.19b}$$

If the masses of the states ν_1 and ν_2 are m_1 and m_2 respectively, the angle θ determines the probability that a ν_α would be observed to have mass m_1. We can also express the mass states in terms of the flavor states as

$$|\nu_1\rangle = \sin(\theta)\,|\nu_\alpha\rangle + \cos(\theta)\,|\nu_\beta\rangle\,, \tag{2.20a}$$

$$|\nu_2\rangle = \cos(\theta)\,|\nu_\alpha\rangle - \sin(\theta)\,|\nu_\beta\rangle\,. \tag{2.20b}$$

After judicious use of double angle formulae, the combination of equations (2.19a), (2.19b), and (2.12) gives us

$$P(\nu_\beta \to \nu_\beta) = 1 - \sin^2(2\theta)\sin^2\left(\Delta m^2_{21}\frac{Lc^3}{4E\hbar}\right). \tag{2.21}$$

From equation (2.21) it follows that

$$P(\nu_\beta \to \nu_\alpha) = 1 - P(\nu_\beta \to \nu_\beta) = \sin^2(2\theta)\sin^2\left(\Delta m^2_{21}\frac{Lc^3}{4E\hbar}\right), \tag{2.22}$$

and so there is a non-zero probability to measure a ν_α neutrino from a ν_β source if and only if the masses m_1 and m_2 are not equal, and in particular not both zero. Furthermore, we can see that the angle θ sets the maximum

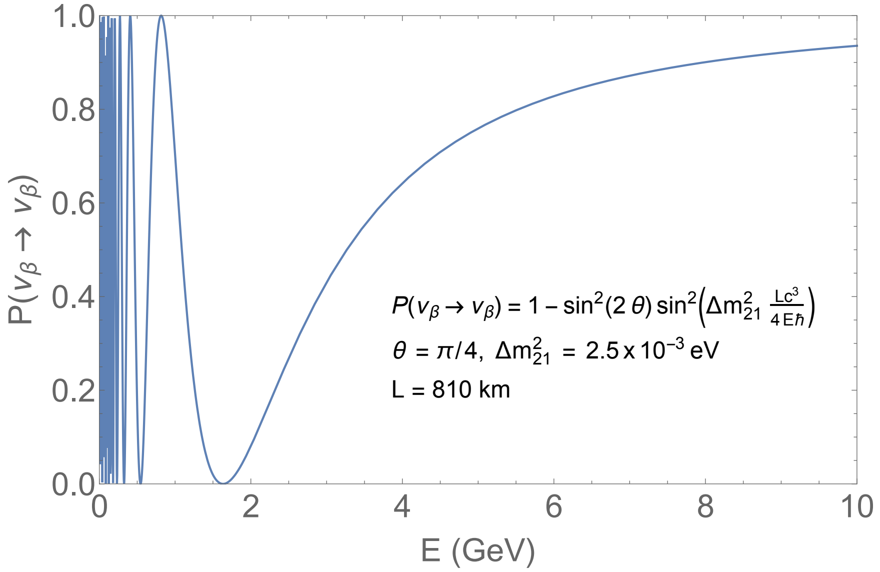

Figure 2.1: The probability of measuring a ν_β of energy E a distance $L = 810\,\text{km}$ away from a ν_β source. This figure assumes two flavor mixing with a mixing angle of $\theta = \pi/4$ and a mass-squared splitting of $\Delta m^2_{21} = 2.5 \times 10^{-3}\,\text{eV}^2$. The probability oscillates rapidly as the neutrino's energy approaches zero.

value that $P(\nu_\mu \to \nu_e)$ can obtain, while the mass-squared splitting Δm^2_{21} sets which value of L/E will obtain that maximum. To illustrate this point we can plot the oscillation probability for a sample case in Figure 2.1.

2.1.3 Three Flavor Mixing

As there are three known flavors of neutrino, ν_e, ν_μ and ν_τ we often work under the assumption that these flavors are the *only* flavors, and consider with them three mass states $\mathcal{M} = \{1, 2, 3\}$. Depending on convention, either $\Delta m^2_{21} > 0$ and $0x < \theta_{12} < \pi/2$ are assumed (as in [17, 18]) or $0x < \theta_{12} < \pi/4$ with no constraint on Δm^2_{21} (as in [19]). The measurements of solar neutrinos described in §1.3 place constraints on $\Delta m^2_{21} \cos{(2\theta_{12})}$ to be positive, which means under either convention $\Delta m^2_{21} > 0$. Measurements of atmospheric neutrino mixing show that $\Delta m^2_{21} < |\Delta m^2_{31}|$. We refer to the case where $\Delta m^2_{31} > 0$ as the *Normal Hierarchy (Ordering)* and the case where $\Delta m^2_{31} < 0$ as the *Inverted Hierarchy (Ordering)*.

The unitary matrix, U, which describes how to move between the mass and flavor bases, is called the Pontecorvo-Maki-Nakagawa-Sakata (PMNS) matrix [20]. The PMNS matrix is often parameterized with three mixing real-valued angles θ_{12}, θ_{23}, and θ_{13} and three real-valued phases δ, α_1,and α_2. The PMNS can matrix be expressed as the product of three matrices

$$U = \mathbb{A} \cdot \mathbb{C} \cdot \mathbb{S} \cdot \mathbb{M} \tag{2.23}$$

where

$$\mathbb{A} = \begin{pmatrix} 1 & 0 & 0 \\ 0 & \cos\theta_{23} & \sin_{23} \\ 0 & -\sin\theta_{23} & \cos\theta_{23} \end{pmatrix}, \tag{2.24}$$

$$\mathbb{C} = \begin{pmatrix} \cos\theta_{13} & 0 & e^{-i\delta}\sin\theta_{13} \\ 0 & 1 & 0 \\ -e^{i\delta}\sin\theta_{13} & 0 & \cos\theta_{13} \end{pmatrix}, \tag{2.25}$$

$$\mathbb{S} = \begin{pmatrix} \cos\theta_{12} & \sin_{12} & 0 \\ -\sin\theta_{12} & \cos\theta_{12} & 0 \\ 0 & 0 & 1 \end{pmatrix}, \tag{2.26}$$

$$\text{and} \quad \mathbb{M} = \begin{pmatrix} e^{i\alpha_1/2} & 0 & 0 \\ 0 & e^{i\alpha_2/2} & 0 \\ 0 & 0 & 1 \end{pmatrix}. \tag{2.27}$$

The matrix $\mathbb{A}$ contains the terms governing the atmospheric neutrino mixing described in §1.4; the matrix $\mathbb{S}$ contains the terms governing the solar neutrino mixing described in §1.3; $\mathbb{C}$ contains the cross terms; and $\mathbb{M}$ contains the phases α_1 and α_2, which are called Majorana phases as they are physically meaningful only if neutrinos are Majorana particles. However, even if neutrinos are Majorana particles, α_1 and α_2 do not contribute to neutrino oscillations. That the Majorana phases do not contribute to neutrino mixing can be seen by noting that in equation (2.12) the mixing matrix contributes only as $U^*_{\beta,j}U_{\alpha,j}$, and that

$$\begin{aligned} U^*_{\beta,j}U_{\alpha,j} &= \sum_{p=1}^{3}\sum_{q=1}^{3} (\mathbb{ACS})^*_{\beta,p}\mathbb{M}^*_{p,j}(\mathbb{ACS})_{\alpha,q}\mathbb{M}_{q,j} \\ &= (\mathbb{ACS})^*_{\beta,j}(\mathbb{ACS})_{\alpha,j}\mathbb{M}^*_{j,j}\mathbb{M}_{j,j} \\ &= (\mathbb{ACS})^*_{\beta,j}(\mathbb{ACS})_{\alpha,j} \qquad (2.28) \end{aligned}$$

as $\mathbb{M}$ is a diagonal unitary matrix.

The phase δ is called the CP-violating phase as it is responsible for the difference between $P(\nu_\alpha \to \nu_\beta)$ and $P(\bar{\nu}_\alpha \to \bar{\nu}_\beta)$. Combining equations (2.12) and (2.14) we can see this difference in oscillation probabilities is

$$P(\bar{\nu}_\alpha \to \bar{\nu}_\beta) - P(\nu_\alpha \to \nu_\beta) = 2\sum_{j=1}^{3}\sum_{k=1}^{3} \mathfrak{I}\left(U^*_{\beta,j}U_{\alpha,j}U_{\beta,k}U^*_{\alpha,k}\right)\sin\left(\Delta m^2_{jk}\frac{Lc^3}{2E\hbar}\right). \qquad (2.29)$$

Of the matrices $\mathbb{A}$, $\mathbb{C}$, and $\mathbb{S}$, $\mathbb{C}$ is the only one whose elements are not all real numbers. The complexity of $\mathbb{C}$ comes in the form of the phases $e^{\pm i\delta}$, and so if $\delta = 0$ then all the elements of $\mathbb{C}$, and hence $\mathbb{ACS}$, are real.

Using equation (2.12) with the three flavor parameters we have

$$\begin{aligned}
P(\nu_e \to \nu_e) = 1 &- \frac{1}{2}\sin^2(2\theta_{13}) - \frac{1}{2}\sin^2(2\theta_{12})\cos^4(\theta_{13}) \\
&+ \frac{1}{2}\sin^2(2\theta_{12})\cos^4(\theta_{13})\cos\left(\Delta m^2_{21}\frac{Lc^3}{2E\hbar}\right) \\
&+ \frac{1}{2}\cos^2(\theta_{12})\sin^2(2\theta_{13})\cos\left(\Delta m^2_{31}\frac{Lc^3}{2E\hbar}\right) \\
&+ \frac{1}{2}\sin^2(\theta_{12})\sin^2(2\theta_{13})\cos\left(\Delta m^2_{32}\frac{Lc^3}{2E\hbar}\right), \qquad (2.30)
\end{aligned}$$

$$
\begin{aligned}
P(\nu_e \to \nu_\mu) = {} & \frac{1}{2}\sin^2\left(2\theta_{12}\right)\left[\cos^2\left(\theta_{13}\right)\cos^2\left(\theta_{23}\right) - \frac{1}{4}\sin^2\left(2\theta_{13}\right)\sin^2\left(\theta_{23}\right)\right] \\
& + \frac{1}{2}\sin^2\left(2\theta_{13}\right)\sin^2\left(\theta_{23}\right) \\
& - \frac{1}{2}\sin^2\left(2\theta_{12}\right)\left[\cos^2\left(\theta_{13}\right)\cos^2\left(\theta_{23}\right) - \frac{1}{4}\sin^2\left(2\theta_{13}\right)\sin^2\left(\theta_{23}\right)\right] \\
& \qquad\qquad \times \cos\left(\Delta m^2_{21}\frac{Lc^3}{2E\hbar}\right) \\
& - \frac{1}{2}\left[\cos^2\left(\theta_{12}\right)\sin^2\left(2\theta_{13}\right)\sin^2\left(\theta_{23}\right)\right. \\
& \qquad \left. + \cos\left(\delta\right)\sin\left(2\theta_{12}\right)\sin\left(\theta_{13}\right)\cos^2\left(\theta_{13}\right)\sin\left(2\theta_{23}\right)\right] \\
& \qquad \times \cos\left(\Delta m^2_{31}\frac{Lc^3}{2E\hbar}\right) \\
& - \frac{1}{2}\left[\sin^2\left(\theta_{12}\right)\sin^2\left(2\theta_{13}\right)\sin^2\left(\theta_{23}\right)\right. \\
& \qquad \left. - \cos\left(\delta\right)\sin\left(2\theta_{12}\right)\sin\left(\theta_{13}\right)\cos^2\left(\theta_{13}\right)\sin\left(2\theta_{23}\right)\right] \\
& \qquad \times \cos\left(\Delta m^2_{32}\frac{Lc^3}{2E\hbar}\right) \\
& + \frac{1}{4}\cos\left(\theta_{13}\right)\sin^2\left(2\theta_{12}\right)\sin^2\left(2\theta_{13}\right)\sin^2\left(2\theta_{23}\right) \\
& \quad \times \left[\sin\left(\delta\right)\left[\sin\left(\Delta m^2_{21}\frac{Lc^3}{2E\hbar}\right) - \sin\left(\Delta m^2_{31}\frac{Lc^3}{2E\hbar}\right)\right.\right. \\
& \qquad\qquad \left. + \sin\left(\Delta m^2_{32}\frac{Lc^3}{2E\hbar}\right)\right] \\
& \qquad\qquad \left. + 2\cos\left(\delta\right)\cos\left(2\theta_{12}\right)\sin^2\left(\Delta m^2_{21}\frac{Lc^3}{4E\hbar}\right)\right],
\end{aligned}
\tag{2.31}
$$

$$
\begin{aligned}
P(\nu_\mu \to \nu_e) = {} & \frac{1}{2}\sin^2(2\theta_{12})\left[\cos^2(\theta_{13})\cos^2(\theta_{23}) - \frac{1}{4}\sin^2(2\theta_{13})\sin^2(\theta_{23})\right] \\
& + \frac{1}{2}\sin^2(2\theta_{13})\sin^2(\theta_{23}) \\
& - \frac{1}{2}\sin^2(2\theta_{12})\left[\cos^2(\theta_{13})\cos^2(\theta_{23}) - \frac{1}{4}\sin^2(2\theta_{13})\sin^2(\theta_{23})\right] \\
& \qquad\qquad \times \cos\left(\Delta m^2_{21}\frac{Lc^3}{2E\hbar}\right) \\
& - \frac{1}{2}\left[\cos^2(\theta_{12})\sin^2(2\theta_{13})\sin^2(\theta_{23})\right. \\
& \quad \left. + \cos(\delta)\sin(2\theta_{12})\sin(\theta_{13})\cos^2(\theta_{13})\sin(2\theta_{23})\right] \\
& \quad \times \cos\left(\Delta m^2_{31}\frac{Lc^3}{2E\hbar}\right) \\
& - \frac{1}{2}\left[\sin^2(\theta_{12})\sin^2(2\theta_{13})\sin^2(\theta_{23})\right. \\
& \quad \left. - \cos(\delta)\sin(2\theta_{12})\sin(\theta_{13})\cos^2(\theta_{13})\sin(2\theta_{23})\right] \\
& \quad \times \cos\left(\Delta m^2_{32}\frac{Lc^3}{2E\hbar}\right) \\
& - \frac{1}{4}\cos(\theta_{13})\sin^2(2\theta_{12})\sin^2(2\theta_{13})\sin^2(2\theta_{23}) \\
& \quad \times \left[\sin(\delta)\left[\sin\left(\Delta m^2_{21}\frac{Lc^3}{2E\hbar}\right) - \sin\left(\Delta m^2_{31}\frac{Lc^3}{2E\hbar}\right)\right.\right. \\
& \qquad\qquad \left. + \sin\left(\Delta m^2_{32}\frac{Lc^3}{2E\hbar}\right)\right] \\
& \qquad\quad \left. -2\cos(\delta)\cos(2\theta_{12})\sin^2\left(\Delta m^2_{21}\frac{Lc^3}{4E\hbar}\right)\right], \qquad (2.32)
\end{aligned}
$$

$$
\begin{aligned}
P(\nu_\mu \to \nu_\mu) = 1 - \frac{1}{2} \big[& \sin^2(2\theta_{23}) + \sin^2(2\theta_{13}) \sin^4(\theta_{23}) \\
& + \big(\cos^2(\theta_{23}) - \sin^2(\theta_{13}) \sin^2(\theta_{23})\big)^2 \\
& - \big(\big(\cos^2(\theta_{23}) - \sin^2(\theta_{13}) \sin^2(\theta_{23})\big) \cos(2\theta_{12}) \\
& \quad - \cos(\delta) \sin(2\theta_{12}) \sin(\theta_{13}) \sin(\theta_{23})\big)^2 \\
- \frac{1}{2} \times [& \cos(\delta) \sin(2\theta_{12}) \sin(\theta_{13}) \sin(2\theta_{23}) \\
& + 2\cos^2(\theta_{12}) \sin^2(\theta_{13}) \sin^2(\theta_{23}) \\
& + 2\sin^2(\theta_{12}) \cos^2(\theta_{23})\big] \\
\times [& \cos(\delta) \sin(2\theta_{12}) \sin(\theta_{13}) \sin(2\theta_{23}) \\
& - 2\sin^2(\theta_{12}) \sin^2(\theta_{13}) \sin^2(\theta_{23}) \\
& - 2\cos^2(\theta_{12}) \cos^2(\theta_{23})\big] \cos\left(\Delta m^2_{21} \frac{Lc^3}{2E\hbar}\right) \\
+ [& \cos(\delta) \sin(2\theta_{12}) \sin(\theta_{13}) \sin(2\theta_{23}) \\
& + 2\cos^2(\theta_{12}) \sin^2(\theta_{13}) \sin^2(\theta_{23}) \\
& + 2\sin^2(\theta_{12}) \cos^2(\theta_{23})\big] \\
& \quad \times \cos^2(\theta_{13}) \sin^2(\theta_{23}) \cos\left(\Delta m^2_{31} \frac{Lc^3}{2E\hbar}\right) \\
- [& \cos(\delta) \sin(2\theta_{12}) \sin(\theta_{13}) \sin(2\theta_{23}) \\
& - 2\sin^2(\theta_{12}) \sin^2(\theta_{13}) \sin^2(\theta_{23}) \\
& - 2\cos^2(\theta_{12}) \cos^2(\theta_{23})\big] \\
& \quad \times \cos^2(\theta_{13}) \sin^2(\theta_{23}) \cos\left(\Delta m^2_{32} \frac{Lc^3}{2E\hbar}\right),
\end{aligned}
\tag{2.33}
$$

and the remaining probabilities can be obtained by applying equations (2.30), (2.31), (2.32), and (2.33) to equations (2.15) and (2.17).

2.1.4 Four Flavor Oscillations

The most minimal extension of the three flavor neutrino model is to include a fourth flavor of neutrino, ν_s, and an additional mass state ν_4. In this case the mixing matrix U is a four-by-four unitary matrix. This matrix may be parameterized by six mixing angles θ_{ij} for $1 \leqslant i < j \leqslant 4$; three CP-violating phases δ_{13}, δ_{14}, and δ_{24}; and 3 Majorana phases α_1, α_2, and α_3. The mixing matrix U can be formed from the product of six rotation matrices

$$\mathbb{R}_{12} = \begin{pmatrix} \cos(\theta_{12}) & \sin(\theta_{12}) & 0 & 0 \\ -\sin(\theta_{12}) & \cos(\theta_{12}) & 0 & 0 \\ 0 & 0 & 1 & 0 \\ 0 & 0 & 0 & 1 \end{pmatrix}, \tag{2.34a}$$

$$\mathbb{R}_{13} = \begin{pmatrix} \cos(\theta_{13}) & 0 & \sin(\theta_{13})e^{-i\delta_{13}} & 0 \\ 0 & 1 & 0 & 0 \\ -\sin(\theta_{13})e^{i\delta_{13}} & 0 & \cos(\theta_{13}) & 0 \\ 0 & 0 & 0 & 1 \end{pmatrix}, \tag{2.34b}$$

$$\mathbb{R}_{14} = \begin{pmatrix} \cos(\theta_{14}) & 0 & 0 & \sin(\theta_{14})e^{-i\delta_{14}} \\ 0 & 1 & 0 & 0 \\ 0 & 0 & 1 & 0 \\ -\sin(\theta_{14})e^{i\delta_{14}} & 0 & 0 & \cos(\theta_{14}) \end{pmatrix} \tag{2.34c}$$

$$\mathbb{R}_{23} = \begin{pmatrix} 1 & 0 & 0 & 0 \\ 0 & \cos(\theta_{23}) & \sin(\theta_{23}) & 0 \\ 0 & -\sin(\theta_{23}) & \cos(\theta_{23}) & 0 \\ 0 & 0 & 0 & 1 \end{pmatrix}, \tag{2.34d}$$

$$\mathbb{R}_{24} = \begin{pmatrix} 1 & 0 & 0 & 0 \\ 0 & \cos(\theta_{24}) & 0 & \sin(\theta_{24})e^{-i\delta_{24}} \\ 0 & 0 & 1 & 0 \\ 0 & -\sin(\theta_{24})e^{i\delta_{24}} & 0 & \cos(\theta_{24}) \end{pmatrix}, \tag{2.34e}$$

$$\mathbb{R}_{34} = \begin{pmatrix} 1 & 0 & 0 & 0 \\ 0 & 1 & 0 & 0 \\ 0 & 0 & \cos(\theta_{34}) & \sin(\theta_{34}) \\ 0 & 0 & -\sin(\theta_{34}) & \cos(\theta_{34}) \end{pmatrix}, \tag{2.34f}$$

and a Majorana phase matrix

$$\mathbb{M} = \begin{pmatrix} 1 & 0 & 0 & 0 \\ 0 & e^{i\frac{\alpha_1}{2}} & 0 & 0 \\ 0 & 0 & e^{i\left(\frac{\alpha_2}{2}+\delta_{13}\right)} & 0 \\ 0 & 0 & 0 & e^{i\left(\frac{\alpha_3}{2}+\delta_{14}\right)} \end{pmatrix} \tag{2.34g}$$

as

$$U = \mathbb{R}_{34}\mathbb{R}_{24}\mathbb{R}_{14}\mathbb{R}_{23}\mathbb{R}_{13}\mathbb{R}_{12}\mathbb{M}. \tag{2.35}$$

This parameterization follows from [21] except the Majorna phases are not rotated away. Though as before in the three flavor case the matrix $\mathbb{M}$ is irrelevant to neutrino oscillations.

In general the oscillation probabilities can we obtained from equation (2.12) using the matrix in equation (2.35). However, we may make several simplifying assumptions. We may assume that the mixing angles θ_{14}, θ_{24}, and θ_{34} are small since we know that nature hues close to the three flavor model and oscillations into the fourth flavor state are suppressed in this limit. Additionally, we can assume that the fourth mass state must be significantly heavier than the first three and so $\Delta m^2_{41} \approx \Delta m^2_{42} \approx \Delta m^2_{43}$ and $\Delta m^2_{41} \gg \Delta m^2_{32} \approx \Delta m^2_{31}$. From measurements of θ_{23} we know that $\cos(2\theta_{23})$ is small. Under the above conditions the ν_μ survival probability is approximately

$$\begin{aligned}P(\nu_\mu \to \nu_\mu) = 1 &- \sin^2(2\theta_{23})\cos(\theta_{24})\sin^2\left(\Delta m^2_{31}\frac{Lc^3}{4E\hbar}\right)\\ &- \sin^2(2\theta_{24})\sin^2\left(\Delta m^2_{41}\frac{Lc^3}{4E\hbar}\right),\end{aligned} \tag{2.36}$$

while the appearance probability for ν_s from a ν_μ source is approximately

$$\begin{aligned}P(\nu_\mu \to \nu_s) = &\cos^4(\theta_{14})\cos^2(\theta_{34})\sin^2(2\theta_{24})\sin^2\left(\Delta m^2_{41}\frac{Lc^3}{4E\hbar}\right)\\ &+ \sin^3(\theta_{34})\sin^2(2\theta_{23})\sin^2\left(\Delta m^2_{31}\frac{Lc^3}{4E\hbar}\right)\\ &- \frac{1}{2}\sin(\delta_{24})\sin(\theta_{24})\\ &\quad\times \sin(2\theta_{34})\sin(2\theta_{23})\sin\left(\Delta m^2_{31}\frac{Lc^3}{2E\hbar}\right),\end{aligned} \tag{2.37}$$

2.2 Oscillations in matter

In §2.1 we made the assumption that neutrinos were not subject to any external forces, i.e., that the neutrinos were oscillating in a vacuum. This assumption allowed us to take the Hamiltonian in the propagator as simply the neutrino's energy. In matter, this is not the case and we must account for the interactions between the neutrinos and any matter they could interact with while propagating.

Under most circumstances the matter a neutrino traverses will be composed solely of electrons, protons, and neutrons. These conditions limit the possible matter interactions to charged current (CC) interactions between the electrons and electron neutrinos as well as flavor independent neutral current (NC) interactions between the neutrinos and all three fermions. Additionally, the matter is electrically neutral, and so the number of electrons and the number of protons will be equal.

From the CC interactions, the electron neutrinos pick up a potential energy

$$V_{CC}(\nu_e, e) = \sqrt{2} G_F N_e, \tag{2.38}$$

where $G_F = 8.96188 \times 10^{-5}\,\mathrm{GeV} \cdot \mathrm{m}^3$ is the Fermi coupling constant and N_e is the electron number density of the matter. The potential energy from CC interactions for anti-electron neutrinos is

$$V_{CC}(\bar{\nu}_e, e) = -\sqrt{2} G_F N_e. \tag{2.39}$$

All other flavors of neutrino remain unchanged from vacuum.

The NC interactions produce potential energies for all active flavors of neutrino. These potentials are

$$V_{NC}(\nu_\alpha, e) = -\frac{1}{\sqrt{2}} G_F N_e \left(1 - 4\sin^2(\theta_W)\right), \tag{2.40a}$$

$$V_{NC}(\nu_\alpha, p) = \frac{1}{\sqrt{2}} G_F N_p \left(1 - 4\sin^2(\theta_W)\right), \tag{2.40b}$$

$$V_{NC}(\nu_\alpha, n) = \frac{1}{\sqrt{2}} G_F N_n, \tag{2.40c}$$

while the potentials for the anti-neutrinos are

$$V_{NC}(\bar{\nu}_\alpha, e) = \frac{1}{\sqrt{2}} G_F N_e \big(1 - 4\sin^2(\theta_W)\big), \tag{2.41a}$$

$$V_{NC}(\bar{\nu}_\alpha, p) = -\frac{1}{\sqrt{2}} G_F N_p \big(1 - 4\sin^2(\theta_W)\big), \tag{2.41b}$$

$$V_{NC}(\bar{\nu}_\alpha, n) = -\frac{1}{\sqrt{2}} G_F N_n, \tag{2.41c}$$

where N_p and N_n are respectively the proton and neutron number densities and θ_W is the Weinberg angle. For a full derivation of the above potentials see [22].

We can obtain a total potential for an active flavor of neutrino in matter by combining equations 2.38, 2.40a, 2.40b, and 2.40c. Assuming $N_e = N_p$ we get

$$V(\nu_\alpha) = \frac{G_F}{\sqrt{2}}(N_n + 2\delta_{\alpha,e} N_e) \tag{2.42}$$

while $V(\bar{\nu}_\alpha) = -V(\nu_\alpha)$. Non-active flavors of neutrinos would have no potential energy from matter interactions. Splitting the flavors of neutrino into $\mathcal{F} = \mathcal{A} \cup \mathcal{S}$, where $\mathcal{A}$ contains the $|\mathcal{A}|$ active flavors of neutrinos and $\mathcal{S}$

contains the $|\mathcal{S}|$ sterile flavors, let us define

$$\mathrm{Tr} = \frac{G_F}{\sqrt{2}}(|\mathcal{A}|N_n + 2N_e), \tag{2.43a}$$

$$V_\alpha = \begin{cases} \frac{G_F}{\sqrt{2}}\left(\frac{|\mathcal{S}|}{|\mathcal{A}+\mathcal{S}|}N_n + 2\left(1 - \frac{1}{|\mathcal{A}+\mathcal{S}|}\right)N_e\right) & \text{if} \quad \alpha = e \\ \frac{G_F}{\sqrt{2}}\left(\frac{|\mathcal{S}|}{|\mathcal{A}+\mathcal{S}|}N_n - \frac{2}{|\mathcal{A}+\mathcal{S}|}N_e\right) & \text{if} \quad \alpha \neq e \in \mathcal{A} \\ -\frac{G_F}{\sqrt{2}}\left(\frac{|\mathcal{A}|}{|\mathcal{A}+\mathcal{S}|}N_n + \frac{2}{|\mathcal{A}+\mathcal{S}|}N_e\right) & \text{if} \quad \alpha \in \mathcal{S} \end{cases} \tag{2.43b}$$

The Hamiltonian for the neutrino in matter, H_{Mat} is thus

$$H_{\mathrm{Mat}} = H_{\mathrm{Vac}} + \mathrm{Tr} + \sum_{\alpha\in\mathcal{F}} V_\alpha \left|\nu_\alpha\right\rangle\!\left\langle\nu_\alpha\right|, \tag{2.44}$$

where, H_{Vac} is the vacuum Hamiltonian. However, this operator is not diagonal in terms of the mass states, and so we cannot simply apply the propagator. Instead we must find a new set of states which diagonalize the Hamiltonian. Since any terms in the Hamiltonian which are proportional to the identity have no physical effect on the propagator, we can ignore them. This includes the Tr term from the matter potential. Additionally, since

$$\begin{aligned} \langle\nu_j|H_{\mathrm{Vac}}\tau|\nu_k\rangle &= m_j c^2\tau\delta_{j,k} \\ &= (Et - p_j L)\delta_{j,k} \\ &= (Et - EL/c)\delta_{j,k} + m_j^2\frac{Lc^3}{2E}\delta_{j,k} \end{aligned} \tag{2.45}$$

has only the last term not proportional to the identity we need only diagonalize the effective Hamiltonian given by

$$H_{\text{Eff}} = \left(\sum_{j \in \mathcal{M}} m_j^2 \frac{c^4}{2E} \left|\nu_j\right\rangle\!\left\langle\nu_j\right| \right) + \left(\sum_{\alpha \in \mathcal{F}} V_\alpha \left|\nu_\alpha\right\rangle\!\left\langle\nu_\alpha\right| \right). \tag{2.46}$$

2.2.1 Two Flavor Mixing in Matter

Considering the two flavor case outlined in §2.1.2, equation (2.43b) becomes

$$V_e = \frac{G_F}{\sqrt{2}} N_e, \tag{2.47a}$$

$$\text{and} \quad V_\mu = -\frac{G_F}{\sqrt{2}} N_e. \tag{2.47b}$$

While the vacuum Hamiltonian becomes

$$\begin{aligned} H_{\text{Vac,2flav}} &= \left(\sum_{j \in \mathcal{M}} m_j^2 \frac{c^2}{2E} \left|\nu_j\right\rangle\!\left\langle\nu_j\right| \right) \\ &= \frac{(m_1^2 + m_2^2)c^4}{4E} \left(\left|\nu_e\right\rangle\!\left\langle\nu_e\right| + \left|\nu_\mu\right\rangle\!\left\langle\nu_\mu\right| \right) \\ &\quad + \frac{\Delta m^2 c^4}{4E} \cos(2\theta) \left|\nu_e\right\rangle\!\left\langle\nu_e\right| - \frac{\Delta m^2 c^4}{4E} \sin(2\theta) \left|\nu_e\right\rangle\!\left\langle\nu_\mu\right| \\ &\quad - \frac{\Delta m^2 c^4}{4E} \sin(2\theta) \left|\nu_e\right\rangle\!\left\langle\nu_\mu\right| - \frac{\Delta m^2 c^4}{4E} \cos(2\theta) \left|\nu_\mu\right\rangle\!\left\langle\nu_\mu\right|. \end{aligned} \tag{2.48}$$

Since $\dfrac{(m_1^2+m_2^2)c^4}{4E}$ is diagonal in $H_{\text{Vac,2flav}}$, an effective two-flavor matter Hamiltonian is

$$\begin{aligned}
H_{\text{Eff,2flav}} = \quad & \frac{\Delta m^2 c^4}{4E}\left(\cos(2\theta) + \frac{2\sqrt{2}G_F N_e E}{\Delta m^2 c^4}\right)|\nu_e\rangle\langle\nu_e| \\
& - \frac{\Delta m^2 c^4}{4E}\sin(2\theta)\,|\nu_e\rangle\langle\nu_\mu| \\
& - \frac{\Delta m^2 c^4}{4E}\sin(2\theta)\,|\nu_\mu\rangle\langle\nu_e| \\
& - \frac{\Delta m^2 c^4}{4E}\left(\cos(2\theta) + \frac{2\sqrt{2}G_F N_e E}{\Delta m^2 c^4}\right)|\nu_\mu\rangle\langle\nu_\mu|\,.
\end{aligned} \tag{2.49}$$

This Hamiltonian is no longer diagonal in terms of the mass eigenstates, and must be diagonalized. To do this we define several useful quantities. The first is a dimensionless variable which contains the effect of the matter

$$x = \frac{2\sqrt{2}G_F N_e E}{\Delta m^2 c^4}, \tag{2.50}$$

a new angle θ_M given by

$$\sin^2(2\theta_M) = \frac{\sin^2(2\theta)}{\sin^2(2\theta) + (\cos(2\theta) + x)^2}, \tag{2.51}$$

and a scaled mass splitting

$$\Delta m_M^2 = \Delta m^2 \sqrt{\sin^2(2\theta) + (\cos(2\theta) + x)^2}. \tag{2.52}$$

Note that in the absence of matter, x becomes zero, $\sin^2(2\theta_M) = \sin^2(2\theta)$, and $\Delta m_M^2 = \Delta m^2$. We can then define two neutrinos states

$$|\nu_{1_M}\rangle = \sin(\theta_M)|\nu_e\rangle + \cos(\theta_M)|\nu_\mu\rangle\,, \tag{2.53a}$$

$$|\nu_{2_M}\rangle = \cos(\theta_M)|\nu_e\rangle - \sin(\theta_M)|\nu_\mu\rangle\,. \tag{2.53b}$$

Applying the Hamiltonian in equation (2.49) to the state $|\nu_{1_M}\rangle$ we find

$$\begin{aligned} H_{\text{Eff,2flav}}|\nu_{1_M}\rangle = {} & \frac{\Delta m_M^2 c^4}{4E}\cos(2\theta_M)\sin(\theta_M)|\nu_e\rangle \\ & - \frac{\Delta m_M^2 c^4}{4E}\sin(2\theta_M)\cos(\theta_M)|\nu_e\rangle \\ & - \frac{\Delta m_M^2 c^4}{4E}\sin(2\theta_M)\sin(\theta_M)|\nu_\mu\rangle \\ & - \frac{\Delta m_M^2 c^4}{4E}\cos(2\theta_M)\cos(\theta_M)|\nu_\mu\rangle \\ = {} & \frac{\Delta m_M^2 c^4}{4E}\big(\cos(2\theta_M) - 2\cos^2(\theta_M)\big)\sin(\theta_M)|\nu_e\rangle \\ & - \frac{\Delta m_M^2 c^4}{4E}\big(\cos(2\theta_M) + 2\sin^2(\theta_M)\big)\cos(\theta_M)|\nu_\mu\rangle \\ = {} & -\frac{\Delta m_M^2 c^4}{4E}|\nu_{1_M}\rangle\,, \end{aligned} \tag{2.54}$$

and similarly

$$H_{\text{Eff,2flav}}|\nu_{2_M}\rangle = \frac{\Delta m_M^2 c^4}{4E}|\nu_{2_M}\rangle\,. \tag{2.55}$$

The states $|\nu_{1_M}\rangle$ and $|\nu_{2_M}\rangle$ thus diagonalize the effective Hamiltonian in the same way as the mass eigenstates $|\nu_1\rangle$ and $|\nu_2\rangle$ diagonalize the Hamiltonian in vacuum. The form of the oscillation of two neutrino flavors in matter is identical to two flavor oscillations in vacuum but with effective mass splitting Δm_M^2 and mixing angle θ_M.

Note that if instead of two active flavors we had one active (non-electron) flavor, ν_μ, and one sterile flavor ν_s we would obtain the same results except with the electron density N_e being replaced with the neutron density N_n. For rock we can expect $N_n \sim N_e$ [16]. Thus the strength of the matter effect for sterile flavors weaker than for active flavors by the ratio of the mass splittings

$$x_{\text{sterile}} \sim x_{\text{active}} \frac{\Delta m_{\text{active}}^2}{\Delta m_{\text{sterile}}^2}. \tag{2.56}$$

By the assumptions laid out in §2.1.4 $m_{\text{sterile}}^2 \gg \Delta m_{\text{active}}^2$, and so we can safely ignore the effect of matter on sterile oscillations.

2.2.2 The MSW Effect

As x goes to zero, the oscillations in matter approach those in vacuum. However it is also worth considering the opposite case, that in which x becomes very large. In a very dense medium, equation (2.51) forces $\sin(\theta_M) \sim 1$ and $\cos(\theta_M) \sim 0$, and so $|\nu_e\rangle \sim |\nu_{2_M}\rangle$. So an electron neutrino in a very dense medium is in the more massive of the two effective mass eigenstates. The preceding case is exactly what happens for electron neutrinos created in the dense core of the Sun.

The Mikheyev–Smirnov–Wolfenstein (MSW) effect occurs when the density of the medium is no longer constant, but instead changes adiabatically along the path of the neutrino. When the density of matter changes slowly, the state of neutrino remains in the effective state it started in. Practically speaking, this means that an electron neutrino created in the Sun's core remains in the state $|\nu_{2_M}\rangle$ as it travels through the Sun even as the effective mass splitting and mixing angle changes with the changing density. As the neutrinos exit the Sun and enter the vacuum of space they must all be in the state $|\nu_2\rangle$. Thus the deficiency in electron neutrinos observed by the Homestake experiment in §1.3 was actually due to the fact that $|\langle\nu_e|\nu_2\rangle|^2 \neq 1$.

2.3 Analysis Phenomenological Framework

For this analysis we are investigating a four neutrino flavor model with three active flavors and one sterile flavor. We assume that the fourth mass state we introduce is sufficiently large than Equations (2.36) and (2.37) hold. This model is a sufficient candidate to explain the anomalous oscillations described in §1.6 and is a model to which the NOvA experiment is sensitive.

Chapter 3

The NOvA Experiment

The NuMI Off-axis ν_e Appearance (NOvA) experiment is a long-baseline neutrino oscillation experiment operated by the Fermi National Accelerator Laboratory (FNAL) consisting of a Near Detector (ND) and a Far Detector (FD) separated by a distance of $810\,\mathrm{km}$. Neutrinos are produced by the Neutrinos at the Main Injector (NuMI) beam near Batavia, Illinois and are used for several neutrino experiments. NOvA was built to lay $14.6\,\mathrm{mrad}$ off the central axis of the NuMI beam. This choice was made so that the neutrinos seen by the NOvA detectors see a flux of neutrinos which peaks at an energy of $2\,\mathrm{GeV}$ [23]. The mechanism for responsible for this spectral shape will be described in §3.1.

The NOvA detectors were designed to be functionally identical tracking calorimeters. This goal was achieved by the composition of numerous liquid scintillator cells arranged in planes of alternating orientation. These cells are read out by avalanche photodiodes (APDs) to convert the scintillation light into a digital signal.

The original intention of the NOvA experiment was to measure the parameters θ_{13}, θ_{23}, and δ_{CP} of the PMNS mixing matrix as well as measuring the value of the neutrino mass splitting Δm^2_{32} and determining the mass hierarchy. However, NOvA is not limited to these inquires and can also be used to search for sterile neutrinos

3.1 The NuMI Beam

The origin of the NuMI beam starts with the acceleration of hydrogen ions H^- by a linear accelerator to an energy of 400 MeV [24]. These ions are then passed through a carbon filter which strips them of electrons. The resultant protons enter a 474.2 m circumference synchrotron accelerator where they are accelerated to 8 GeV before feeding into the Main Injector, a 3, 319.4 m synchrotron that takes the protons up to 120 GeV.

The Main Injector directs the 120 GeV towards a 1.2 m long graphite target. Many kinds of particles are produced by the collisions of protons on the carbon atoms, but of interest to NuMI are the pions π^+ and π^- which predominately decay into muons and muon-neutrinos

$$\pi^+ \to \nu_\mu + \mu^+, \quad \text{and} \tag{3.1a}$$

$$\pi^- \to \bar{\nu}_\mu + \mu^-. \tag{3.1b}$$

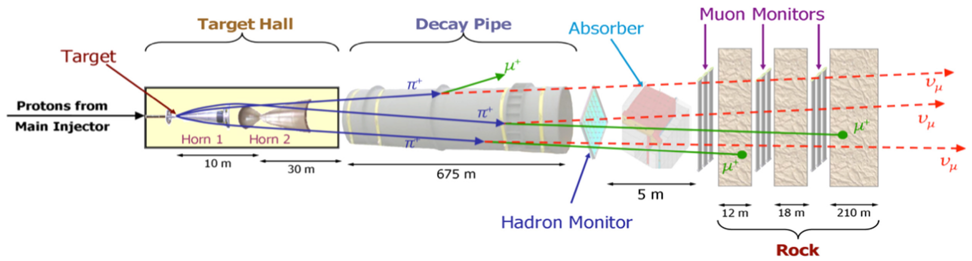

Figure 3.1: A schematic diagram of the NuMI beam which shows the target, magnetic horns, decay pipe, and absorbers [24].

There is also a secondary beam component formed from the decay of kaons K^+ and K^-, who primarily decay as

$$K^+ \to \nu_\mu + \mu^+, \quad \text{and} \tag{3.2a}$$

$$K^- \to \bar{\nu}_\mu + \mu^-. \tag{3.2b}$$

By focusing the charged pions into a beam with magnetic horns, NuMI creates a beam of either ν_μ or $\bar{\nu}_\mu$ depending on the current supplied to the magnets. By supplying a forward horn current (FHC) we select for the positively changed π^+ and create a beam of primarily ν_μ. By reversing the horn current (RHC) we focus the decay of π^- into $\bar{\nu}_\mu$. The pions primarily decay in a 675 m long evacuated decay pipe which starts 46 m from the target. After the decay pipe is an absorber made of aluminum, steel, and concrete designed to halt any hadrons in the beam. The absorber is followed by 240 m of dolomite rock to absorb the muons which remain. Figure 3.1 diagram of the NuMI beam.

In the lab reference frame, the neutrino flux Φ_ν and energy E_ν produced from a pion decay from Equation (3.2) are [25]

$$\Phi_\nu = \left(\frac{2\gamma}{1+\gamma^2\theta^2}\right)^2 \frac{A}{4\pi z} \tag{3.3}$$

and

$$E_\nu = \frac{0.43E_\pi}{1+\gamma^2\theta^2} \tag{3.4}$$

where $\gamma = E_\pi/m_\pi c^2$, θ is the angle between pion's initial trajectory and the direction the neutrino is emitted in, A is the area of the detector seeing the neutrino, and z is the distance the neutrino has traveled from the decay. A detector on axis with the pion decay thus sees a neutrino energy spectrum proportional to the pion energy spectrum. However when $\gamma^2\theta^2 \gg 1$, which necessitates $\theta \neq 0$, the neutrino energy is proportional to E_π^{-1}. Since E_π^{-1} is relatively flat at high energies in comparison to E_π, this leads to a neutrino energy spectrum peaked at a well defined energy. For $\theta \sim 14$ mrad this peak energy is approximately 2 GeV [25]. This spectral shaping is useful for a neutrino oscillation experiment since the oscillation probability is, in the two flavor approximation in Equation (2.22), proportional to $\sin\left(\Delta m^2 \frac{Lc^3}{4E\hbar}\right)$. By building the detector at a particular angle off-axis and distance from the neutrino production we can set both L and E. If the mass splitting Δm^2 is known with some precision we can then ensure our detector sees neutrinos when the oscillations are maximal simply by choosing the location of the detector. The off-axis angle and baseline of NOvA were chosen such that the oscillations driven by Δm^2_{32} are maximal with a peak neutrino energy of 2 GeV.

Simulation predicts that the NuMI beam running FHC produces a flux of neutrinos 14.6 mrad off axis composed of neutrinos with energy between 1 and 5 GeV, 96% of which are ν_μ with most of the contamination being $\bar{\nu}_\mu$, with less than 1% being ν_e and $\bar{\nu}_e$ [26]. Running in RHC mode we instead predict 83% $\bar{\nu}_\mu$ with the remainder being ν_μ, and less than 1% being ν_e and $\bar{\nu}_e$ [26]. When NOvA is taking Main Injector delivers protons for 10 μs to the NuMI target every 1.33 s [27]. As of the cut off for data to be included in this analysis, the NuMI beam delivered 11×10^{20} protons on target (POT) to the ND and 9.5×10^{20} POT to the FD while running FHC, and 11.8×10^{20} POT to the ND and 12×10^{20} POT to the FD while running RHC.

3.2 The NOvA Detectors

Both of NOvA's two detectors are located 14.6 mrad off the central axis of the NuMI beam, with the ND seeing a range of $11 \sim 20$ mrad, and are of similar construction. The ND is located 100 m underground and 1 km away from the NuMI beam target. The FD is located 810 km from the NuMUI target in Ash River, Minnesota. The FD is on the surface, but is under a 3 m water-equivalent overburden to reduce cosmic ray background events. The ND has a mass of 300 tons while the FD is 14.4 kilotons [23].

To orient ourselves while talking about the detector and events therein we define local coordinate systems (x, y, z) for each detector such that the positive z-direction is the direction from the NuMI target to the FD, the y-direction points upwards, and the x-direction is such that (x, y, z) is right-handed. The origin of the coordinate systems are situated in the center of the first plane of their respective detector.

Both detectors are made up of many PVC cuboids full of liquid scintillator called cells. Each cell is roughly 3.56 cm wide and 5.59 cm deep with cell walls 0.51 cm thick. The length of each cell in the ND is 3.9 m while FD cells are 15.5 m. A diagram of a single NOvA cell can be seen in Figure 3.2.

The cells are arranged into planes consisting of cells adjoined lengthwise. The planes are made of 96 cells for ND planes and 384 cells for FD planes, with every other of the final 22 planes of the ND containing only 64 cells. The planes were then attached depthwise with planes in alternating orientations. Planes with their cells' length oriented in the vertically direction are called x-view planes and planes with their cells' length oriented horizontally are called y-view planes. These planes are so called because the x-view planes will read out the position of a particle in the horizontal (x) direction, and likewise for the y-view planes. Since the cells have alternating orientations in different planes we define a view-agnostic coordinate w which give the locations within a cell. We define w such that it is equivalent to x in y-view cells and y in x-view cells.

By alternating the views of the plans in each detector NOvA is able to track a changed particle as it moves through the detector. The ND is composed of 214 planes while the FD has 896. These planes make the total

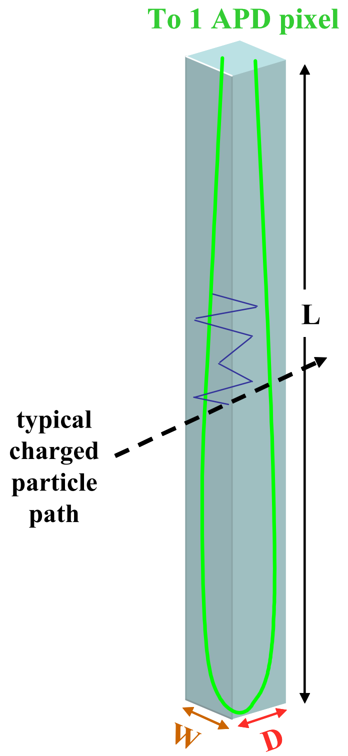

Figure 3.2: A schematic diagram of a single NOvA cell. Shown in green is the wavelength shifting fiber contained in the scintillation mixture. The width W and depth D are 3.56 cm and 5.59 cm respectively, while the length L depends on which detector the cell is in. For the ND L $=$ 3.9 m and L $=$ 15.5 m for the FD. Also shown is the scintilation light (blue) generated by a charged particle (black dashed) traveling through the cell [28].

lengths of the ND and FD 12.8 m and 60 m respectively. The final 22 planes in the ND farthest down stream of the beam (in the positive z-direction) are two thirds the height of ordinary ND cells and form what is call the Muon Catcher. The muon catcher has 10 cm of steel interspersed between each plane which functions to slow down any muons produced from neutrino interactions.

Inside each cell is liquid scintillator composed of mineral oil, pseudocumene (1,2,4-trimethylbenzene), PPO (2,5-diphenyloxazole), bis-MSB (1,4-bis-(o-methyl-styryl)-benzene), Stadis-425, and vitamin E [29]. The mineral oil makes up the bulk of the scintillator, around 94%, and functions to as a solvent to hold the other materials. The pseudocumene acts as the primary scintillating substance and emits $270 \sim 320\,\mathrm{nm}$ photons when excited by passing charged particles. These photons are then absorbed by the PPO, which then radiates predominantly $340 \sim 380\,\mathrm{nm}$ though it can emit photons with wavelengths as large as $460\,\mathrm{nm}$. The bis-MSB then further converts these photons to a wavelength mostly in the range of 390 to $440\,\mathrm{nm}$, though some may go as large as $480\,\mathrm{nm}$ [29]. The Stadis-425 acts as a antistatic and serves to reduce the risk of fire by increasing the conductivity of the mixture allowing it to discharge more efficiently. The vitamin E was added to prevent discoloration which could interfere with the photons traveling through the scintillator [29].

Suspended in the scintillator is a wavelength shifting (WLS) fiber which captures and converts photons with wavelengths between 400 and $450\,\mathrm{nm}$ into photons with wavelengths in the range 490 to $550\,\mathrm{nm}$. The WLS fibers carry the photons to APDs attached to each plane on the positive w-side. The APDs convert the photons from the WLS fibers into electrons which can be read out as a digital signal. These photoelectrons (PE) form the basic physical measurement of activity in detector. It is the PE signal which is calibrated in order to associate the activity with the energy deposited in the scintillation by passing particles. This calibration process is described in Chapter 4.

Chapter 4

Energy Calibration

All detectors must be calibrated. The NOvA detectors are composed of individual scintillating cells, each with their own electronics and filled with one of several scintillation liquid batches. These cell-by-cell differences means that we must calibrate each segment of the detector separately. To handle the differing responses we the compare the signals produced in each cell to known energy depositions.

To this end we use cosmic ray muons as a standard candle. As muons traverse the scintillator they emit radiation in accordance with their energy and the density of the scintillator. As the radiative losses for the muon are well known, we can determine the rate of energy depotition per unit length from the geometry of the muon's trajectory. We estimate the distance the cosmic muon travels in a cell to associate the cell's response to the known energy deposition.

Since the physics of muon energy loss in matter is well understood, the main source of uncertainty in our calibration is determining the distance the cosmic muon traversed a given cell. However, we are also limited by the number of cosmic ray muons that can be used for calibration. As each cell needs to be calibrated separately we want to maximize the number of cosmic muons used in our calibration. This balancing act is at the core of NOvA's calibration strategy. What follows is a discussion of how NOvA uses cosmic ray muons to calibrate the detectors and how we compared different reconstruction techniques to maximize our calorimetric energy estimation.

4.1 Standard Candle

The average energy lost per unit length by a charged particle as it travels through a material, $\left\langle -\frac{dE}{dx} \right\rangle$, is well described by the Bethe-Bloch equation [16]

$$\left\langle -\frac{dE}{dx} \right\rangle = K\frac{Z}{A}\frac{1}{\beta^2}\left[\frac{1}{2}\ln\left(\frac{2m_e c^2\beta^2\gamma^2 Q_{\max}}{I^2}\right) - \beta^2 - \frac{\delta}{2} + \frac{Q_{\max}^2}{8(\gamma M c^2)^2}\right]. \quad (4.1)$$

The numerous quantities in equation (4.1) can be broken down in to two primary categories: material and kinematic. The material properties are Z, A, and I, which are the atomic number, atomic mass and mean excitation energy of the material respectively. The kinematic variables are $\beta = \nu/c$, $\gamma = (1-\beta^2)^{-1/2}$, and $Q_{\max} = \dfrac{2m_e c^2\beta^2\gamma^2}{1+2\gamma m_e/M + (m_e/M)^2}$, where m_e and M

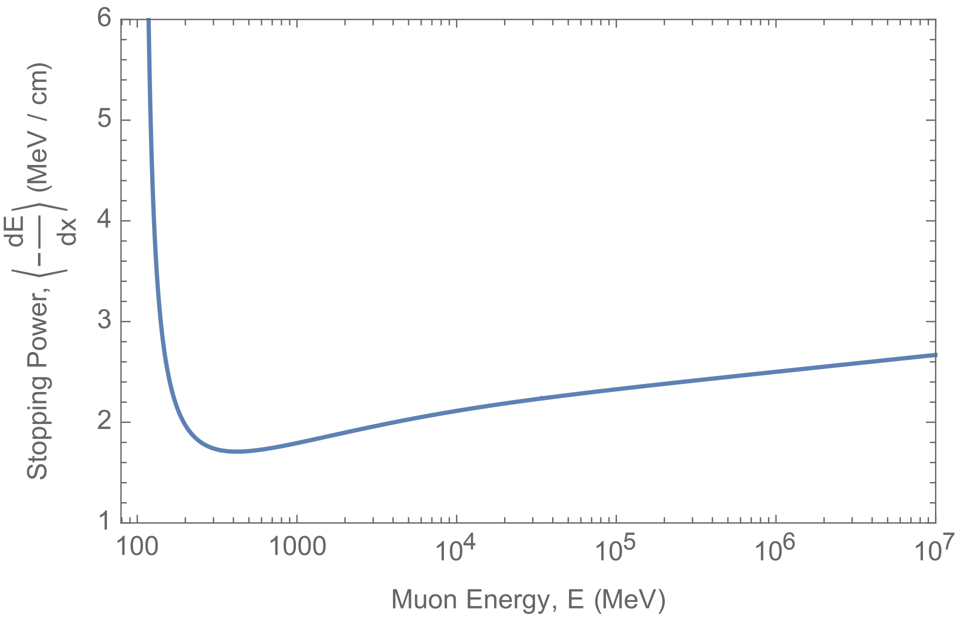

Figure 4.1: The stopping power of benzene on an impinging muon as calculated using equation (4.1). The parameters for the Bethe-Bloch equation were taken from the Particle Data Group [16].

are the mass of an electron and of the traveling particle. The remaining terms are the scaling constant, $K = 0.307075$ MeV g^{-1} cm^2, and the density effect correction, δ, which is dependent on β and the material in question. For benzene, which is a similar chemical makeup to the primary scintillant used by NOvA (1,2,4-trimethylbenzene) [29], the result of equation (4.1) can be seen in Figure 4.1. Important to note is that the stopping power is relatively flat for a large range of energies and is close to the minimum value of 1.70831 MeV cm^{-1}, which occurs exactly for $E = 418.823$ MeV. It is this consistent energy loss that allows NOvA to use muons for its calibration.

A particle which loses energy at the minimum value of equation (4.1) is said to be a minimally ionizing particle (MIP). Since the energy lost by a MIP is readily predictable from equation (4.1), identifying detector activity caused by MIPs gives a good estimate of how much energy per unit length was deposited in the scintillator. Assuming a particle is traveling through a single medium until it loses all kinetic energy we can integrate the Bethe-Bloch equation to find the distance, L, from the end of the particle's track at which it reaches an energy, E,

$$L = \int_{Mc^2}^{E} \frac{dE'}{\left\langle -\frac{dE'}{dx} \right\rangle}. \tag{4.2}$$

As L is a bijective function of E, we can associate the position along the particle's track to a unique energy, and thus also the energy deposited per unit length via equation (4.1). The stopping power of a muon impinging on benzene as a function of L can be seen in Figure 4.2. From this figure we can see that the stopping power is close to the minimum value of $1.70831\ \mathrm{MeV\,cm^{-1}}$ when the muon is between $1\ \mathrm{m}$ and $2\ \mathrm{m}$ from the point at which it decays.

However, when we are considering a real muon moving through the NOvA detector we must consider more than just the scintillator. The non-scintillating materials in the detector also cause muons to lose energy. Accounting for the energy lost in non-scintillating material and the composition of the scintillator by simulating muons in the NOvA Far Detector we find that cosmic muons deposit a minimum of $1.7915 \pm 0.0035\ \mathrm{MeV\,cm^{-1}}$ in the scintillator, and deposit within 1.8% of this amount between $1\ \mathrm{m}$ and

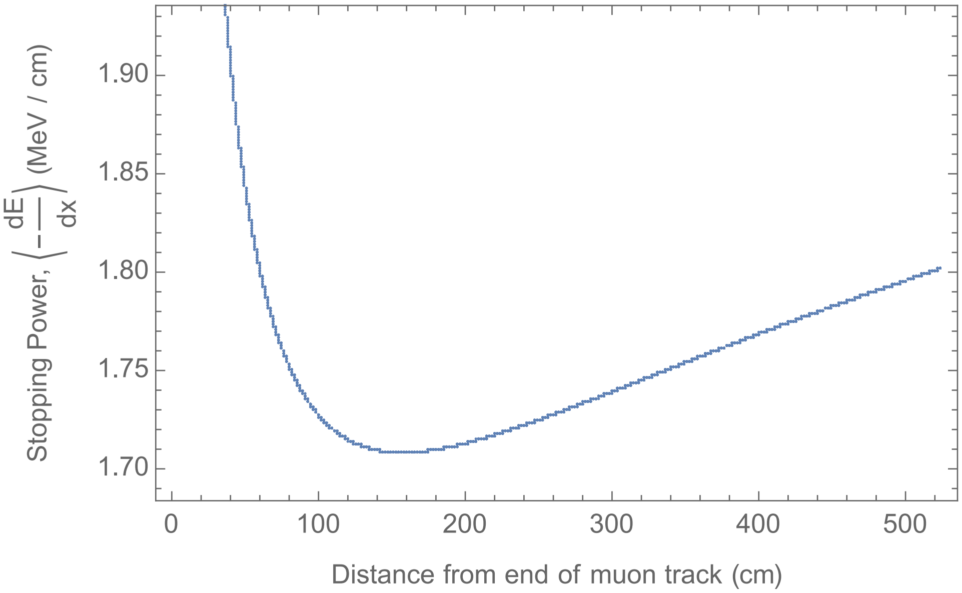

Figure 4.2: The stopping power of benzene on an impinging muon, obtained using equation (4.1), as a function of distance from the end of the muon's track, L. The distance was obtained by numerically integrating (4.1).

2 m from the end of the muon track [30].

4.2 Event Selections

We can now convert the activity observed in a cell, hereafter a cell hit, using the deposited energy per unit length and a reconstruction of the muon's trajectory. As NOvA uses tracking detectors we are able to reconstruct the path a muon takes through the detector easily. We use this information to predict the path length inside any given cell along the muon track.

To ensure we accurately reconstruct the path length inside the cell we restrict ourselves to only looking at muon tracks which

1. stop within the detector
2. have a total track length greater than 200 cm;
3. have at least 80% of the hits in the event included in the reconstructed track;
4. have a track which crosses at least three planes;
5. travel at least 70 cm down the z-axis of the detector;
6. have an initial z-direction cosine greater than 0.2;
7. have no more than six hits per x-/y-plane of the detector;
8. have no more than a 10% asymmetry in the number of x- and y-planes; and
9. have a track that starts at most 10 cm away from any edge of the detector.

The conditions 2 through 4 ensure that we reconstruct the muon path accurately; the conditions 5 through 9 require that the muon travel along the beam direction and mimic the muons produced by beam events; and condition 9 helps to remove activity that is not truly cosmogenic. In addition to the above conditions on the track as a whole we do not use individual cell hits which are further than three times the mean separation between cell hits away from the previous cell hit in the track or which have a reconstructed path greater than 10 cm within the cell. This condition removes low quality cell hits, even if the track containing them is reconstructable on the whole.

These restrictions on their own do not fully specify the reconstruction method. Two main algorithms were considered, which will be described in the following sections. These two algorithms have different restrictions on the cell hits they can reconstruct which changes how many events we can use in our calibration. We want to have as large a calibration sample as possible to account for statistical fluctuations. However, we also wish to ensure that our reconstructions are as accurate as possible. Our two algorithms are compared on the basis of these two factors.

4.3 Tricell Method

To qualify for tricell reconstruction the cell hit must have two adjacent cells in the same plane which also see activity from the muon. This requirement ensures that muons cross the two opposite sides of the cell, a distance known to be 3.56 cm on average. Using this fact in conjunction with the direction the muon is going through the plane we can estimate path length in the cell, as seen in Figure 4.3.

Since we require the muon to cross at least three planes of the detector we have a handle on the direction of the muon as we know how many x-(y-)cells the muon crossed in the interval it took to move through the width of three planes in the z-direction as well as the distance between

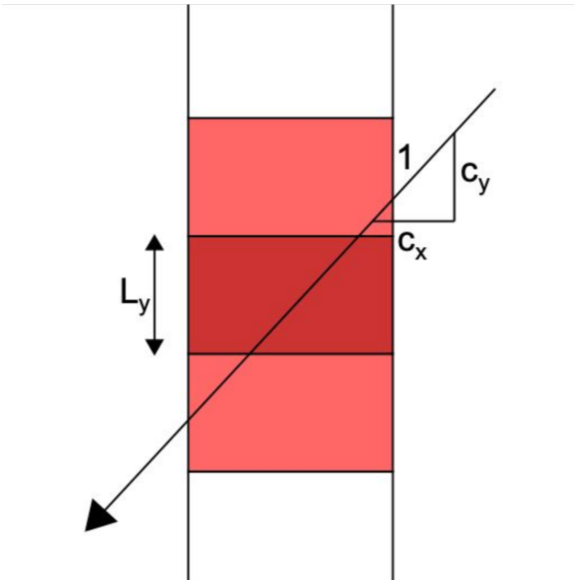

Figure 4.3: A schematic depiction of a cell hit valid for the tricell method within a y-plane. By requiring activity to occur in all three red cells, we know that the muon must have crossed the two walls of the dark red cell, which are on separated by the interior cell width L_y, which is on average 3.56 cm, and the path through the cell can be estimated as $L = L_y/c_y$. The activity in the dark red cell is then suitable for the tricell calibration. [30]

the y-(x-)cells in the outer two planes. Taking the direction cosines for the muon in the cell we can reconstruct the path length of the muon track in a x-(y-)plane cell as

$$L_{\text{path}} = L_{x(y)}/c_{x(y)} \tag{4.3}$$

where $L_{x(y)}$ is the width of the cell in the x-(y-)direction and $c_{x(y)}$ is the corresponding direction cosine. This method will almost always underestimate the path as it accounts for the motion in only two directions.

4.4 Trajectory Method

The trajectory reconstruction does not impose additional constraints on the cell hits. Instead, it relies on the reconstruction of the muon's path as a whole. Using the tracking capabilities of the detector we reconstruct the points in three dimensional space which the muon likely passed through each cell. We call these reconstructed points *trajectory point*. To estimate the path we draw a line from the trajectory point in the cell to the next trajectory point and calculate where this line intersects the cell's walls. A schematic of this reconstruction can be seen in Figure 4.4.

The reconstruction accuracy in the trajectory method is limited by our ability to reconstruct trajectory point. However, as this method does not require adjacent cell hits, there are far more of them, allowing for increased coverage of the detector.

4.5 Method Comparisons

To compare these reconstruction methods we use the Monte Carlo simulation where the true muon path through each cell is known. We apply the selections outlined in §4.3 and §4.4 and then reconstruct the path for each hit using both the tricell and trajectory methods whenever possible.

As each cell needs to be calibrated individually it is better to maximize the number of hits in each cell. As can be seen in Figure 4.5, in each cell there are between 3 and 10 times more trajectory hits than tricell hits. This

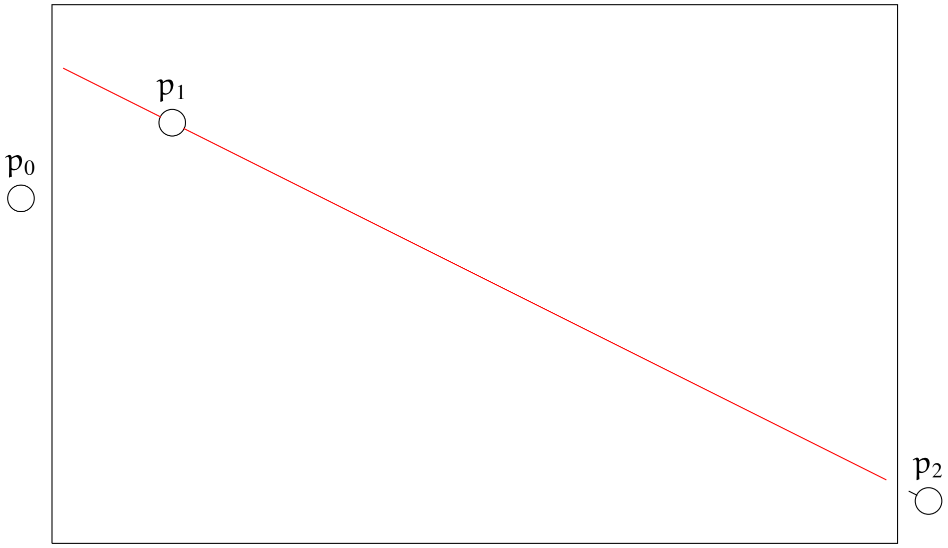

Figure 4.4: A diagram illustrating the trajectory reconstruction. Here a muon is reconstructed as having passed through the location p_1 inside a cell, and p_2 is the subsequent trajectory point. The trajectory reconstruction draws the line containing p_1 and p_2 and estimates the muon path length in the cell consisting of the segment of that line contained withing the walls of the cell. This segment is shown in red on the diagram. Note that the trajectory point p_0 which precedes p_1 does not factor into the reconstruction.

additional coverage allows for the response to be averaged over more hits and potentially have a more precise understanding of each cell's response.

However, it is also important to consider the accuracy of the path reconstructions in addition to the number of hits used. Figures 4.6 and 4.7 show the accuracy in the reconstructed paths for simulated cell hits for the tricell and trajectory methods respectively. Note that there are no tricell hits with a path less than 3.56 cm as the reconstruction is limited by the width of the cells. In both views the trajectory method has a wider distribution of uncertainties for all path lengths in both views than the tricell method does.

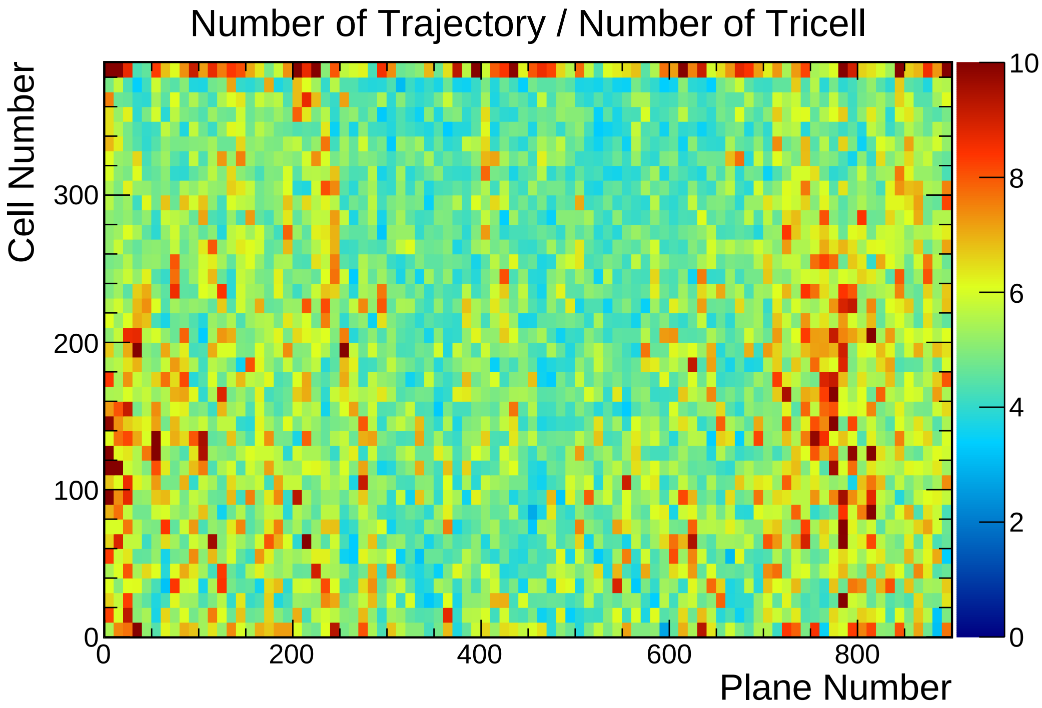

Figure 4.5: The ratio of the number of simulated cell hits in the NOvA Far Detector which can be reconstructed with the trajectory to the numberused with the tricell method. Each bin corresponds to one cell specified by the location of the cell in the plane and the plane in the detector.

Additionally, trajectory reconstructions with a path length less than 3.5 cm tend to underestimate the length more frequently.

We can compare the number of hits for each reconstructed path length between the two methods. This comparison, which can be seen in Figure 4.8, shows that much of the gain in coverage from the trajectory method occurs for hits with a reconstructed path length less than 3.5 cm. Since this range of path lengths falls in the region for which we know the trajectory method tends to underestimate the path we conclude that many of the

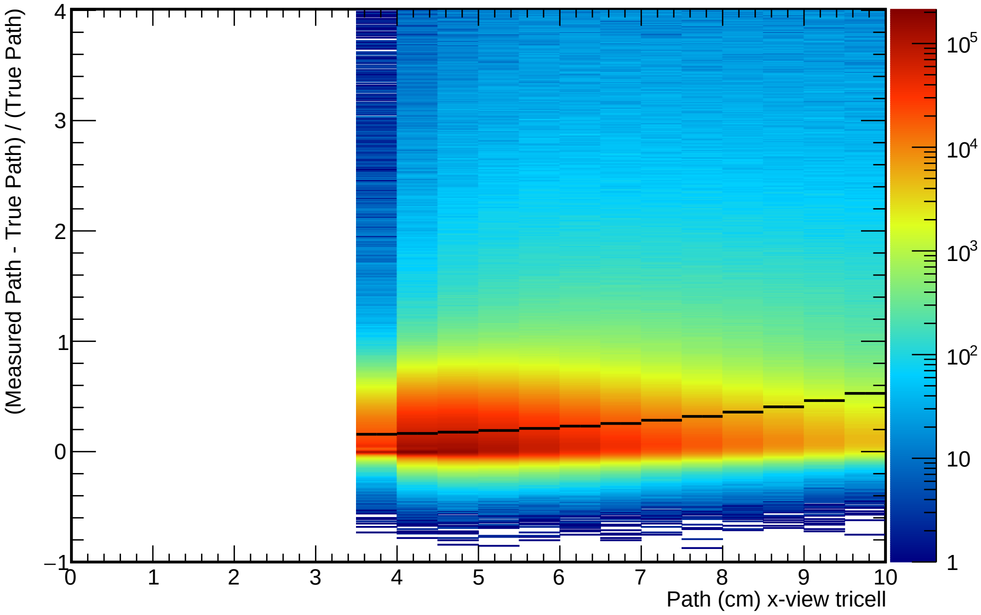

(a) x-view

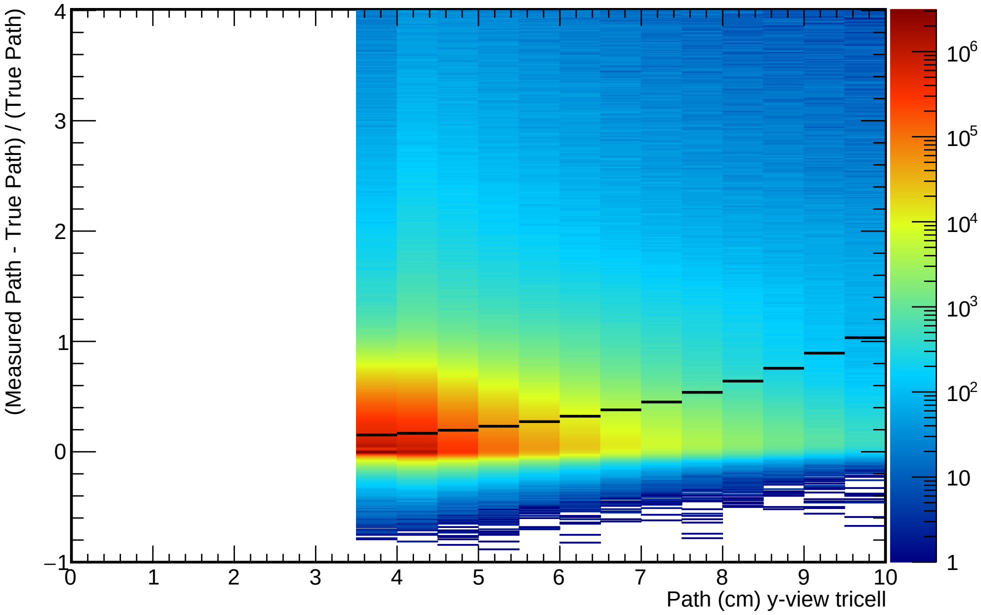

(b) y-view

Figure 4.6: The fractional difference in the the path reconstruction as a function of reconstructed path with the tricell method for x-view cells (a) and y-view cells (b). The black lines show the mean error for each length. Note there are no tricell hits with a path less than 3.56 cm as the reconstruction is limited by the physical widths of the cells.

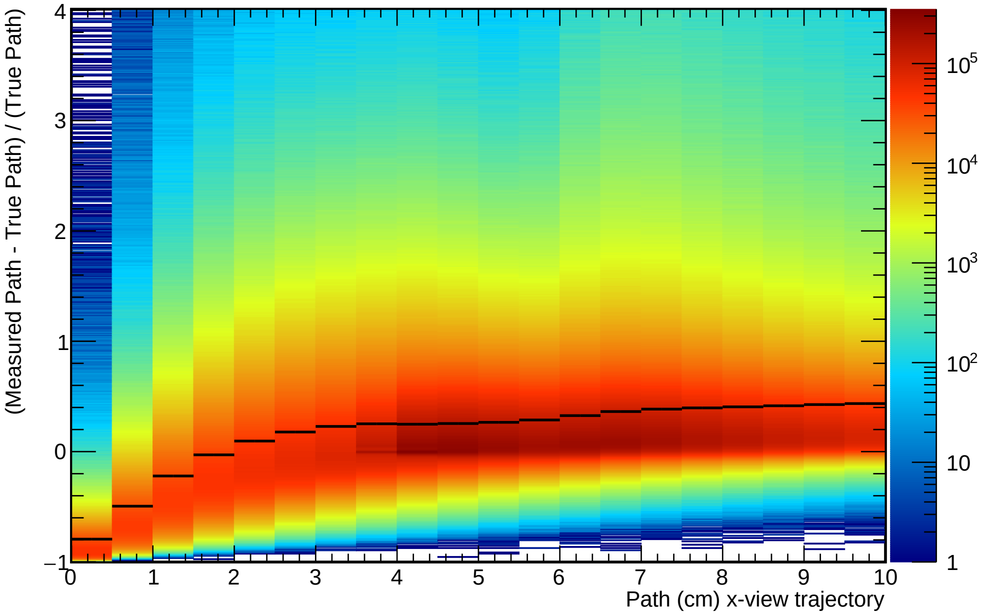

(a) x-view

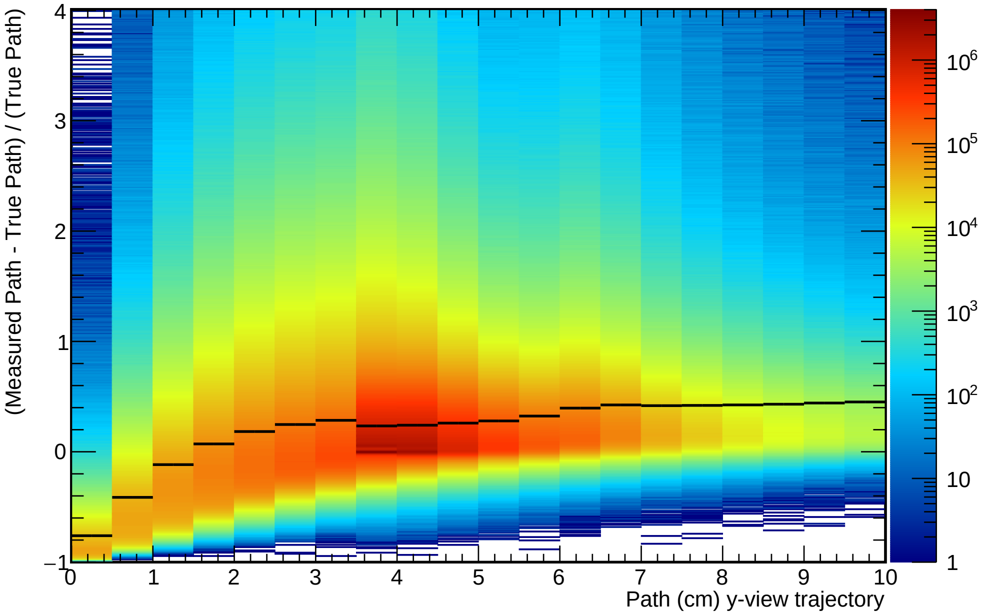

(b) y-view

Figure 4.7: The fractional difference in the the path reconstruction as a function of reconstructed path with the trajectory method for x-view cells (a) and y-view cells (b). The black lines show the mean error for each length.

additional hits included with the trajectory method are not of good quality reconstruction. Given these reservations we have chosen to use the tricell reconstruction method for our calibration.

4.6 Applying the Calibration

The first step of the calibration is the measurement of individual cell responses. We record the average number of photoelectrons produced per centimeter, PE/cm, as a function of position in the cell, w. We define w such that $w = 0\,\mathrm{cm}$ corresponds to the central z-axis of the detector and greater w is closer to the readout of the cell's APD. To calculate the PE/cm for a cell hit we use the tricell method described in §4.3. The average PE/cm as a function of w for the entirety of the ND and FD can be seen in Figure 4.9, but note that for the calibration these plots are produced for each individual cell. The average PE/cm changes as a function of the position in the cell primarily as a result of attenuation and threshold effects. As the photonic signal from an event travels though the wavelength shifting fiber it becomes attenuated and decreases in strength, leading to fewer photoelectrons produced in the APD. This effect is stronger the farther the photons are produced from the readout of the cell. The attenuation also introduces a threshold effect, where low energy cell hits produced farther away from the cell readout can only be seen if there is an upward fluctuation in the number of photoelectrons produced, meaning at low w we are biased to-

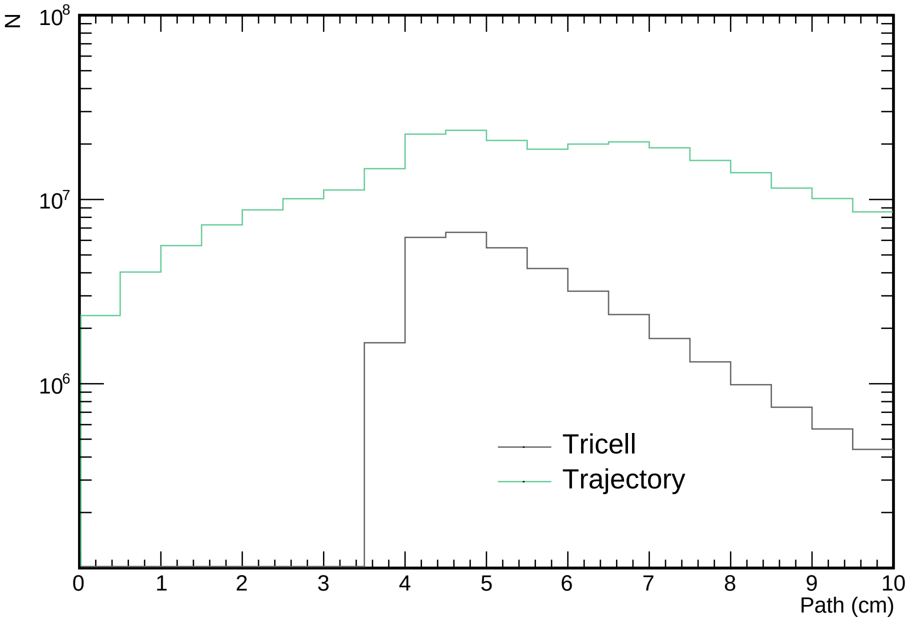

(a) x-view

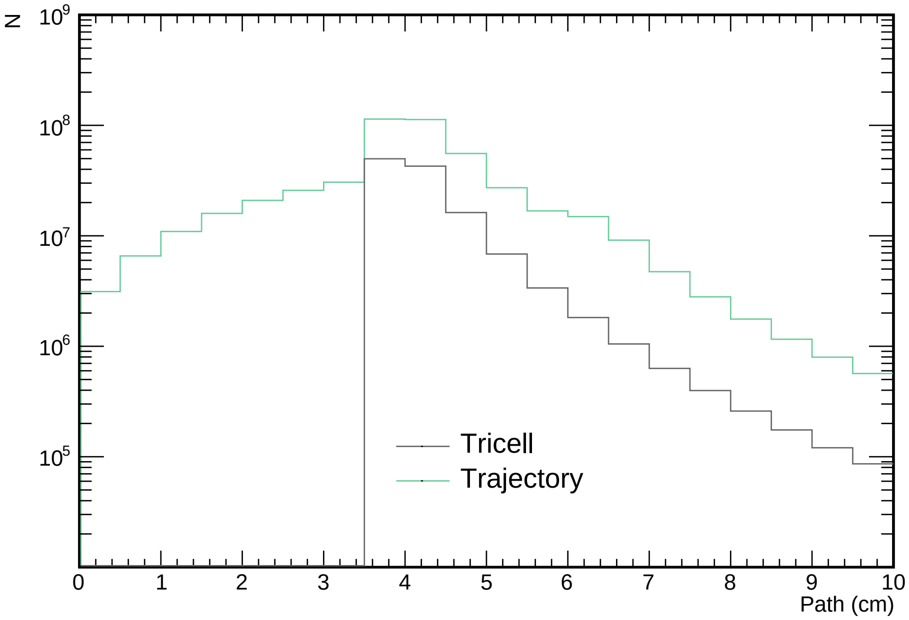

(b) y-view

Figure 4.8: The number of simulated cell hits which can be used for calibration as a function of the reconstructed path reconstruction as a function of reconstructed path length with the trajectory method for x-view cells (a) and y-view cells (b). Note there are no tricell hits with a path less than 3.56 cm as the reconstruction is limited by the physical width of the cells.

wards higher PE/cm. Each cell in the detector attenuates light differently, and so we assign a rating from 0 to 8 which we call the fiber brightness, with lower fiber brightness corresponding to shorter attenuation lengths.

In addition to the threshold effects, the fact that the cosmic ray muons are traveling downwards causes low energy muons to be filtered out before they reach the lower parts of the detector. This “shadowing” effect means that the hits at the bottom of the detector are biased towards higher energies, and thus higher PE/cm.

To account for the differences in electronic response in each cell due to the threshold and shadowing effects we look at MC simulated events where we have access to the truth information about the muon energy, and so can be used to correct for the bias in muon energy [31]. A function $T(w)$ is calculated for each cell by comparing the simulated number of photoelections produced by a given MC event to the number of simulated photons which would be seen at the readout in the absence of fluctuations, λ. We also compare the simulated true energy deposited in the cell, E_{true}, to the predicted energy using the average deposited energy of a minimally ionizing muon traversing a distance L in the cell $E_{\text{MIP}} = (1.70831\ \text{MeV cm}^{-1})L$.

$$T(w) = \left\langle \frac{PE_{\text{sim}}}{\lambda} \right\rangle_w \times \left\langle \frac{E_{\text{true}}}{E_{\text{MIP}}} \right\rangle_w \tag{4.4}$$

Equation (4.4) is then fit as a function of cell number and w for each view and fiber brightness separately. This fit of $T(w)$ is our threshold and shadowing

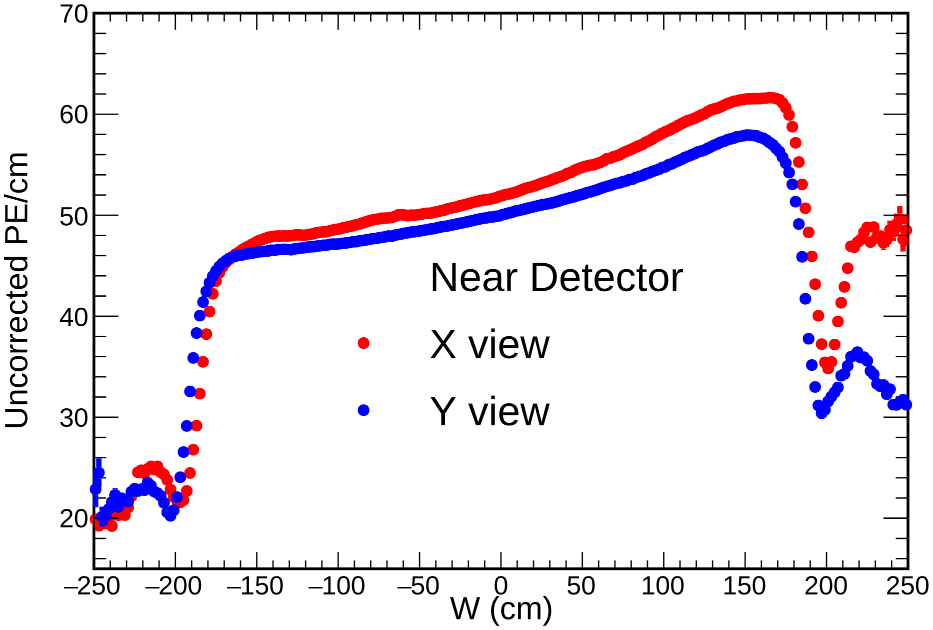

(a) Near Dectecor

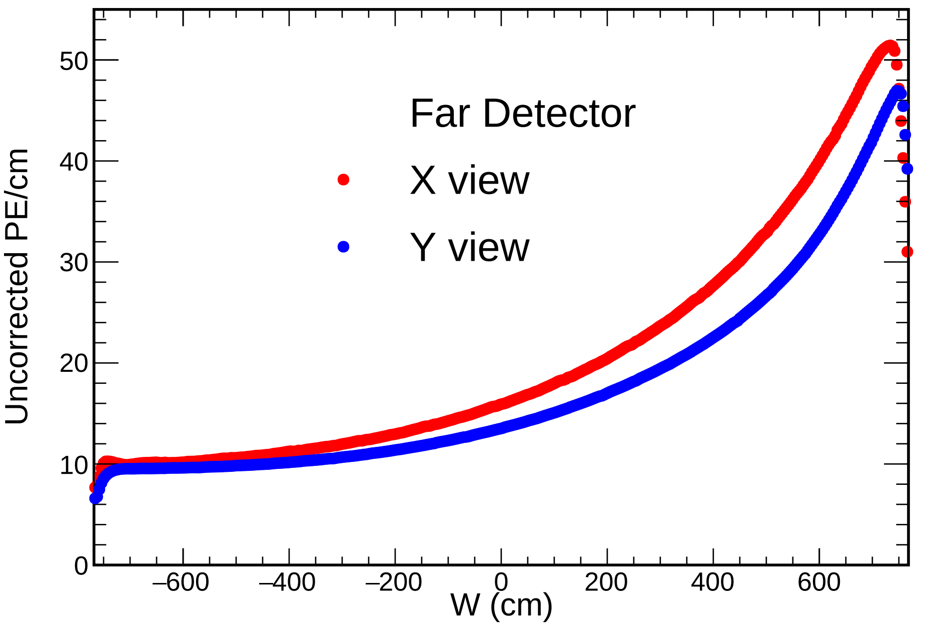

(b) Far Detector

Figure 4.9: The average detector response for the ND (a) and FD (b), separated into x—view (red) and y—view cells (blue). Note that detector response is higher for large w as we a closer to the cell readout [32].

correction. This is done to smooth out statistical noise in $T(w)$. Figure 4.10 shows plots of $T(w)$ averaged over each plane view.

To account for the attenuation effects in each cell the average number of photoelectrons per reconstructed path length produced in a cosmic ray cell hit is fit with a double exponential function

$$y_{\text{exp}} = A\left(e^{w/B} + e^{-(w-L_{\text{cell}})/B}\right) + C, \tag{4.5}$$

where L_{cell} is the length of the cell and A, B, and C are free parameters. The fit is performed in the region of $-150\,\text{cm} < w < 150\,\text{cm}$ for ND cells and $-750\,\text{cm} < w < 750\,\text{cm}$ for FD cells. However, this fit does not accurately model the detector response near the edges of each cell. To account for this defficency a twenty point tri-cubic local regression is performed on the ratio of data over y_{exp}. We obtain a curve which can serve as a multiplicative correction to y_{exp}. For a given w we interpolate between the twenty local regression points to construct a correction c_{interp}. A full estimate of the average photoelectrons per centimeter produced in a cell at a given w is then calculated as $c_{\text{interp}} \times y_{\text{exp}}$. An example of the full fit can be seen in Figure 4.11. A dimensionless normalization of 37.51 in the ND and 39.91 and in the FD is used to scale y_{exp} to obtain a correction factor to convert the PE/cm of a cell hit to a $PE_{\text{corr}}/\text{cm}$, which corresponds to a uniform energy deposition per unit length regardless of where in the detector the activity

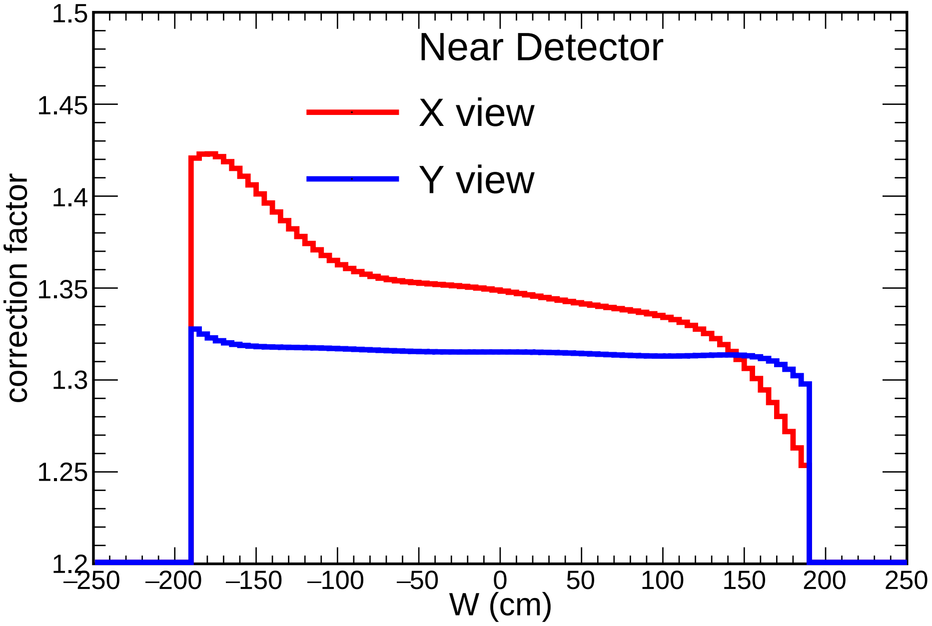

(a) Near Detector

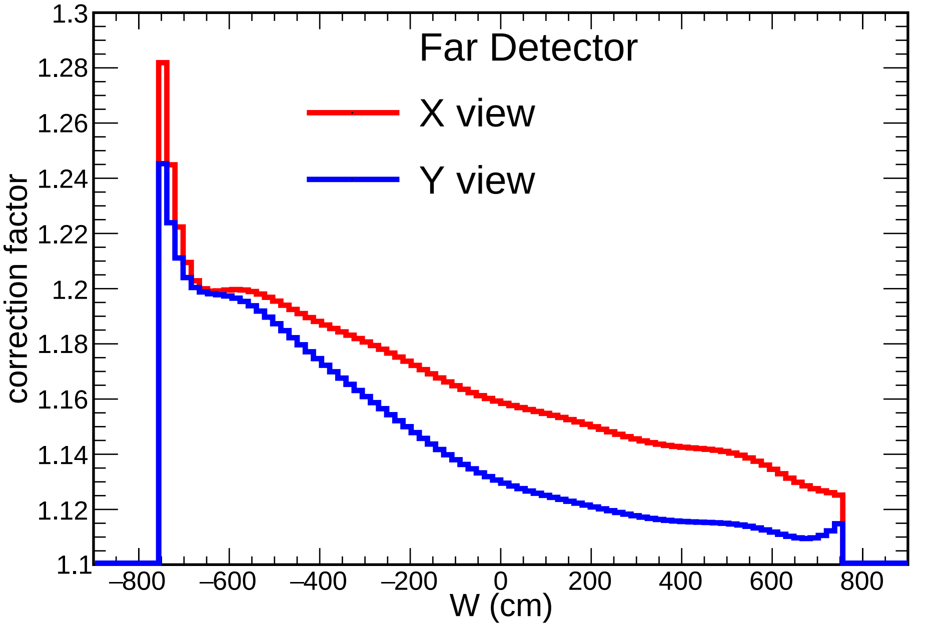

(b) Far Detector

Figure 4.10: Average threshold and shielding correction factor T as a function of position in the cell w. The red curves show are average over all x-view cells, while the blue is averaged over y-view cells. Note that low w corresponds to the end of the cell farthest from the readout, and so those ends require a stronger correction to deal with threshold effects [32].

was recorded.

$$\mathrm{PE}_{\mathrm{corr,ND}}/\mathrm{cm} = \frac{c_{\mathrm{interp}} \times y_{\mathrm{exp}}}{37.51}, \tag{4.6a}$$

$$\mathrm{PE}_{\mathrm{corr,FD}}/\mathrm{cm} = \frac{c_{\mathrm{interp}} \times y_{\mathrm{exp}}}{39.91}. \tag{4.6b}$$

The normalization factors are included so the average $\mathrm{PE}_{\mathrm{corr}}/\mathrm{cm}$ at $w = 0\,\mathrm{cm}$ is $1/\mathrm{cm}$. Once these uniform $\mathrm{PE}_{\mathrm{corr}}$ are established for each detector, all that remains is to convert this activity to an energy.

To convert $\mathrm{PE}_{\mathrm{corr}}$ to an energy is a simple matter of finding a scaling coefficient. This factor is calculated by finding the average $\mathrm{PE}_{\mathrm{corr}}/\mathrm{cm}$ produced in the data, and comparing it to the average simulated energy deposition per unit length. The reconstructed energy we associate with a cell hit is thus

$$E = \mathrm{PE} \times \frac{\left\langle \mathrm{MeV/cm}\big|_{\mathrm{MC}} \right\rangle}{\left\langle \mathrm{PE}_{\mathrm{corr}}\big|_{\mathrm{Data}} \right\rangle}. \tag{4.7}$$

To check the reliability of the calibration we look at the reconstructed $\frac{dE}{dx}$ for tricell hits in the penultimate meter of a stopping muon track. As this is the region where the energy losses are known to be 1.70831 MeV cm^{-1}, our calibrated energy should return a distribution peaked near this value. Figure 4.12 shows this distribution of tricell hits in the ND and FD for both the data and MC. The distribution peaks are near the expected value for both detectors, and the data and MC means agree to within 2%.

With this calibration method we have an accurate way to obtain the

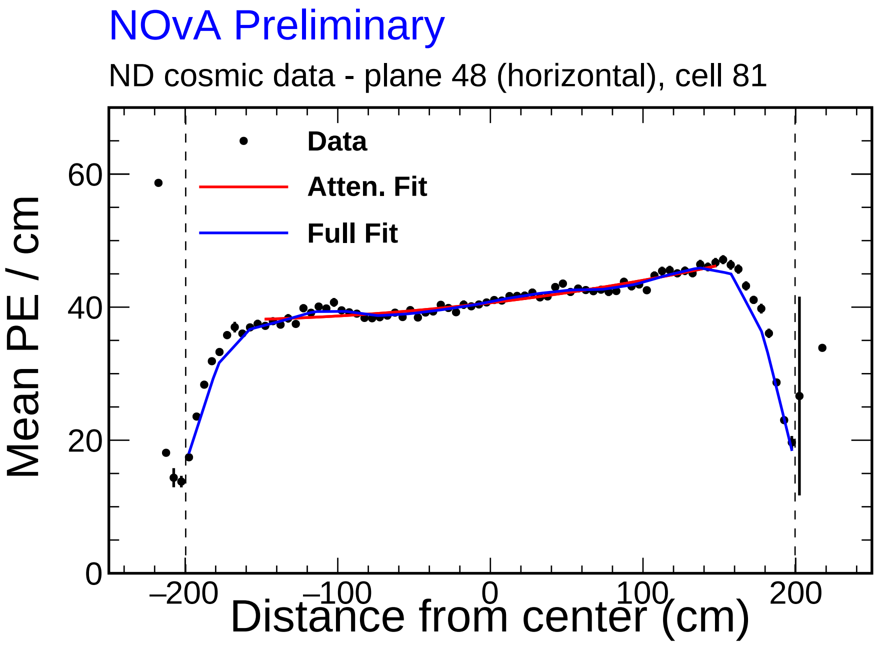

Figure 4.11: An example of the attenuation fit for ND cell 81 in plane 48. The dashed lines show the physical boundaries of the cell. Note that as the distance from the center of the cell, w, is a reconstructed quantity some cell hits are reconstructed with unphysical w. The red curve shows the result of fitting the data with Equation (4.5) for $-150\,\mathrm{cm} < w < 150\,\mathrm{cm}$. The ratio of the data to red curve is then fit with a twenty point tri-cubic local regression to obtain a second order correction. The full fit including this correction is shown in blue [32].

energy deposited in a scintillating cell. This forms the basis for constructing the energy of neutrino interaction event in the detector. However, the energy of a neutrino event cannot be assumed to be the sum of energies in the cell hits composing the event as there are inefficiencies in the reconstruction of neutrino interactions. These inefficiencies can lead to either missing energy from the neutrino or to erroneously attributing unrelated

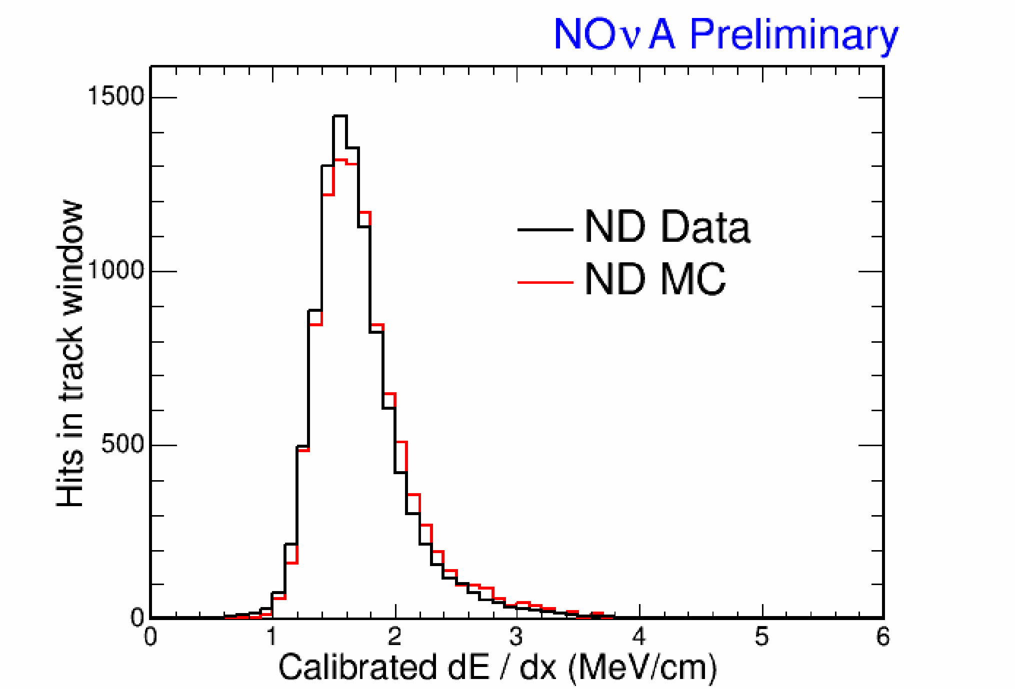

(a) Near Detector

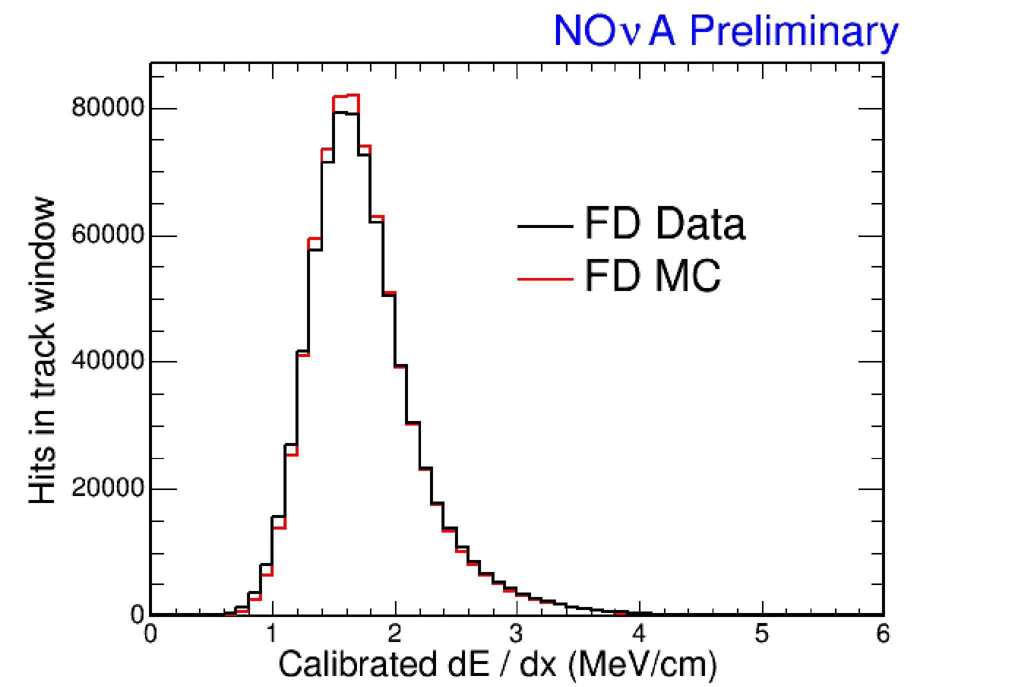

(b) Far Detector

Figure 4.12: The distribution of reconstructed $\frac{dE}{dx}$ for tricell hits in the penultimate meter of a stopping muon track for data (black) and MC (red) in the ND (a) and FD (b) [33]. The plots have been normalized so there are the same number of events in the data and MC. The data and MC agree on the mean of the distributions to within 2% for both detectors [34].

detector activity to the neutrino. To properly estimate the neutrino energy we must proceed with more care. This estimation process will be described in Chapter 6, but requires already defining the event selection used in the analysis.

Chapter 5

Event Selection

For the sterile neutrino search we measure the energy spectra of charged current interactions from muon neutrinos and the neutral current interactions from all neutrinos. Previous NOvA analyses have already developed selection criteria for ν_μCC and ν_eCC events [35]. We use the same sample of ν_μCC events except we do not separate them into quantiles based on the fraction of the energy deposited into the hadronic system. Previous analyses use four quantiles to improve the energy resolution, but we found that we gained no additional sensitivity to sterile neutrinos by doing so. Instead we combine the four quantiles to increase our statistics in each energy bin.

Our NC selection was developed specifically for this analysis, designed with a search for sterile neutrinos in mind. Our chief concerns with the NC selection are removing poorly reconstructed events, ensuring maximal energy deposited in the detector, and rejecting background events. In a

NC interaction the neutrino deposits a fraction of its energy, y, into the hadronic system, with the outgoing neutrino retaining the remaining energy. We define the energy deposited in the detector as

$$E_{\text{dep}} = y \times E_{\nu}. \tag{5.1}$$

Since we cannot detect the outgoing neutrino, we optimize our selection to measure the deposited energy.

At a conceptual level we can divide the event selection processes into several stages: quality, containment, and signal/background separation. Starting with an event formed from a collection of cell hits which have been grouped together based on their proximity in time and space [36], we ensure that these hits can be properly reconstructed into something which qualitatively looks like a neutrino interacting in the detector. Next we remove events which we believe did not deposit all of their energy in the detector. In the FD we remove cosmic background events; as the ND is underground we have effectively no cosmic background events in that sample. Finally, we use machine learning algorithms to identify the events which look most NC-like. These criteria taken together form the full NC event selection.

We designed the selection by looking at our simulation and defining our signal as true NC events whose interaction vertices were within the boundaries of the detector. All other events were taken as background.

The selections were defined separately in the ND and FD to account for the different backgrounds, beam angle, and detector geometries.

This is a blinded analysis [37], and so we do not look at the data collected by NOvA which will be used in the analysis until the analysis framework is finalized and approved by the collaboration. As such we cannot examine the full effect of our selection on the data. However, 10% of the ND data was designated to be studied and not used in the final analysis. We did not set aside any data in the FD as the event rate is much lower there than in the ND and every event is needed for the analysis. These data allow us to have some understanding of what effects the ND selections have on our sample, but we gain no such understanding for the FD selections.

5.1 Neutral Current Selection

5.1.1 Near Detector Selection

5.1.1.1 Event Quality

We first check the reconstruction of each event along several axes. We must be able to locate a vertex where we believe the interaction took place, ensure that something "particle-like" emerges from said vertex, and require that the event extends into multiple planes. To obtain a vertex we apply a Hough Transformation to locate the position which looks most like the origin of the cell hits [38, 39]. In general this process looks for lines in collections of points by considering the set of all possible lines passing through each individual point. For our purposes we are looking at trajectory points in the x-z and y-z planes. Each of these lines has some distance of closest approach to the origin of the coordinate system. If there are collinear points in the collection they will share a line and hence a distance of closest approach. A line exist when there is a peak in the distribution of distances of closest approach. By finding lines in the x-z and y-z planes we can construct a vertex from their common origin in three dimensional space. If a vertex cannot be found then the event is discarded.

Once a vertex is located we attempt to reconstruct prongs in the event. These prongs are collections of cell hits in the x-view and y-view which are designed to capture the energy deposited by the daughter particles of the interaction. Using a fuzzy k-means algorithm we cluster cell hits within the event into track-like collections which appear to stem out of the reconstructed vertex [40]. Prongs are later to be classified by a CVN to identify the probable daughter particle which is responsible for the energy depositions in the prong. This process of identifying the daughter particles of the interaction is crucial to the event reconstruction. As such we require at least one prong be found.

We also require that the event has cell hits in at least three planes of the detector. The NOvA detectors are tracking calorimeters and, as described in §3.2, to reconstruct the trajectories of particles we need to see activity in both the x-view and y-view planes. To ensure we can accurately reconstruct

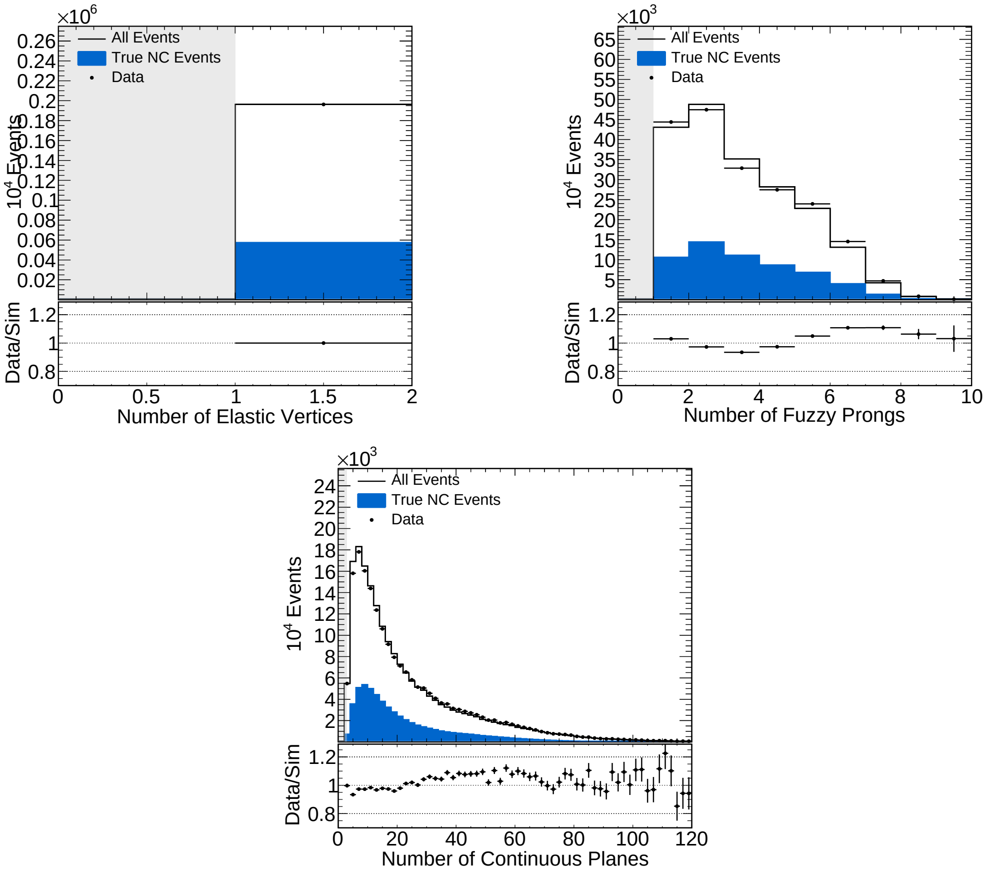

Figure 5.1: Comparisons of data and simulation for the ND quality requirements. The true NC events are highlighted in blue, and the removed regions are shown as grey boxes. The simulation is normalized to have the same number of events as the data.

the event we require that the event spans at least 3 contiguous planes.

The plots in Figure 5.1 show the distribution of the variables used in the selection criteria as well as their selection limits. We also compare the simulation to the ND data not used in the analysis and find that there are shape differences on the order of 10% for all criteria.

5.1.1.2 Containment

There are two main ways we could fail to contain an event—firstly, the event could originate outside the detector, in which case we would see only the fraction of the event that made it into the scintillator; secondly, the particles produced by the event could escape the detector, in which case they will carry away energy we cannot hope to measure. The containment of the event is thus based on reducing the frequency of these two cases.

We look at the reconstructed vertex position within the detector to remove events which originated outside the detector. We refer to such events as “rock” events as they primarily occur from neutrinos interacting with the rock surrounding the ND producing particles which then are mistaken for events originating inside the detector. Using the coordinate system defined in §3.2, we restrict our sample to events whose vertices are contained in the region $-100\,\text{cm} < x < 100\,\text{cm}$; $-100\,\text{cm} < y < 100\,\text{cm}$; and $150\,\text{cm} < z < 1000\,\text{cm}$. Figure 5.2 shows the distribution of these quantities for events passing the criteria of §5.1.1.1.

We also constrain how close we allow the outgoing particles to get to the walls of the detectors. To maximize E_{dep}, we looked at the energy in our simulated NC events which is visible to the detector, E_{vis}. This visible energy is not the calorimetric energy defined in Chapter 4; instead it is the amount of energy deposited in the scintillator within the simulation. Since E_{vis} does not account for the energy deposited in the non-active material in the detector, we expect $E_{\text{vis}} \sim 0.58 E_{\text{dep}}$ [41]. However, this ratio will only

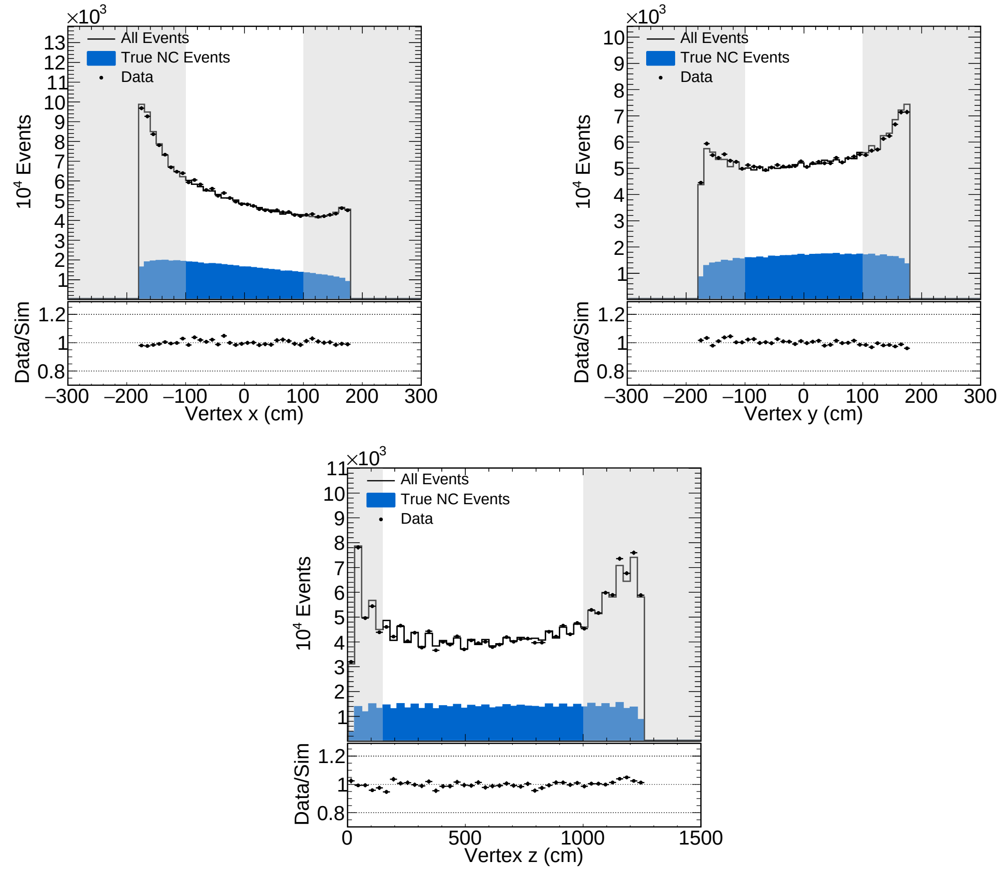

Figure 5.2: Comparisons of data and simulation for the ND vertex positions, with the NC signal events in blue. Note that the simulation has been normalized to match the number of events in the data. The removed regions are shown as grey boxes. These plots have the quality requirements outlined in §5.1.1.1 already applied.

hold for events which are fully contained in the detector. When the event is poorly contained and particles leave the detector the value of E_{vis}/E_{dep} drops. Since we expect that more particles will escape the detector when the reconstructed prongs are closer to the edges of the detector, we can plot the average E_{vis}/E_{dep} as a function of the minimum distance of each event's prongs to any edge of the detector. These plots can be found in Figure 5.3 and show that as this distance goes to zero, E_{vis}/E_{dep} drops slightly. We see that the distributions for the top, bottom, East, and West edges flatten out when the prongs are 20 cm from the edges. The back edge of the detector has a slightly stricter requirement of 50 cm to ensure the events are not lost in the muon catcher. We see a pronounced falloff in the ratio for events which are closer than 150 cm to the front of the detector, and so we remove all such events. The remaining volume is called the *fiducial volume* of the ND. The distributions of events passing the quality criteria of §5.1.1.1 are shown as a function of minimum prong distance to each detector edge in Figure 5.4.

5.1.1.3 Signal Selection

For the signal selection we use a convolutional visual network (CVN) which has been trained to recognize NC-like neutrino interactions [42]. The CVN score ranges from 0 to 1 and gives a measure of how much an event looks like a NC interaction, with 1 being most NC-like and 0 being least NC-like. The distribution of CVN scores can be seen in Figure 5.5. We select only

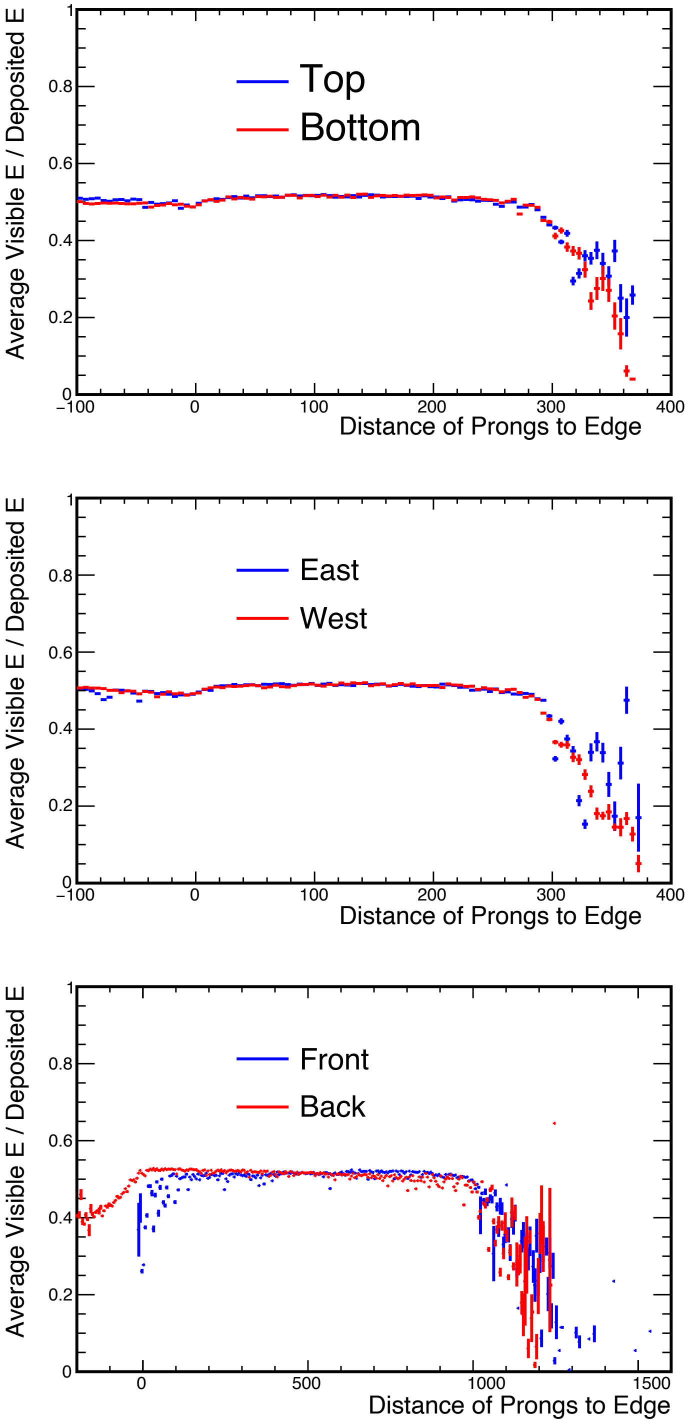

Figure 5.3: The average fraction of E_{vis}/E_{dep} in our ND simulation as a function of the minimum distance of the prongs from each detector edge. Note that there are negative values of the prong distance to edge due to errors in the prong reconstruction.

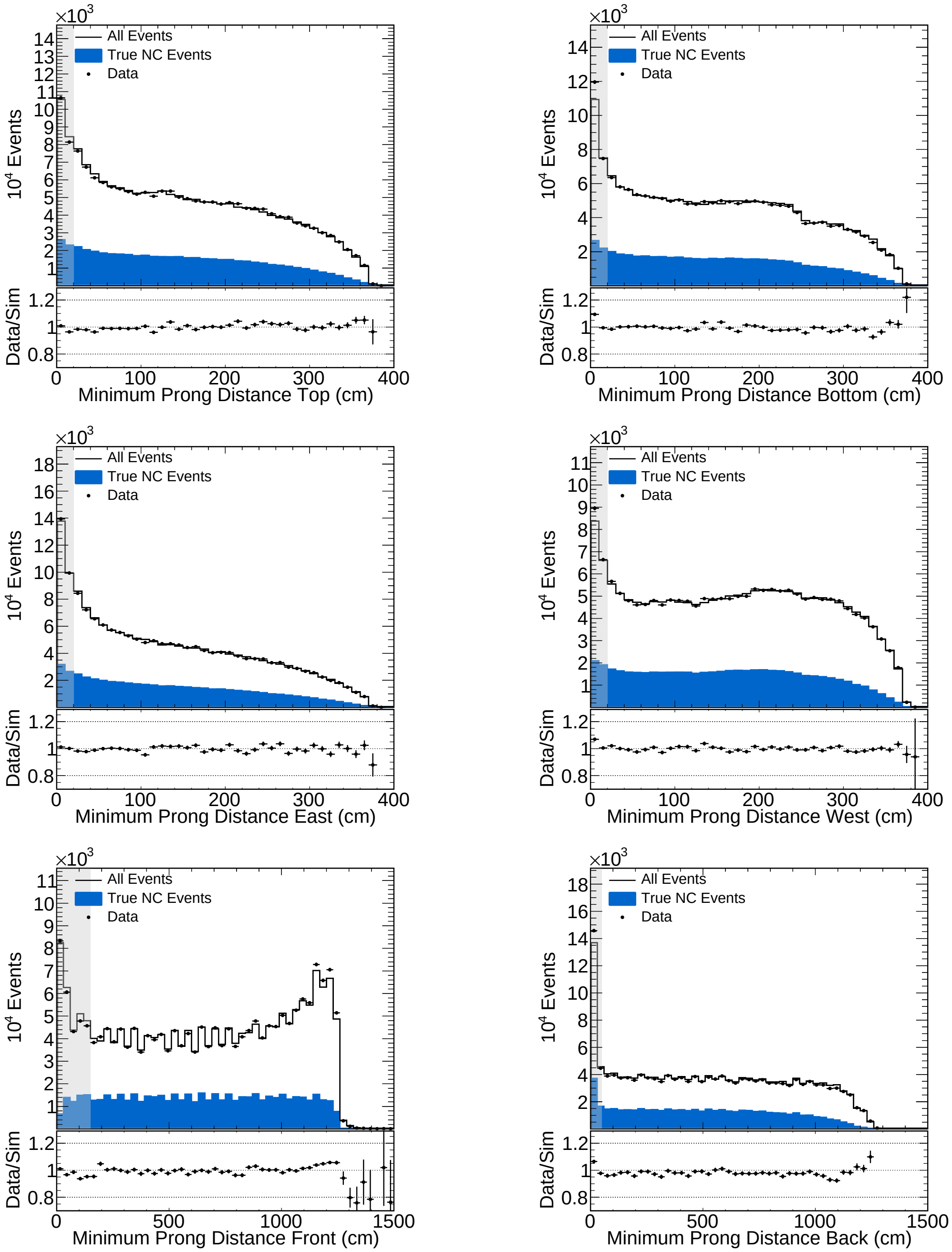

Figure 5.4: Comparisons of data and simulation for the minimum distance of any prong to each detector edge. Here, the true NC events are in blue, and the removed regions are shown as grey boxes. Note that the simulation has been normalized to have the same number of events as the data. In these plots, the event quality requirements of §5.1.1.1 and vertex position demands have been applied.

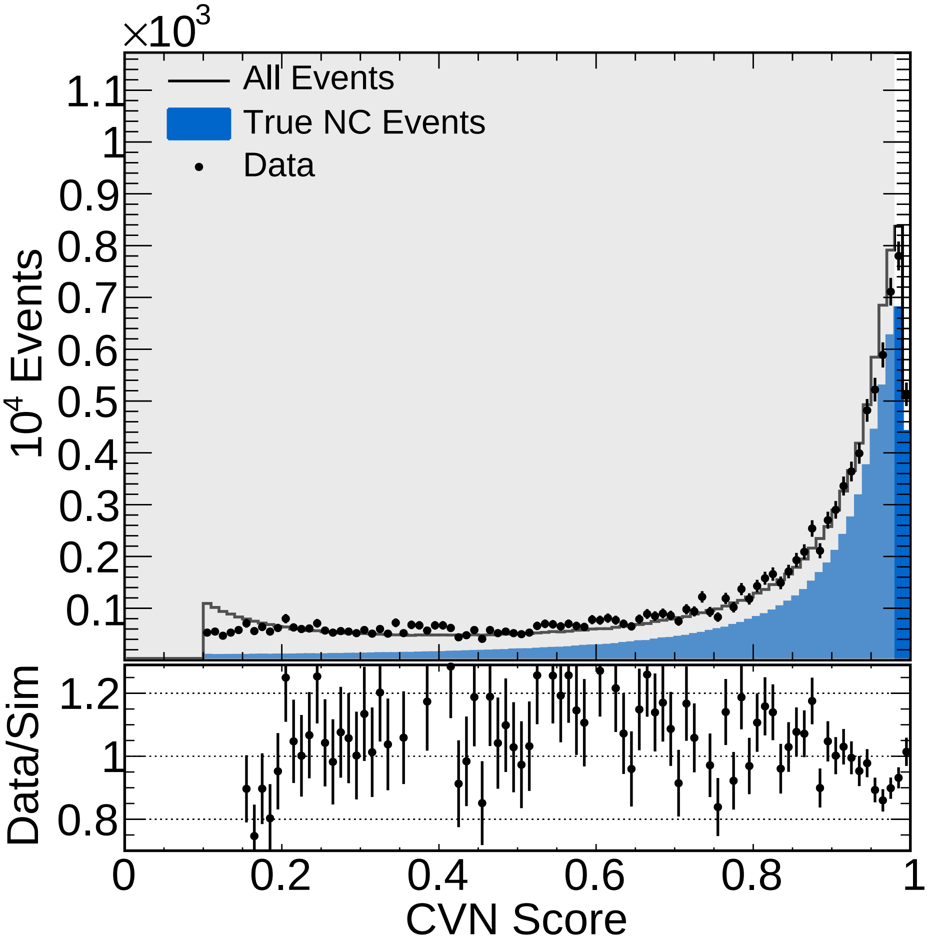

Figure 5.5: Comparisons of data and simulation for the CVN score for the ND. Here, the true NC events are in blue, and the removed region is shown as a gray box. Note that the simulation has been normalized to have the same number of events as the data. These plots have the event quality and containment requirements applied as outlined in §5.1.1.1 and §5.1.1.2 respectively.

events with a CVN score greater than 0.98. The reason for this value will be elaborated on in §5.1.2.3 as it relates to the FD selection.

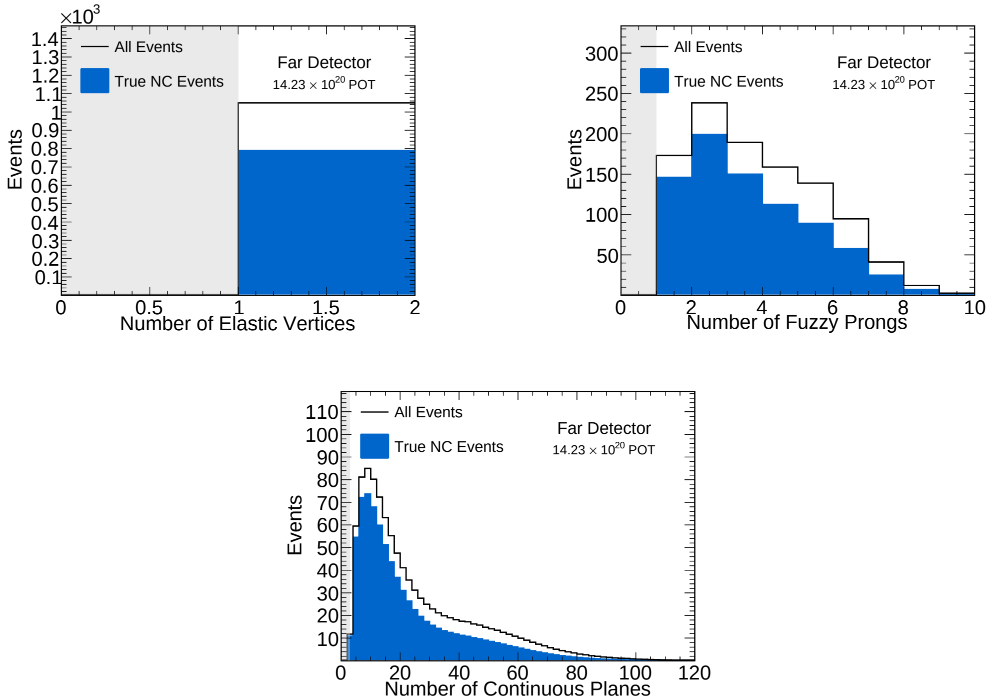

Figure 5.6: Distributions for the variables used in the FD event quality requirements. The true NC events are highlighted in blue, and the removed regions are shown as grey boxes.

5.1.2 Far Detector Selection

5.1.2.1 Event Quality

The FD event quality requirements are identical to those for the ND outlined in §5.1.1.1. Figure 5.6 shows the distribution of the number of vertices, number of prongs, and number of contiguous planes. As with the ND, we remove events with no reconstructed vertex or prongs, and events with fewer than 3 contiguous planes.

5.1.2.2 Containment Requirements

Unlike the ND requirements in §5.1.1.2, we do not use the vertex position directly to determine the containment of FD events. Instead the vertex position is used in rejecting cosmic background events which are more prevalent in the FD. The way the vertex position is used is described in §5.1.2.3.

We still use the minimum distance between the event's prongs and the walls of the detector as a containment criterion. The distributions for the average fraction of visible energy, $\langle E_{\text{vis}}/E_{\text{dep}}\rangle$, for FD events are shown in Figure 5.7 and show the same decline in $\langle E_{\text{vis}}/E_{\text{dep}}\rangle$ as the distance to the edge becomes smaller. We remove events whose prongs get closer than 100 cm to the top, bottom, East, or West edges or 160 cm to the front or back edges. The remaining volume is the fiducial volume for the FD. These requirements and the distributions can be seen in Figure 5.8.

5.1.2.3 Cosmic Ray Muon Rejection and Signal Selection

As cosmogenic muons are a significant background in the FD we require additional handling to remove. As well as a CVN selection similar to that used in §5.1.1.3, we also use a boosted decision tree (BDT) to help us separate true NC events from the cosmic ray background events. The cosmic ray background rejection BDT was trained on twenty event variables using the TMVA package [43]. The training variables are

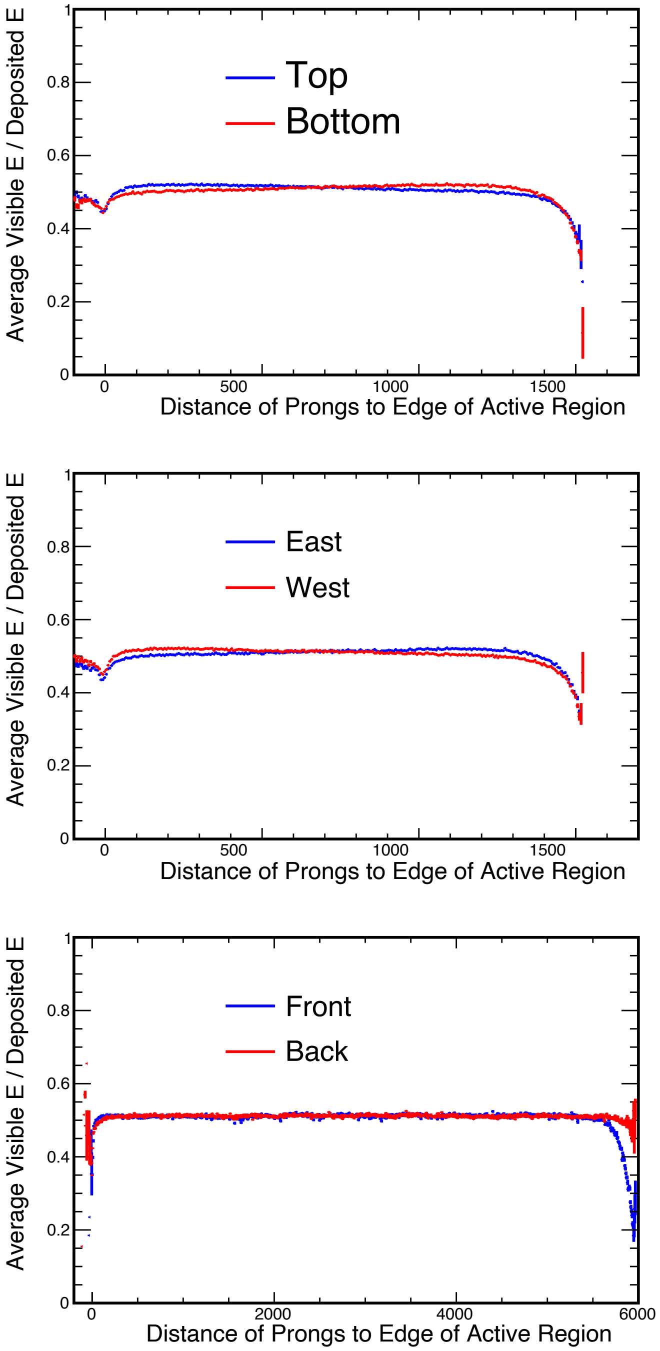

Figure 5.7: The average fraction of E_{vis}/E_{dep} in our FD simulation as a function of the minimum distance of the prongs from each detector edge. Note that there are negative values due to errors in the prong reconstruction.

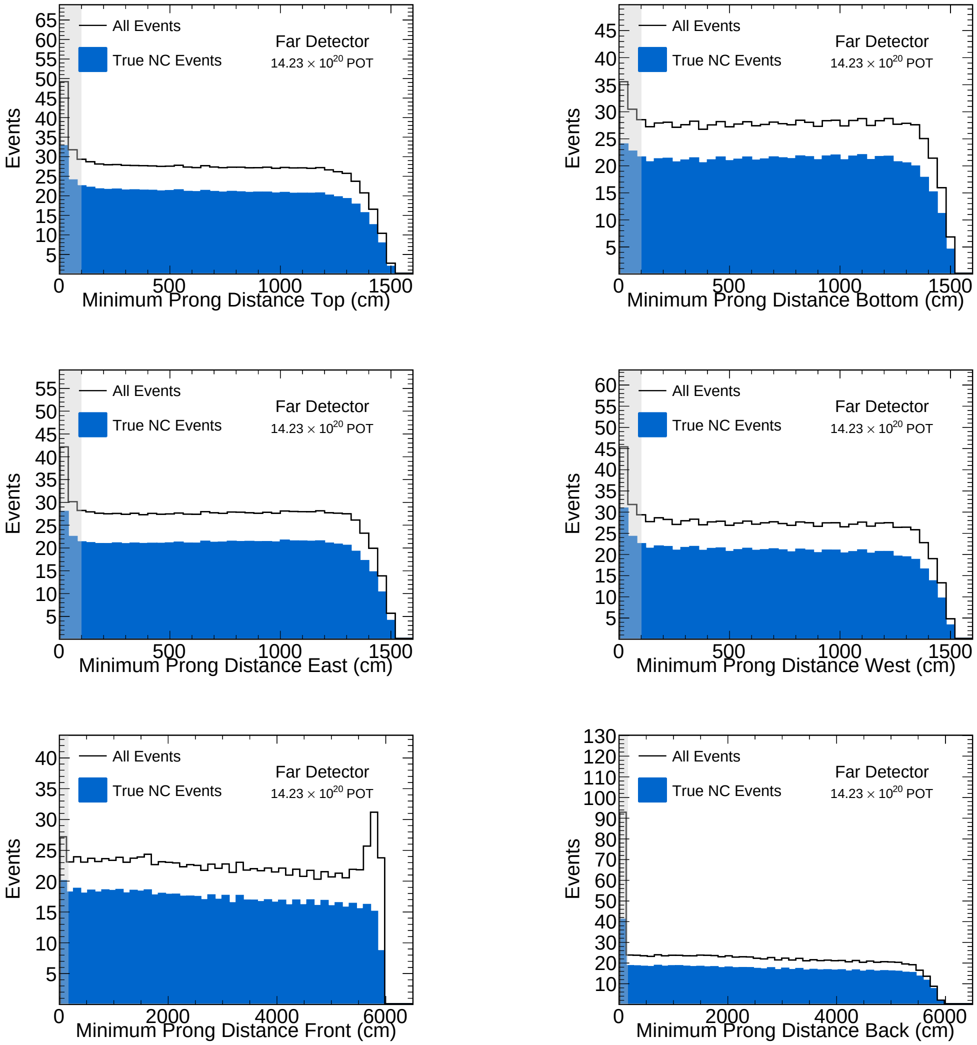

Figure 5.8: Distributions for the minimum distance of any prong to each edge of the FD. Here, the true NC events are in blue, and the removed regions are shown as grey boxes. In these plots, the quality requirements of §5.1.2.1 have been applied.

1. the vertex position in x, y, and z
2. the number of contiguous planes
3. total number of hits in the event
4. the number of hits per plane
5. the number of hits whose energy range is like those in the penultimate meter of a muon track
6. momentum fraction transverse to the beam
7. how separated the event is to the nearest event in both time and space
8. number of reconstructed showers
9. calorimetric energy of the reconstructed showers
10. distance between the vertex and the closest reconstructed shower
11. the shower $y-$direction cosine
12. the shower length
13. the shower width
14. and the number of hits in both $x-$planes, $y-$planes, as well as the difference and ratio of the two

Distributions of variables 1 through 7 and 14 can be seen in Figure 5.9 while the distribution of variables 8 through 13 are in Figure 5.10. By looking

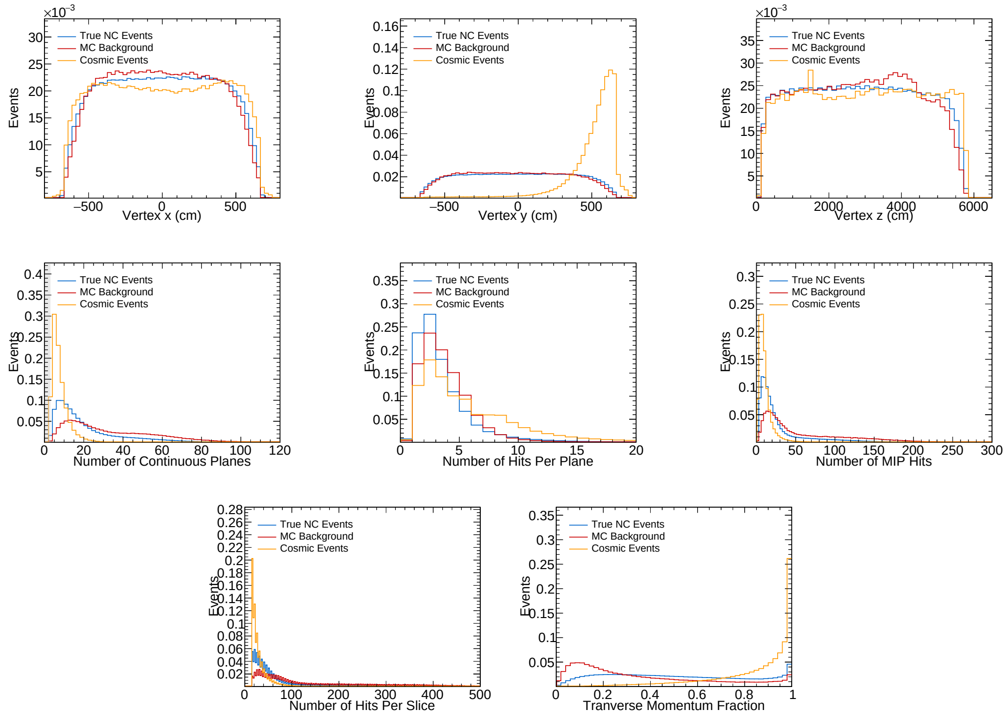

Figure 5.9: Variables 1 through 7 and 14 used in the BDT training. These distributions are normalized to have one event and have requirements described in §§5.1.2.1-5.1.2.2 applied to them.

at these variables the BDT ranks how likely the event is to be a NC event instead of a cosmic background event.

To choose the values of the CVN and BDT scores to use for our selection we use a figure of merit which takes into account the number of signal events in the i-th bin in the energy spectrum, S_i, the number of background events, B_i, and the total systematic and statistical uncertainty for that bin, σ_i

$$\mathrm{FOM} = \frac{1}{N}\sum_{i} \frac{S_i}{\sqrt{S_i + B_i + \sigma_i^2}}, \tag{5.2}$$

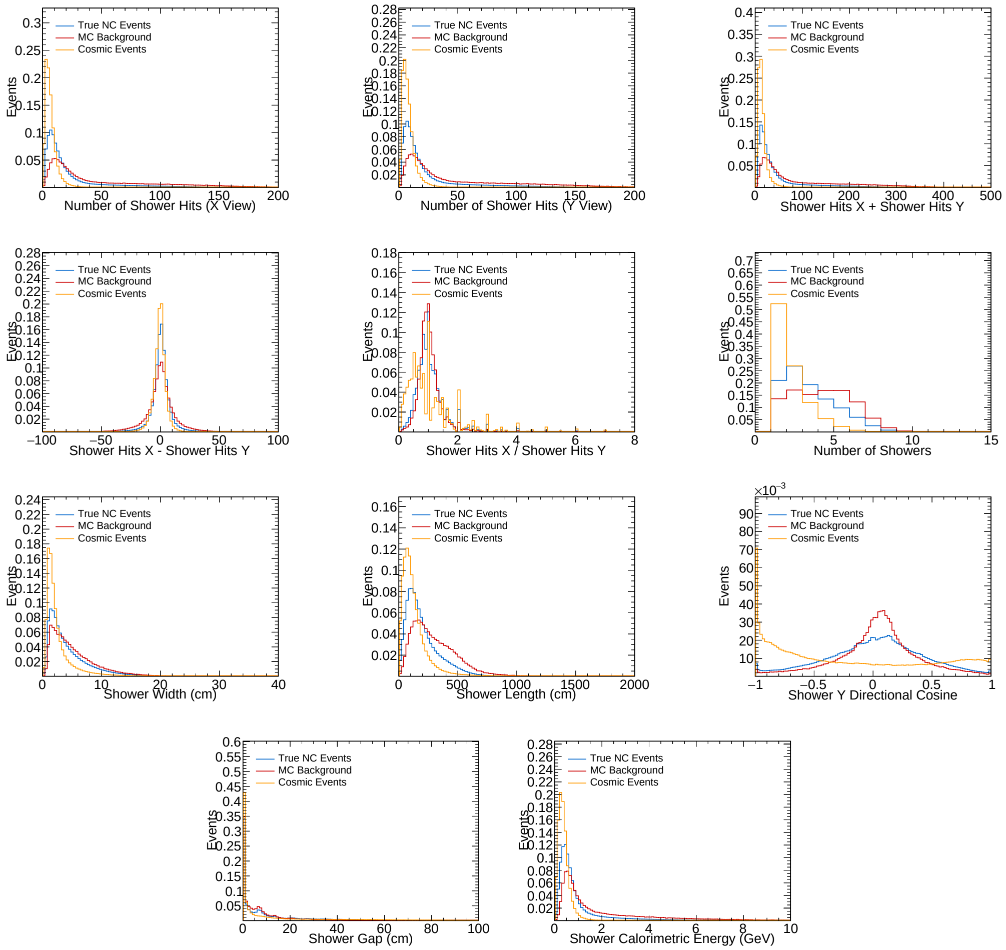

Figure 5.10: Variables 8 through 13 used in the BDT training. These distributions are area normalized and have requirements described in §§5.1.2.1-5.1.2.2 applied to them.

where N is the number of bins in the spectrum. The uncertainties were calculated by decorelating a covariance matrix to obtain an effective per bin uncertainty σ_i. This processes will be described in Chapter 7. The covariance matrix relies on simulating expected neutrino spectra, and the matrix used for this processes was generated with an older version of our simulation and is not the same as the covariance matrix which is used in this analysis. We used an older version of our simulation since the covariance matrix for the current simulation was still in development at time we were constructing our selection. We expect this choice to have minimal impact on the analysis as the general shape of the systematic uncertainties should be similar.

In optimizing our figure of merit, FOM, we maximize the number of signal events in each bin while minimizing the backgrounds and their uncertainties. Since the uncertainties from the covariance matrix are calculated using both the ND and FD spectra we calculate the optimal CVN scores used in the ND and FD selections simultaneously. After maximizing the FOM we find the optimal values are 0.98 for the ND CVN, 0.1 for the FD CVN, and 0.85 for the cosmic rejection BDT. The distribution of FD CVN scores and cosmic rejection BDT scores can be seen in Figure 5.11.

5.1.3 Selection Summary

We require that our NC events are taken only from the sample of events which are not already ν_eCC or ν_μCC selected to ensure that we do not use the same event in two samples. We developed selection criteria based on

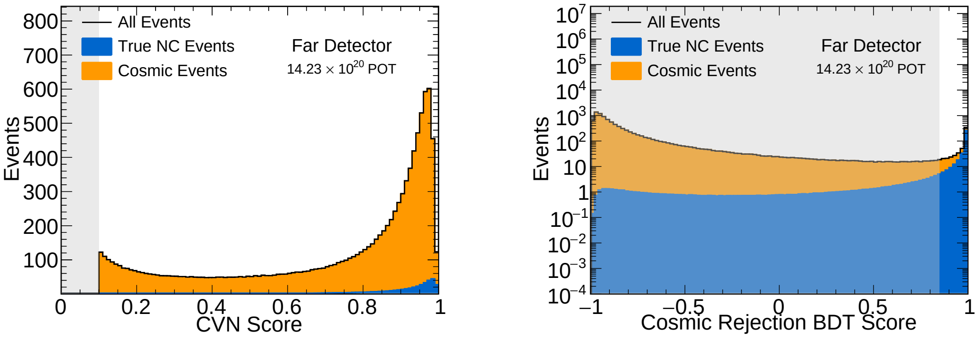

Figure 5.11: Distributions for the FD CVN and cosmic rejection BDT scores. Here, the true NC events are in blue, the cosmic background events are shown in orange, and the removed regions are shown as grey boxes. These events have the requirements described in §§5.1.2.1-5.1.2.2 applied to them.

event quality to ensure our events can be reconstructed accurately. We also determined boundaries in the ND and FD that allow us to remove uncontained events—events with activity beyond these boundaries likely have particles which escaped the detector and so we cannot accurately estimate the event's energy. Finally we made use of CVNs and BDTs to separate our signal and background. The critical values for the CVNs and BDTs were determined by optimizing our signal with the constraints of our backgrounds and systematic uncertainties. All events which satisfy these conditions are included in our NC selection.

Once our NC sample is defined, we need to reconstruct the energy of each event in our sample to create our data spectrum.

Chapter 6

Neutral Current Event Energy Estimation

When a neutrino of energy E_ν interacts via the exchange of a Z boson there is no charged lepton in the final state. Instead there is a shower of hadrons which carry a fraction of the incoming neutrino energy, y, and the neutrino deposits an amount of energy $E_{\text{dep}} = y \times E_\nu$ into this hadronic shower. The outgoing neutrino carries away an immeasurable amount of energy $(1 - y) \times E_\nu$. Since it is not possible to directly measure E_ν for a NC interaction we do not attempt to estimate it during NC event reconstruction. Instead we only attempt to estimate E_{dep}.

An energy estimator is a function of reconstructed quantities from an event which calculates an energy, E_{est}, which we use as an estimate of E_{dep}. The goal is to construct a function such that the difference between E_{est} and

E_{dep} is small for as many events as possible. To determine the quality of an estimator we look at distributions of

$$\frac{\Delta E_{\mathrm{dep,est}}}{E_{\mathrm{dep}}} \equiv \frac{E_{\mathrm{est}} - E_{\mathrm{dep}}}{E_{\mathrm{dep}}}. \tag{6.1}$$

For a good estimator, Equation (6.1) should be narrowly and symmetrically distributed about zero. The narrowness in the distribution indicates a precise estimator, while being distributed about zero indicates an accurate estimator.

It is important to look at only true NC events passing our selections, as outlined in Chapter 5.1.2, when developing the energy reconstruction as we want to base our estimate only on the selected signal. Additionally, we can underestimate E_{dep} due to particles carrying energy outside of the fiducial volume of the detector and causing us to not have enough information to properly reconstruct the event. Such events are said to be uncontained and are impossible to accurately reconstruct. Instead, an energy estimator only accounts for inefficiencies in capturing the energy of showers contained within the detector, not in our ability to contain events. Any estimator is applied to events which we believe are contained; an estimator which tries to account for energy outside of the detector will lead to an overestimation of E_{dep} for events which are fully contained. To this end, we only consider events which have a true vertex within the detector, as this requirement is a good proxy for contained events after applying our selection. As part of the NC selection we exclude events producing particles that deposit energy near the detector edges. This selection means that events originating right on a detector edge are not a concern because they will produce particles depositing energy near the edge of the detector.

The task of developing an energy estimator is thus to use the reconstructed quantities of the selected events and construct an accurate and precise estimate of E_{dep} from those quantities. Truth information may be used in motivating our estimator, and in fact must be used as E_{dep} is known only from truth information, but the calculation of the estimate E_{est} can only use reconstructed quantities. Many estimators were considered for this analysis, with the preferred estimator described in §6.2.

6.1 Candidate Energy Estimators

6.1.1 Calorimetric Estimator

When a neutrino interaction occurs in the detector the observed energy is called the calorimetric energy, E_{cal}. This quantity is simply the sum of the calibrated energy depositions described in Chapter 4. We can use E_{cal} as an estimate of E_{dep}. One complication is that it is difficult to fully capture the energy in hadronic showers as they contain neutrons. Neutrons do not directly ionize the scintillator in the detector and can only deposit energy when the neutron collides with a nucleus. These collisions occur sporadically, and so the energy depositions from neutrons are not easily as-

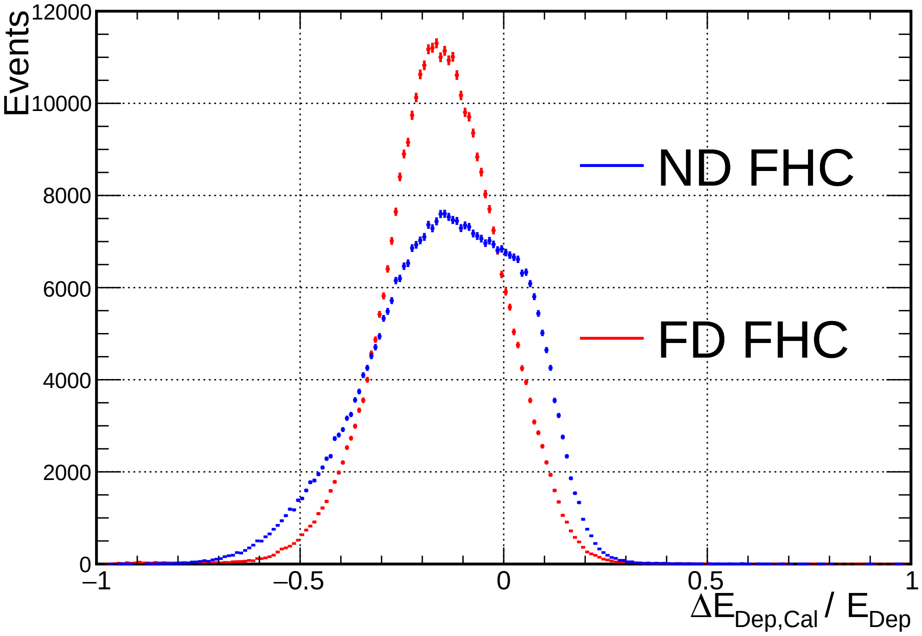

Figure 6.1: The distribution of $\Delta E_{dep,cal}/E_{dep}$, for true NC events passing the full selection and having an interaction vertex inside the detector for the ND (blue) and FD (red). An accurate, unbiased estimator would result in a symmetric distribution peaked at zero. Clearly, E_{cal} underestimates E_{dep}.

sociated with a neutrino interaction during reconstruction. Because of this reconstruction deficiency, E_{cal} is not an accurate measure of E_{dep}. We can see how well E_{cal} approximates E_{dep} from the distribution of $\Delta E_{dep,cal}/E_{dep}$ in Figure 6.1. This distribution shows that E_{cal} is lower than E_{dep} in 75% of Near Detector (ND) events and and 85% of Far Detector (FD) events. Because E_{cal} is not an effective measure of E_{dep} we need to develop a way of better estimating E_{dep}.

6.1.2 Linear Estimator

In previous analyses the NC energy estimator was based on linear fits of the average deposited energy, $\langle E_{\text{dep}} \rangle$, as a function of E_{cal} over the range of 0 to 10 GeV for both the ND and FD [44]. A new round of MC simulation has been produced, and so these fits were redone. The linear estimator for the new MC uses the same fitting method as the previous analyses. The results of these fits can be seen in Figure 6.2. Applying the fit parameters, the linear estimator returns an estimate, E_L, for the ND and FD

$$E_{\text{ND,L}} = (0.034 \pm 0.001)\,\text{GeV} + (1.168 \pm 0.001) \times E_{\text{cal}}, \tag{6.2}$$

$$E_{\text{FD,L}} = (0.070 \pm 0.001)\,\text{GeV} + (1.170 \pm 0.001) \times E_{\text{cal}}. \tag{6.3}$$

This estimator treats all events in the same manner and neglects the differences in the hadronic content. Attempting to account for hadronic activity in events with a large fraction of electromagnetic activity leads to an overestimation of E_{dep}. To illustrate this deficiency we consider two samples of events, those dominated by energy from hadronic activity, E_{Had}, and those dominated by energy from electromagnetic activity, E_{EM}.

To determine which events are dominated by either E_{Had} or E_{EM}, we consider which particles the NC interaction produces. In particular, neutrons and pions are a good discriminator of events with high amounts of E_{Had} or E_{EM}. Neutrons are the primary source of hadronic activity we are concerned with, however charged pions,π^+ or π^-, are also sources of E_{Had}. Like neutrons, charged pions are hadrons while, as charged particles, they ionize the scintillator. Thus events with either neutrons or charged pions have significant E_{Had}. Neutral pions, π^0, are also hadrons but they are electromagnetically neutral and so do not directly ionize the scintillator. However, π^0's quickly and predominately decay into a pair of photons, which are easily detectable sources of E_{EM}. The E_{Had} dominated sample is therefore composed of events which produce at least one neutron, π^+, or π^- and no π^0s, while the E_{EM} dominated sample is composed of events with at least one π^0 and no neutrons, π^+, or π^-. This selection uses the truth information of particles generated in these events. By scaling E_{cal} for both types of events in the same manner, on average the E_{EM} dominated events were overestimated while the E_{Had} dominated events were underestimated, as can be seen in Figure 6.3 which shows $\Delta E_{\text{dep,L}}/E_{\text{dep}}$ for events dominated by E_{EM} or E_{Had}.

6.1.3 Orphaned Energy Estimator

Since the linear estimator overestimates the energy for the E_{EM} dominated sample and underestimates the energy for the E_{Had} dominated sample, one avenue of improvement is to estimate the energy for these samples separately. To do so we would like to split the events based on neutron content; neutrons represent the hadronic activity most likely to be absent in E_{cal}. However, because an energy estimator must be applied to data, any estimation must be done using only reconstructed quantities. As we cannot accurately determine if an event produces neutrons, we cannot use directly

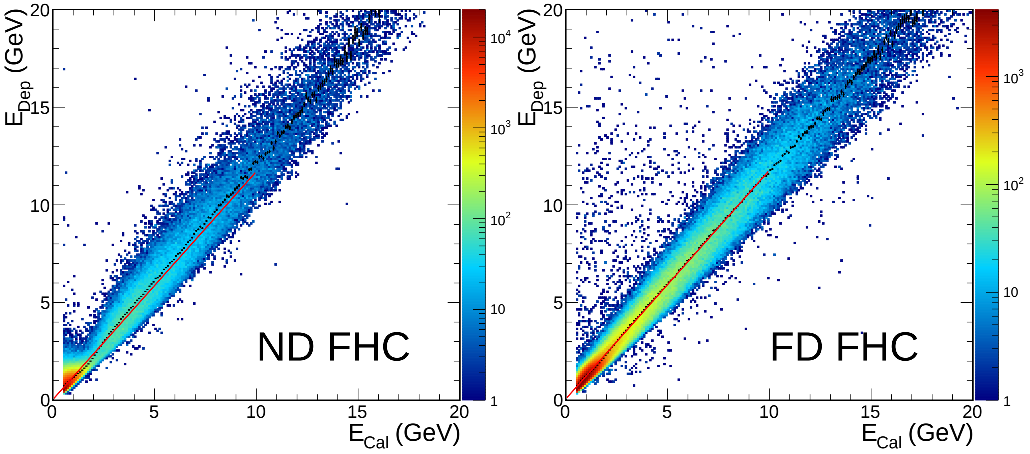

Figure 6.2: Distributions of simulated events showing E_{dep} as a function of E_{cal} for the ND (left) and FD (right). The black points are $\langle E_{dep} \rangle$ for each bin of E_{cal}, and the red lines are the linear fits to these averages. The fits are performed over the range of 0 to 10 GeV. The fit in the ND is $\langle E_{dep} \rangle_{ND} = (0.034 \pm 0.001)\,\text{GeV} + (1.168 \pm 0.001) \times E_{cal}$, and the fit in the FD is $\langle E_{dep} \rangle_{FD} = (0.070 \pm 0.001)\,\text{GeV} + (1.170 \pm 0.001) \times E_{cal}$.

use neutron content as an input to our energy estimator.

Instead, we use the fact that neutrons are not easily reconstructed to our advantage. During the reconstruction of a neutrino event, we associate energy depositions into collections called prongs which represent individual particles. Charged particles easily ionize the scintillator while neutrons do not. This means that charged particles are easy to reconstruct into prongs while neutrons are not. Because of this difficulty, events with calorimetric energy that is not reconstructed into prongs are more likely to have neutrons in the final state than events for which all deposited energy is reconstructed into prongs. We call the energy from depositions which

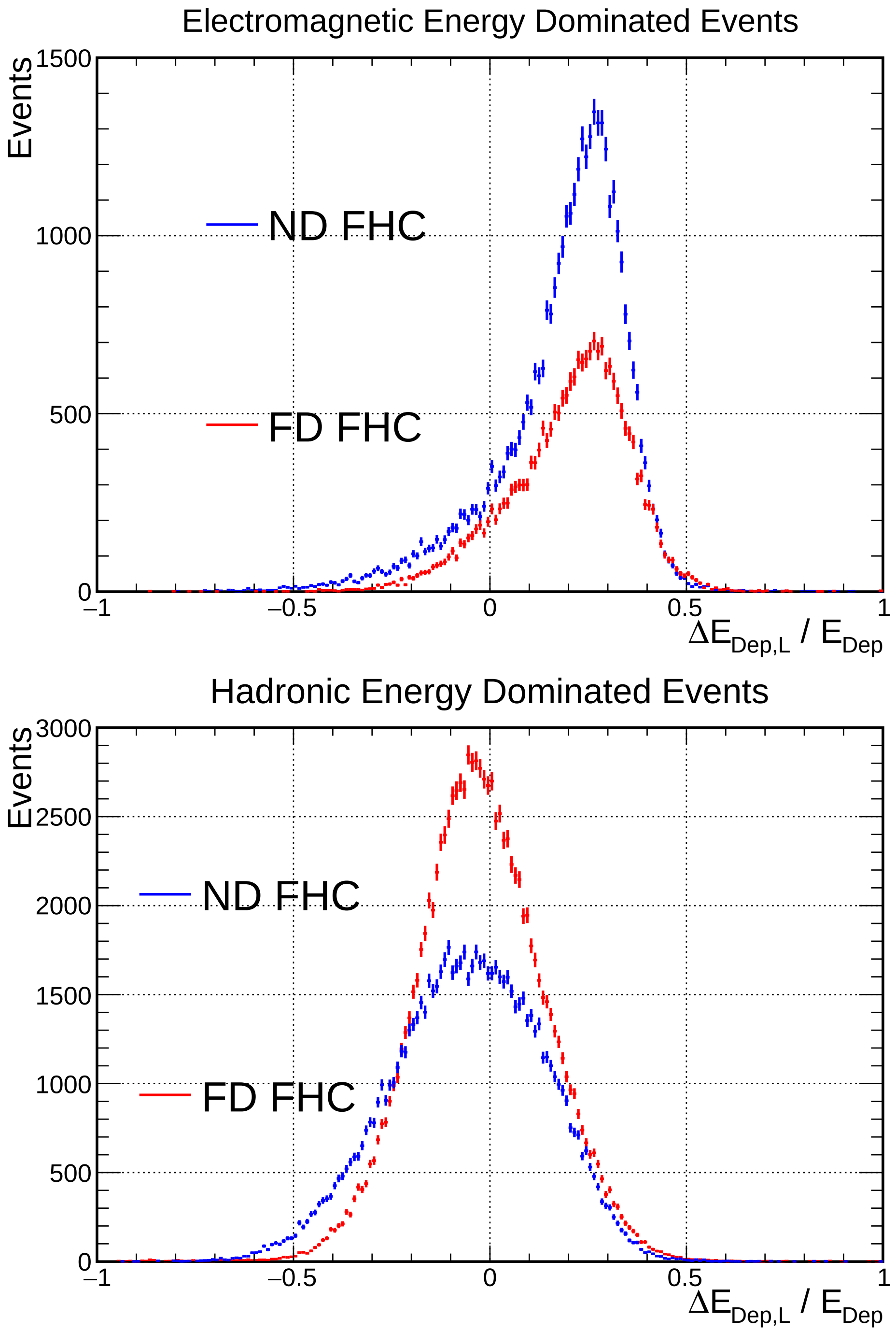

Figure 6.3: Distributions of $\Delta E_{\mathrm{dep,L}}/E_{\mathrm{dep}}$ for the ND and FD events dominated by electromagnetic energy (top) and events dominated by hadronic energy (bottom).

are not in any reconstructed prong the orphaned energy, E_{Orph}. Figure 6.4 shows that splitting the sample at $E_{\text{Orph}} = 0.01\,\text{GeV}$ is a proxy for splitting events by neutron content.

For the orphaned energy estimator, we fit $\langle E_{\text{dep}} \rangle$ as a linear function of E_{cal} for each E_{Orph} sample separately. For the $E_{\text{Orph}} < 0.01\,\text{GeV}$ sample the fit is performed from 0 to 2 GeV, while the $E_{\text{Orph}} > 0.01\,\text{GeV}$ sample is fit from 0 to 10 GeV. These ranges were chosen so that the fit is performed on regions which contain more than 90% of events in the sample. The fits are shown in Figures 6.5 and 6.6. The orphaned energy estimator, E_{O}, is then formed in the same way as in the linear estimator,

$$E_{\text{ND,O}} = \begin{cases} (0.211 \pm 0.002)\,\text{GeV} + (0.905 \pm 0.002) \times E_{\text{cal}}, & E_{\text{Orph}} < 0.01\,\text{GeV}, \\ (0.062 \pm 0.001)\,\text{GeV} + (1.189 \pm 0.001) \times E_{\text{cal}} & E_{\text{Orph}} > 0.01\,\text{GeV}, \end{cases} \tag{6.4}$$

$$E_{\text{FD,O}} = \begin{cases} (0.205 \pm 0.004)\,\text{GeV} + (0.971 \pm 0.004) \times E_{\text{cal}}, & E_{\text{Orph}} < 0.01\,\text{GeV}, \\ (0.100 \pm 0.001)\,\text{GeV} + (1.167 \pm 0.001) \times E_{\text{cal}} & E_{\text{Orph}} > 0.01\,\text{GeV}. \end{cases} \tag{6.5}$$

While the orphaned energy estimator does better than the linear estimator at accounting for E_{EM} and E_{Had}, it does not do so perfectly. This behavior can be seen best in ND events with $E_{\text{cal}} < 2\,\text{GeV}$, where 90% of the electromagnetic energy dominated ND events are located. In Figure 6.7, we can see that the linear estimator leads to a distribution neither sharply peaked

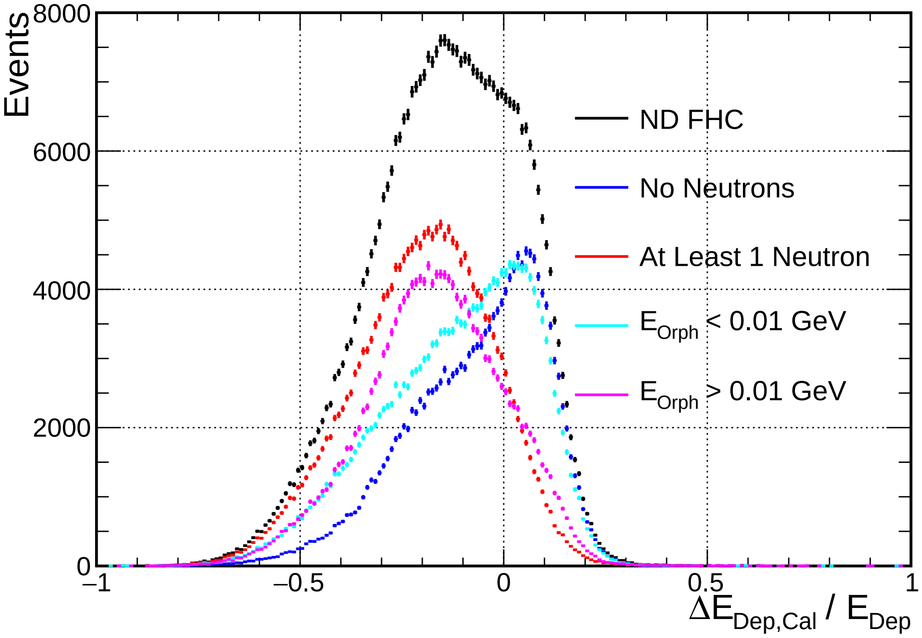

Figure 6.4: The distribution of of the $\Delta E_{\text{dep,cal}}/E_{\text{dep}}$ in the ND. The sample is split into events which produce at least one neutron in the final state (red) and those which have none (blue). Also shown is the split into events with $E_{\text{Orph}} < 0.01$ GeV (cyan) and events with $E_{\text{Orph}} > 0.01$ GeV (magenta).

nor symmetrically distributed around zero. While the orphaned energy estimator leads to a more sharply peaked distribution, it is not symmetric about zero. The reason for this deficiency is two fold: firstly, $\langle E_{\text{dep}} \rangle$ is not linearly distributed in E_{cal} for ND events, as can be seen in Figures 6.2 and 6.5; and secondly, events which have neutrons can still contain electromagnetic showers and the energy from these showers can still be overestimated. To correct this deficiency, we need an estimator which estimates energy from hadronic and electromagnetic showers both separately and non-linearly.

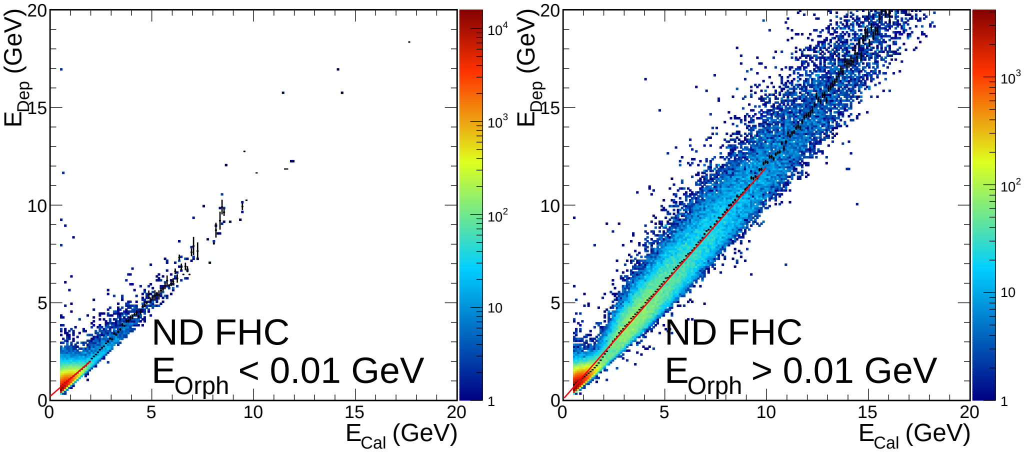

Figure 6.5: Distributions of simulated ND events with $E_{Orph} < 0.01$ GeV (left) and $E_{Orph} > 0.01$ GeV (right). The black points are $\langle E_{dep} \rangle$ vs E_{cal}, and the red lines are the linear fits to these averages, with a fit range of 0 to 2 GeV for $E_{Orph} < 0.01$ GeV and a fit range of 0 to 10 GeV for $E_{Orph} > 0.01$ GeV. The fit is $\langle E_{dep} \rangle = (0.211 \pm 0.002)\,\text{GeV} + (0.905 \pm 0.002) \times E_{cal}$ for $E_{Orph} < 0.01$ GeV, and $\langle E_{dep} \rangle = (0.062 \pm 0.001)\,\text{GeV} + (1.189 \pm 0.001) \times E_{cal}$ for $E_{Orph} > 0.01$ GeV.

6.1.4 Quadratic Estimator

The quadratic energy estimator splits calorimetric energy into two parts, E^r_{EM} and E^r_{Had}, which are the reconstructed calorimetric energy that is respectively electromagnetic or hadronic in origin. A Convolutional Neural Network (CNN) determines which prongs in an event are electromagnetic in origin. The total energy from all electromagnetic prongs is E^r_{EM}, while $E^r_{Had} = E_{cal} - E^r_{EM}$ [45]. The quadratic energy estimator is inspired by the electron neutrino charged current (ν_e CC) energy estimator. Details of the ν_e CC energy estimator can be found in [45]. For that estimator, $\langle E_{dep} \rangle$ was

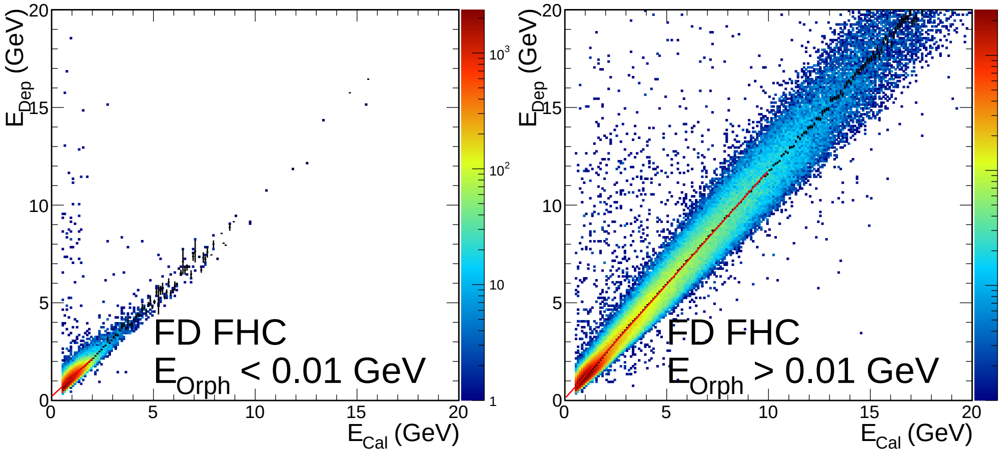

Figure 6.6: Distributions of simulated FD events with $E_{Orph} < 0.01$ GeV (left) and $E_{Orph} > 0.01$ GeV (right). The black points are $\langle E_{dep} \rangle$ vs E_{cal}, and the red lines are the linear fits to these averages, with a fit range of 0 to 2 GeV for $E_{Orph} < 0.01$ GeV and a fit range of 0 to 10 GeV for $E_{Orph} > 0.01$ GeV. The fit is $\langle E_{dep} \rangle = (0.205 \pm 0.004)\,\text{GeV} + (0.971 \pm 0.004) \times E_{cal}$ for $E_{Orph} < 0.01$ GeV, and $\langle E_{dep} \rangle = (0.100 \pm 0.001)\,\text{GeV} + (1.167 \pm 0.001) \times E_{cal}$ for $E_{Orph} > 0.01$ GeV.

fit with the function

$$\langle E_{dep} \rangle = \frac{1}{F}\left(A \times E^{r}_{EM} + B \times E^{r}_{Had} + C \times E^{r2}_{EM} + D \times E^{r2}_{Had}\right). \tag{6.6}$$

However, for this analysis the overall scaling factor F is dropped and we add a cross term. We fit $\langle E_{dep} \rangle$ to the function

$$\langle E_{dep} \rangle = \alpha \times E^{r}_{EM} + \beta \times E^{r}_{Had} + \gamma \times E^{r2}_{EM} + \delta \times E^{r2}_{Had} + \epsilon \times E^{r}_{EM} \times E^{r}_{Had}. \tag{6.7}$$

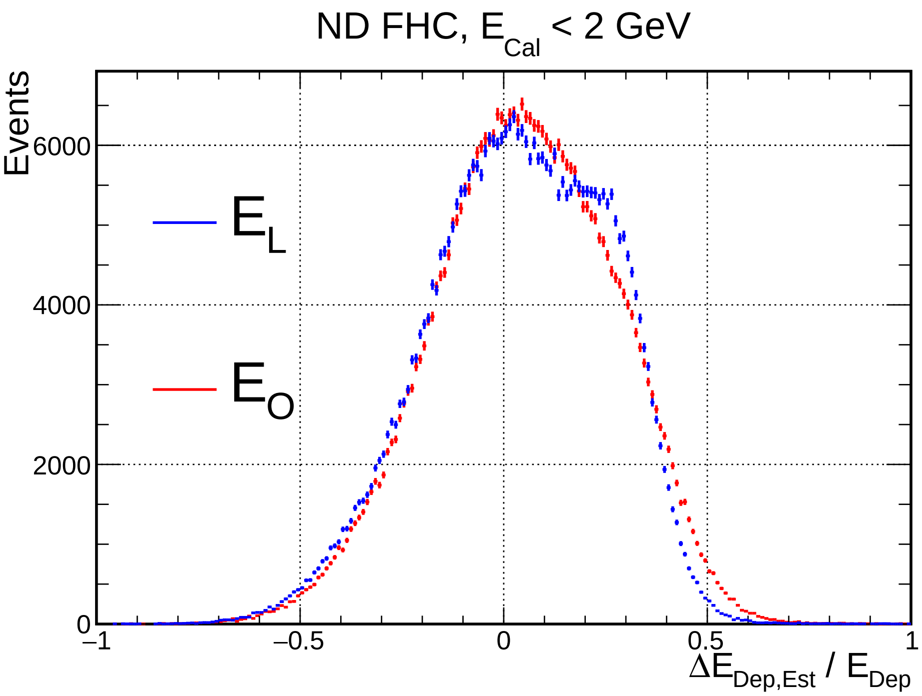

Figure 6.7: Distribution of $\Delta E_{dep,Est}/E_{dep}$, where E_{Est} is either E_L or E_O, for ND events with $E_{cal} < 2$ GeV using the linear estimator (blue) and the orphaned energy estimator (red).

The quadratic energy estimator calculates E_Q,

$$E_Q = \alpha \times E^r_{EM} + \beta \times E^r_{Had} + \gamma \times E^{r2}_{EM} + \delta \times E^{r2}_{Had} + \epsilon \times E^r_{EM} \times E^r_{Had}, \quad (6.8)$$

where the parameters α, β, γ, δ, and ϵ take the values from the fit described in equation (6.7). The distributions of $\langle E_{Dep} \rangle$ in E^r_{EM} and E^r_{Had} can be seen in Figure 6.8. However, the simulation does not cover the entire range of E^r_{EM} and E^r_{Had} with sufficient statistics to be fit well. Only E^r_{EM} and E^r_{Had} bins which have at least 20 events are used in the fit of $\langle E_{dep} \rangle$. The location of these bins can be seen in Figure 6.9. The results of the fit yield

$$\begin{aligned}
E_{\mathrm{ND,Q}} = {} & (1.041 \pm 0.001) \times E^{r}_{\mathrm{EM}} + (1.187 \pm 0.001) \times E^{r}_{\mathrm{Had}} \\
& + (8.1 \pm 0.3) \times 10^{-3} \times \ \mathrm{GeV}^{-1} \times E^{r2}_{\mathrm{EM}} + (2.78 \pm 0.08) \times 10^{-2} \times \ \mathrm{GeV}^{-1} \times E^{r2}_{\mathrm{Had}} \\
& + (0.108 \pm 0.02) \times \ \mathrm{GeV}^{-1} \times E^{r}_{\mathrm{EM}} \times E^{r}_{\mathrm{Had}}, \qquad (6.9) \\
E_{\mathrm{FD,Q}} = {} & (1.035 \pm 0.001) \times E^{r}_{\mathrm{EM}} + (1.259 \pm 0.001) \times E^{r}_{\mathrm{Had}} \\
& + (4.2 \pm 0.3) \times 10^{-3} \times \ \mathrm{GeV}^{-1} \times E^{r2}_{\mathrm{EM}} + (4 \pm 6) \times 10^{-4} \times \ \mathrm{GeV}^{-1} \times E^{r2}_{\mathrm{Had}} \\
& + (5.67 \pm 0.001) \times 10^{-2} \times \ \mathrm{GeV}^{-1} \times E^{r}_{\mathrm{EM}} \times E^{r}_{\mathrm{Had}}. \qquad (6.10)
\end{aligned}$$

However, the quadratic estimator does not perform well for high energy events. As can be seen in Figure 6.9, only the low energy region has sufficient statistics to be used in the quadratic fit, which means the fit does not have the information necessary to make accurate estimations of E_{dep} at higher values of E_{cal}. To improve on this deficiency, an estimator must be developed based on events at all energy scales.

6.1.5 Scaling Estimator

The scaling estimator is developed by looking at $\Delta E_{\mathrm{dep,cal}}/E_{\mathrm{dep}}$ for events dominated by hadronic showers and events dominated by electromagnetic showers. These samples are defined in the same manner as in Section 6.1.2. These distributions, seen in Figure 6.10, are peaked at different values of $\Delta E_{\mathrm{dep,cal}}/E_{\mathrm{dep}}$. Fitting the the region where these distributions are above

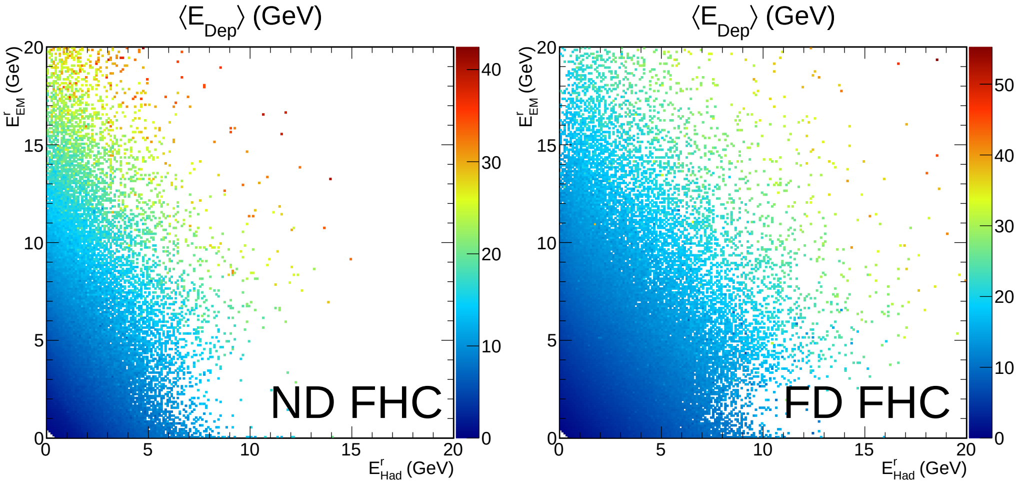

Figure 6.8: Distribution of $\langle E_{dep} \rangle$ (on the color scale) as a function of E^r_{EM} and E^r_{Had} for the ND (left) and FD (right).

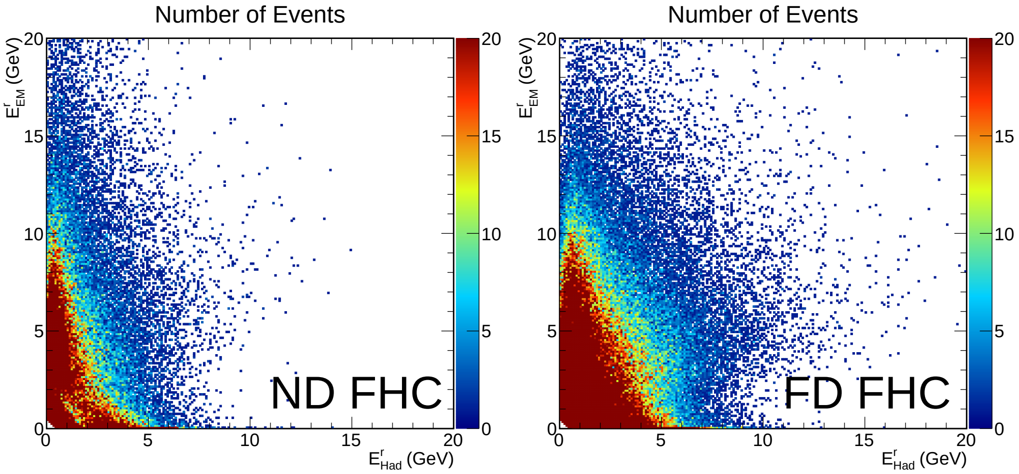

Figure 6.9: Distributions of the number of events (on the color scale) for the ND (left) and FD (right). The color axis is capped at 20 events so that dark red bins have at least 20 events. The fit of $\langle E_{dep} \rangle$ vs E^r_{EM} and E^r_{Had} is done only for bins with at least 20 events.

75% of the maximum value with Gaussian distributions indicates that E_{cal} overestimates E_{dep} for events dominated by electromagnetic showers by 4.9% (2.5%) and underestimates E_{dep} for events dominated by hadronic showers by 20.5% (20.3%) in the ND (FD). If E_{cal} for a single event differs from the event's E_{dep} by X%, then $E_{\text{cal}} = (1 + X/100) \times E_{\text{dep}}$. This relation relies on truth information, so we must use the simulation to find an average difference $\langle X\% \rangle$ for all events. If a sample is found on average to have E_{cal} differ from E_{dep} by $\langle X\% \rangle$, we divide E_{cal} by $1+\langle X\% \rangle /100$ to obtain an estimate of E_{dep}. Using these biases, E_S is obtained by scaling E^r_{EM} and E^r_{Had} as

$$E_{\text{ND,S}} = \frac{E^r_{\text{EM}}}{1.049 \pm 0.003} + \frac{E^r_{\text{Had}}}{0.795 \pm 0.002}, \tag{6.11}$$

$$E_{\text{FD,S}} = \frac{E^r_{\text{EM}}}{1.025 \pm 0.003} + \frac{E^r_{\text{Had}}}{0.797 \pm 0.001}. \tag{6.12}$$

However, this estimator overestimates the energy of events with $E_{\text{cal}} > 2.5$ GeV as seen in Figure 6.11. By fitting a Gaussian distribution to the region above 90% of the maximum value of the $\Delta E_{\text{dep,S}}/E_{\text{dep}}$ distribution, we and see that the scaling estimator overestimate ND events with $E_{\text{cal}} < 2.5$ GeV by 4.5%.

6.1.6 Bias Corrected Estimators

All the energy estimators considered above are biased across E_{cal}, and so we attempt to correct for this deficiency. However, before we correct for this effect, we must first quantify it. The events are separated into samples with

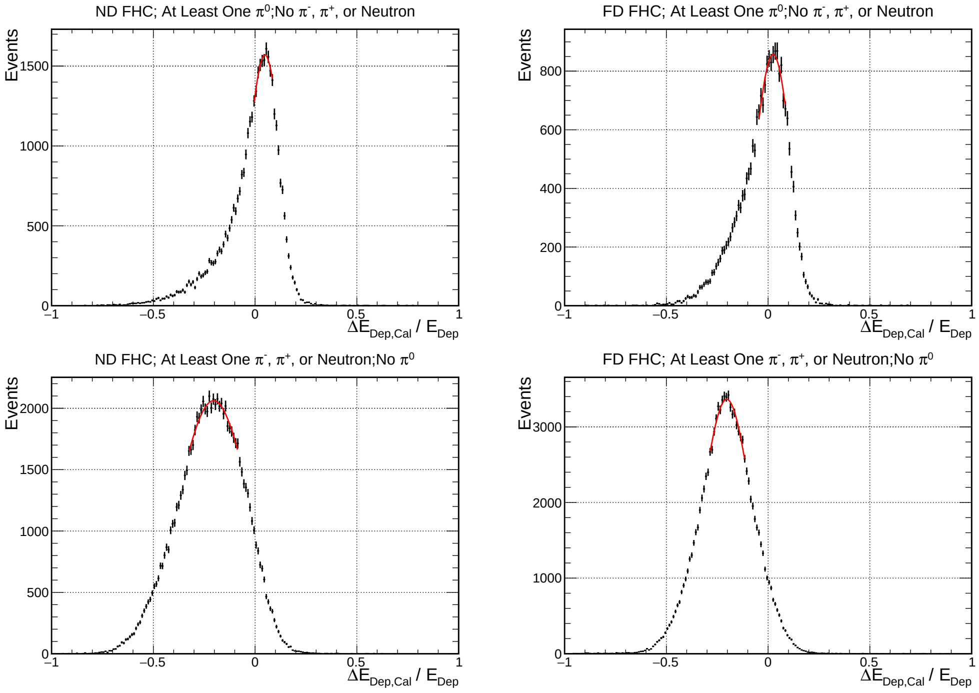

Figure 6.10: Distributions of $\Delta E_{\text{dep,cal}}/E_{\text{dep}}$ for electromagnetic energy dominated events (top row) and hadronic energy dominated events (bottom row), for the ND (left column) and FD (right column). In red are Gaussian fits to the region above 75% of the maximum value. The means from the Gaussian fits are used to obtain correction factors to scale E^r_{EM} and E^r_{Had} to better match the deposited energy. The results of the fit indicate that electromagnetic energy dominated events tend to be overestimated by $(4.9 \pm 0.3)\%$ in the ND and $(2.5 \pm 0.3)\%$ in the FD, while the hadronic energy dominated events are underestimated by $(20.5 \pm 0.2)\%$ and $(20.3 \pm 0.1)\%$ in the ND and FD respectively.

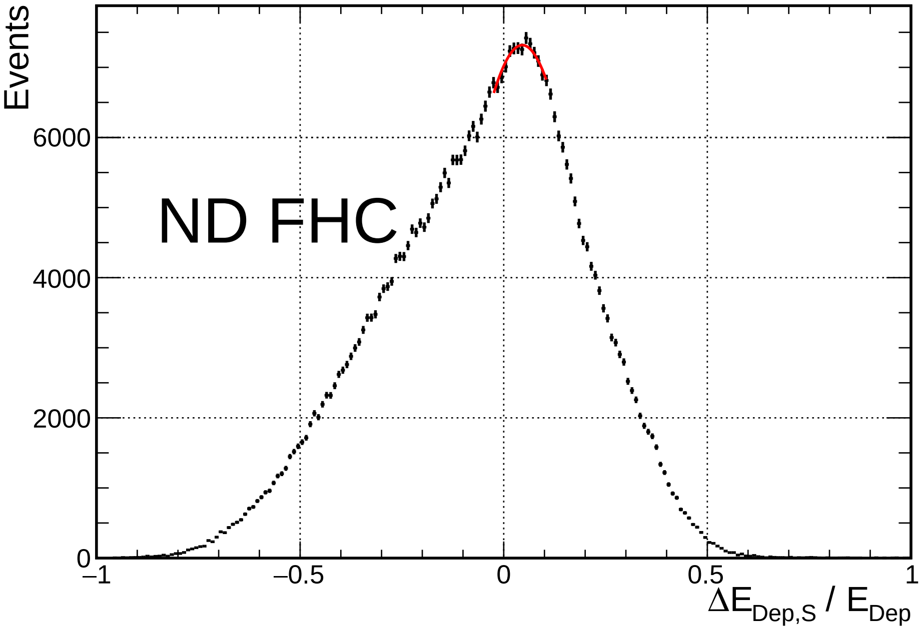

Figure 6.11: The distribution of $\Delta E_{dep,S}/E_{dep}$ for ND events with $E_{cal} < 2.5$ GeV. In red is the Gaussian fit to the distribution in the region above 90% of the maximum value of the distribution. The mean from this Gaussian fit is 4.5%.

$0.5\,\text{GeV} \leqslant E_{cal} \leqslant 1\,\text{GeV}$, $1\,\text{GeV} \leqslant E_{cal} \leqslant 1.5\,\text{GeV}$, and so on up to 40 GeV. The distribution of $\Delta E_{dep,Est}/E_{dep}$ is obtained for each sample, and these $\Delta E_{dep,Est}/E_{dep}$ distributions are fit with a Gaussian distribution. The mean from the Gaussian fit is the bias for that E_{cal} range, with the uncertainty in the bias taken as the uncertainty in the fit mean. However, not every sample is truly Gaussian, and so different ranges of $\Delta E_{dep,Est}/E_{dep}$ are used depending on the number of events in the E_{cal} sample. If the number of events is greater than 50000, only the bins in the sample with content above

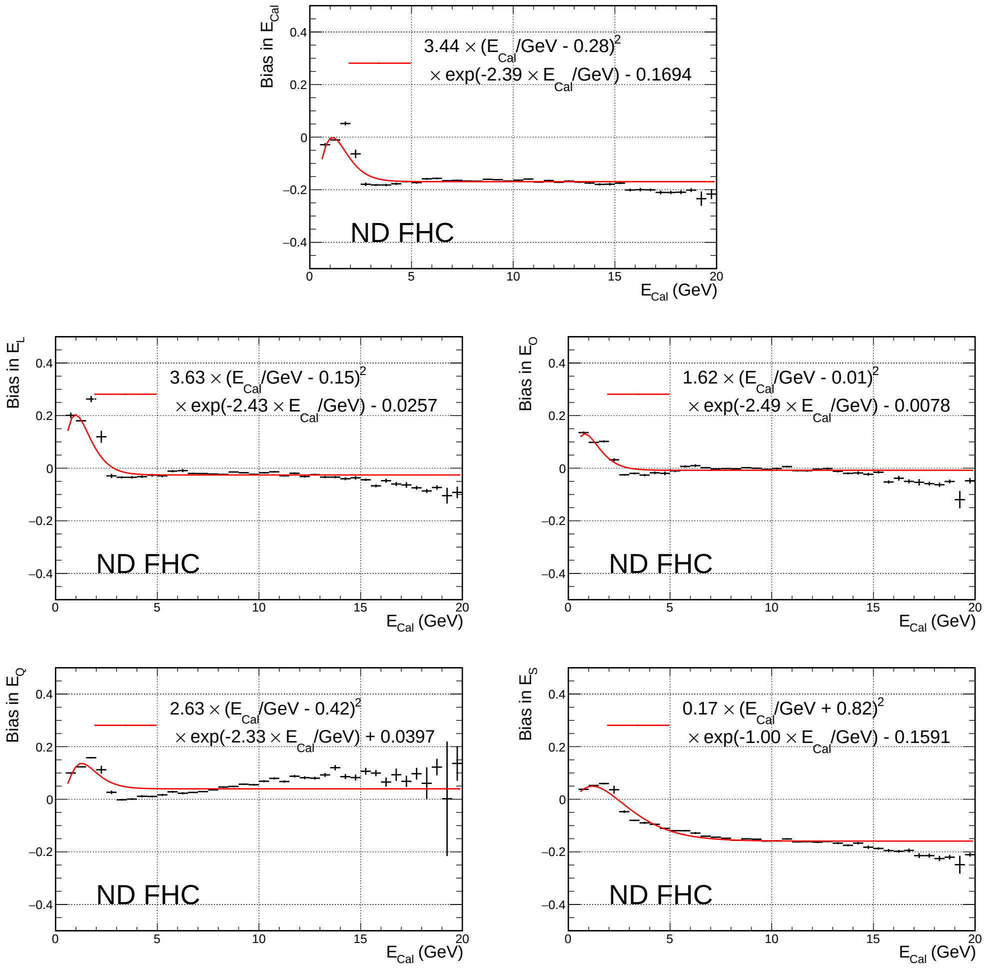

Figure 6.12: The biases in E_{cal} (top), E_L(middle left), E_O (middle right), E_Q (bottom left), and E_S (bottom right) for ND events. In red are the best fits of the biases to the function defined in equation (6.13).

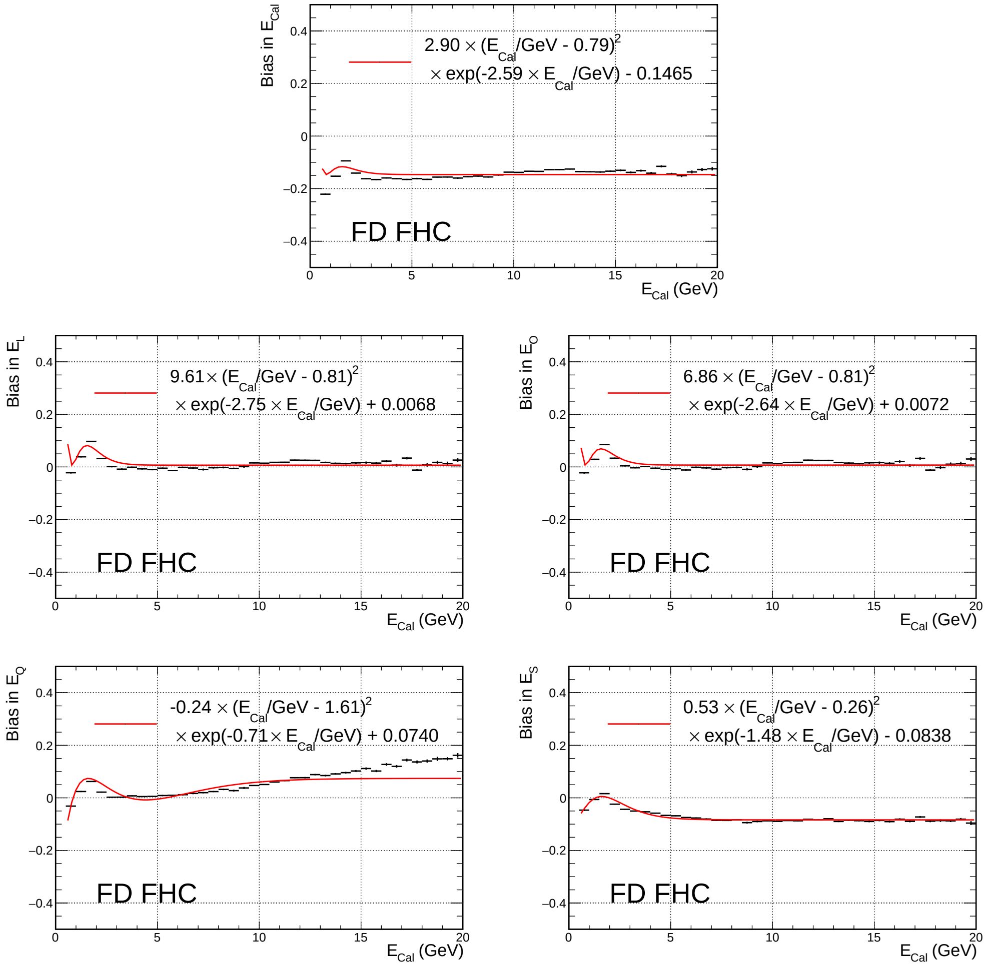

Figure 6.13: The biases in E_{cal} (top), E_L(middle left), E_O (middle right), E_Q (bottom left), and E_S (bottom right) for FD events. In red are the best fits of the biases to the function defined in equation (6.13).

80% of the maximum bin content are fit; if the number of events is between 3200 and 50000, the bins in the sample above 50% of the maximum value is fit; and if the number of events is less than 3200 then the entire region is fit. By changing the range of the fits based on the statistics of the sample we ensure that each fit identifies the peak of the distribution as accurately as possible. Figure 6.14 shows the bias in E_{Est} as a function of E_{cal} for the calorimetic, linear, orphaned energy, quadratic, and scaling estimators.

To correct these biases, we fit them as a function of E_{cal} with the product of a parabola and an exponential

$$f_{Est}(E_{cal}) = P \times (E_{cal}/\text{GeV} + Q)^2 \times e^{-R \times E_{cal}} + S \tag{6.13}$$

This *ad hoc* function was chosen as it captures the shape at low energies while becoming asymptotically flat at high energies. The asymptote ensures the correction will not change rapidly at high energies. The fits can be seen in Figures 6.12 and 6.13. The best fit functions for the ND are

$$f_{ND,cal}(E_{cal}) = 3.44 \times (E_{cal}/\text{GeV} - 0.28)^2 \times e^{-2.39 \times E_{cal}/\text{GeV}} - 0.1694, \tag{6.14a}$$

$$f_{ND,L}(E_{cal}) = 3.63 \times (E_{cal}/\text{GeV} - 0.15)^2 \times e^{-2.43 \times E_{cal}/\text{GeV}} - 0.0257, \tag{6.14b}$$

$$f_{ND,O}(E_{cal}) = 1.62 \times (E_{cal}/\text{GeV} - 0.01)^2 \times e^{-2.49 \times E_{cal}/\text{GeV}} - 0.0078, \tag{6.14c}$$

$$f_{ND,Q}(E_{cal}) = 2.63 \times (E_{cal}/\text{GeV} - 0.42)^2 \times e^{-2.33 \times E_{cal}/\text{GeV}} + 0.0397, \tag{6.14d}$$

$$f_{ND,S}(E_{cal}) = 0.17 \times (E_{cal}/\text{GeV} + 0.82)^2 \times e^{-1.00 \times E_{cal}/\text{GeV}} - 0.1591, \tag{6.14e}$$

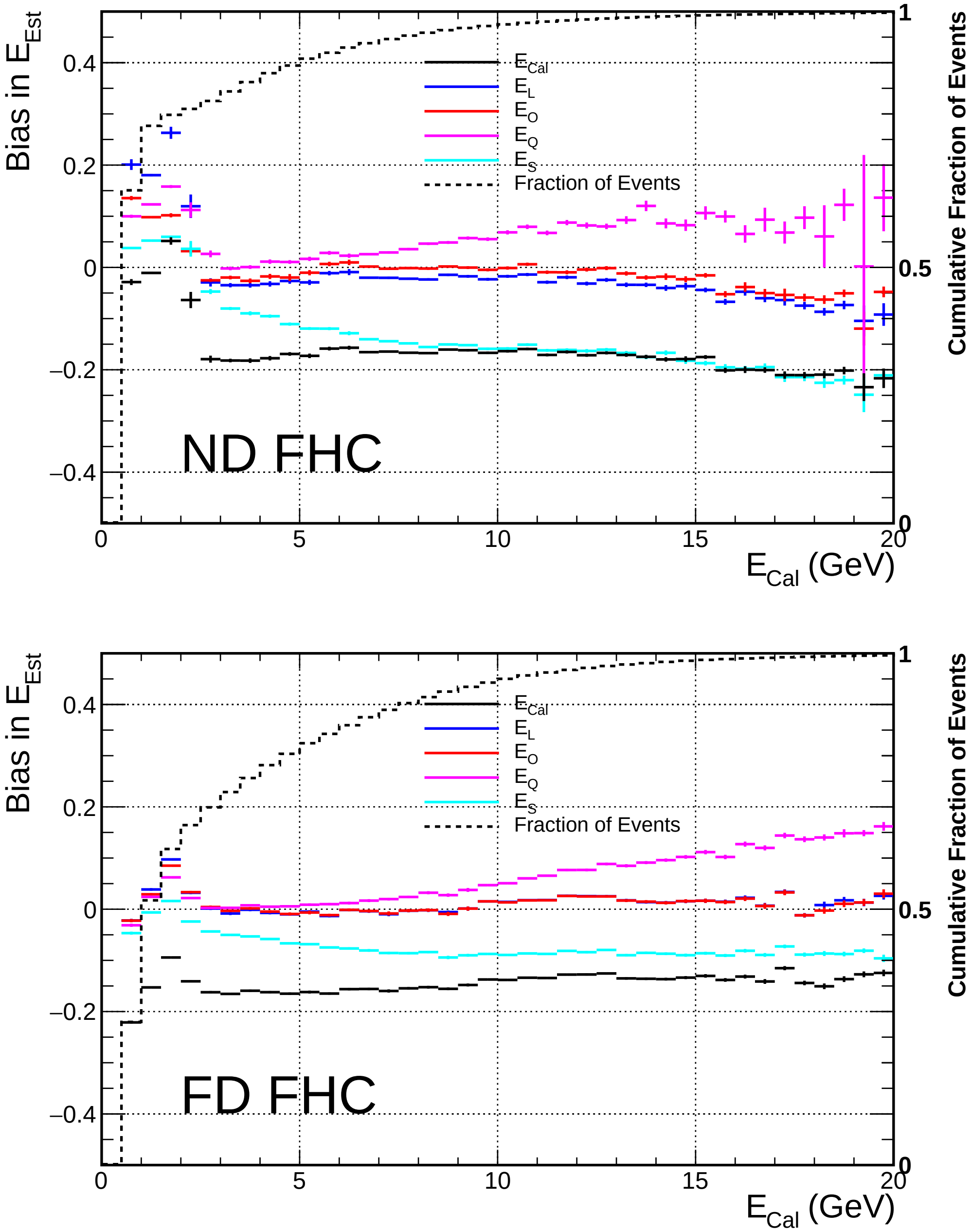

Figure 6.14: The biases in E_{Est} for the calorimetric, linear, orphaned energy, quadratic, and scaling estimators for ND (top) and FD (bottom) events. Also shown is the cumulative fraction of events bellow E_{cal}, shown with the dashed line.

and the best fit functions for the FD are

$$f_{\mathrm{FD,cal}}(E_{\mathrm{cal}}) = \quad 2.90 \times (E_{\mathrm{cal}}/\mathrm{GeV} - 0.79)^2 \times e^{-2.59\times E_{\mathrm{cal}}/\mathrm{GeV}} - 0.1465, \tag{6.15a}$$

$$f_{\mathrm{FD,L}}(E_{\mathrm{cal}}) = \quad 9.61 \times (E_{\mathrm{cal}}/\mathrm{GeV} - 0.81)^2 \times e^{-2.75\times E_{\mathrm{cal}}/\mathrm{GeV}} + 0.0068, \tag{6.15b}$$

$$f_{\mathrm{FD,O}}(E_{\mathrm{cal}}) = \quad 0.86 \times (E_{\mathrm{cal}}/\mathrm{GeV} - 0.81)^2 \times e^{-2.64\times E_{\mathrm{cal}}/\mathrm{GeV}} + 0.0072, \tag{6.15c}$$

$$f_{\mathrm{FD,Q}}(E_{\mathrm{cal}}) = -0.24 \times (E_{\mathrm{cal}}/\mathrm{GeV} - 1.61)^2 \times e^{-0.71\times E_{\mathrm{cal}}/\mathrm{GeV}} + 0.0740, \tag{6.15d}$$

$$f_{\mathrm{FD,S}}(E_{\mathrm{cal}}) = \quad 0.53 \times (E_{\mathrm{cal}}/\mathrm{GeV} - 0.26)^2 \times e^{-1.48\times E_{\mathrm{cal}}/\mathrm{GeV}} - 0.0838. \tag{6.15e}$$

An event with energy E_{cal} can be assumed to differ from E_{dep} by $f(E_{\mathrm{cal}})$. For each energy estimator, we can generate a new energy estimator

$$E_{\mathrm{Est}'} = \frac{E_{\mathrm{Est}}}{1 + f_{\mathrm{Est}}(E_{\mathrm{cal}})}. \tag{6.16}$$

The bias corrected estimators for the ND are

$$E_{\mathrm{ND,cal'}} = \frac{E_{\mathrm{cal}}}{0.8306 + 3.44 \times (E_{\mathrm{cal}}/\mathrm{GeV} - 0.28)^2 \times e^{-2.39 \times E_{\mathrm{cal}}/\mathrm{GeV}}}, \tag{6.17a}$$

$$E_{\mathrm{ND,L'}} = \frac{E_{\mathrm{ND,L}}}{0.9743 + 3.63 \times (E_{\mathrm{cal}}/\mathrm{GeV} - 0.15)^2 \times e^{-2.43 \times E_{\mathrm{cal}}/\mathrm{GeV}}}, \tag{6.17b}$$

$$E_{\mathrm{ND,O'}} = \frac{E_{\mathrm{ND,O}}}{0.9922 + 1.62 \times (E_{\mathrm{cal}}/\mathrm{GeV} - 0.01)^2 \times e^{-2.49 \times E_{\mathrm{cal}}/\mathrm{GeV}}}, \tag{6.17c}$$

$$E_{\mathrm{ND,Q'}} = \frac{E_{\mathrm{ND,Q}}}{1.0397 + 2.63 \times (E_{\mathrm{cal}}/\mathrm{GeV} - 0.42)^2 \times e^{-2.33 \times E_{\mathrm{cal}}/\mathrm{GeV}}}, \tag{6.17d}$$

$$E_{\mathrm{ND,S'}} = \frac{E_{\mathrm{ND,S}}}{0.8409 + 0.17 \times (E_{\mathrm{cal}}/\mathrm{GeV} + 0.82)^2 \times e^{-1.00 \times E_{\mathrm{cal}}/\mathrm{GeV}}}. \tag{6.17e}$$

Where $E_{\mathrm{ND,L}}$, $E_{\mathrm{ND,O}}$, $E_{\mathrm{ND,Q}}$, and $E_{\mathrm{ND,S}}$ are defined in equations (6.2), (6.4), (6.9), and (6.11) respectively. The bias corrected estimators for the FD are

$$E_{\mathrm{FD,cal'}} = \frac{E_{\mathrm{cal}}}{0.8535 + 2.90 \times (E_{\mathrm{cal}}/\mathrm{GeV} - 0.79)^2 \times e^{-2.59 \times E_{\mathrm{cal}}/\mathrm{GeV}}}, \tag{6.18a}$$

$$E_{\mathrm{FD,L'}} = \frac{E_{\mathrm{FD,L}}}{1.0068 + 9.61 \times (E_{\mathrm{cal}}/\mathrm{GeV} - 0.81)^2 \times e^{-2.75 \times E_{\mathrm{cal}}/\mathrm{GeV}}}, \tag{6.18b}$$

$$E_{\mathrm{FD,O'}} = \frac{E_{\mathrm{FD,O}}}{1.0072 + 6.86 \times (E_{\mathrm{cal}}/\mathrm{GeV} - 0.81)^2 \times e^{-2.64 \times E_{\mathrm{cal}}/\mathrm{GeV}}}, \tag{6.18c}$$

$$E_{\mathrm{FD,Q'}} = \frac{E_{\mathrm{FD,Q}}}{1.0740 - 0.24 \times (E_{\mathrm{cal}}/\mathrm{GeV} - 1.61)^2 \times e^{-0.71 \times E_{\mathrm{cal}}/\mathrm{GeV}}}, \tag{6.18d}$$

$$E_{\mathrm{FD,S'}} = \frac{E_{\mathrm{FD,S}}}{0.9162 + 0.53 \times (E_{\mathrm{cal}}/\mathrm{GeV} - 0.26)^2 \times e^{-1.48 \times E_{\mathrm{cal}}/\mathrm{GeV}}}. \tag{6.18e}$$

Where $E_{\mathrm{FD,L}}$, $E_{\mathrm{FD,O}}$, $E_{\mathrm{FD,Q}}$, and $E_{\mathrm{FD,S}}$ are defined in equations (6.3), (6.5), (6.10), and (6.12) respectively. The bias corrected estimators do not fully remove the biases as the fits in Figures 6.12 and 6.13 do not perfectly follow the biases. The remaining biases in the the corrected estimators can be seen in Figure 6.15. We use these biases to determine which of these estimators to use in the analysis.

6.1.7 Selecting an Estimator

Since more than 50% of all events in both the ND and FD have $E_{\text{cal}} < 2\,\text{GeV}$, it is this region that we should give the most consideration when selecting an energy estimator. As can be seen in figure 6.15, the bias corrected scaling estimator is almost always the least biased energy estimator in the $E_{\text{cal}} < 2\,\text{GeV}$ region. The two exceptions are that the bias corrected linear estimator has a smaller bias for ND events with $1\,\text{GeV} < E_{\text{cal}} < 1.5\,\text{GeV}$ and that the bias corrected quadratic estimator has a smaller bias for FD events with $1.5\,\text{GeV} < E_{\text{cal}} < 2\,\text{GeV}$. In ND events with $1\,\text{GeV} < E_{\text{cal}} < 1.5\,\text{GeV}$ the bias corrected calorimetric estimator has a bias of $-6 \times 10^{-3}\%$ compared the the bias corrected scaling estimator's 0.2%, and in FD events with $1.5\,\text{GeV} < E_{\text{cal}} < 2\,\text{GeV}$ the bias corrected quadratic estimator has a bias of -0.9% compared to the bias corrected scaling estimator's 1.2%. However, the bias corrected calorimetric and quadratic estimators have their own deficiencies. As seen in Figure 6.15 the bias corrected calormetric estimator has a bias of -9% for FD events with $E_{\text{cal}} < 1\,\text{GeV}$ where 28% of the FD events are located, and the bias corrected quadratic estimator has an increasing bias for for $E_{\text{cal}} > 10\,\text{GeV}$.

Additionally we look at the distribution of $\Delta E_{\text{dep,Est}}/E_{\text{dep}}$ for each esti-

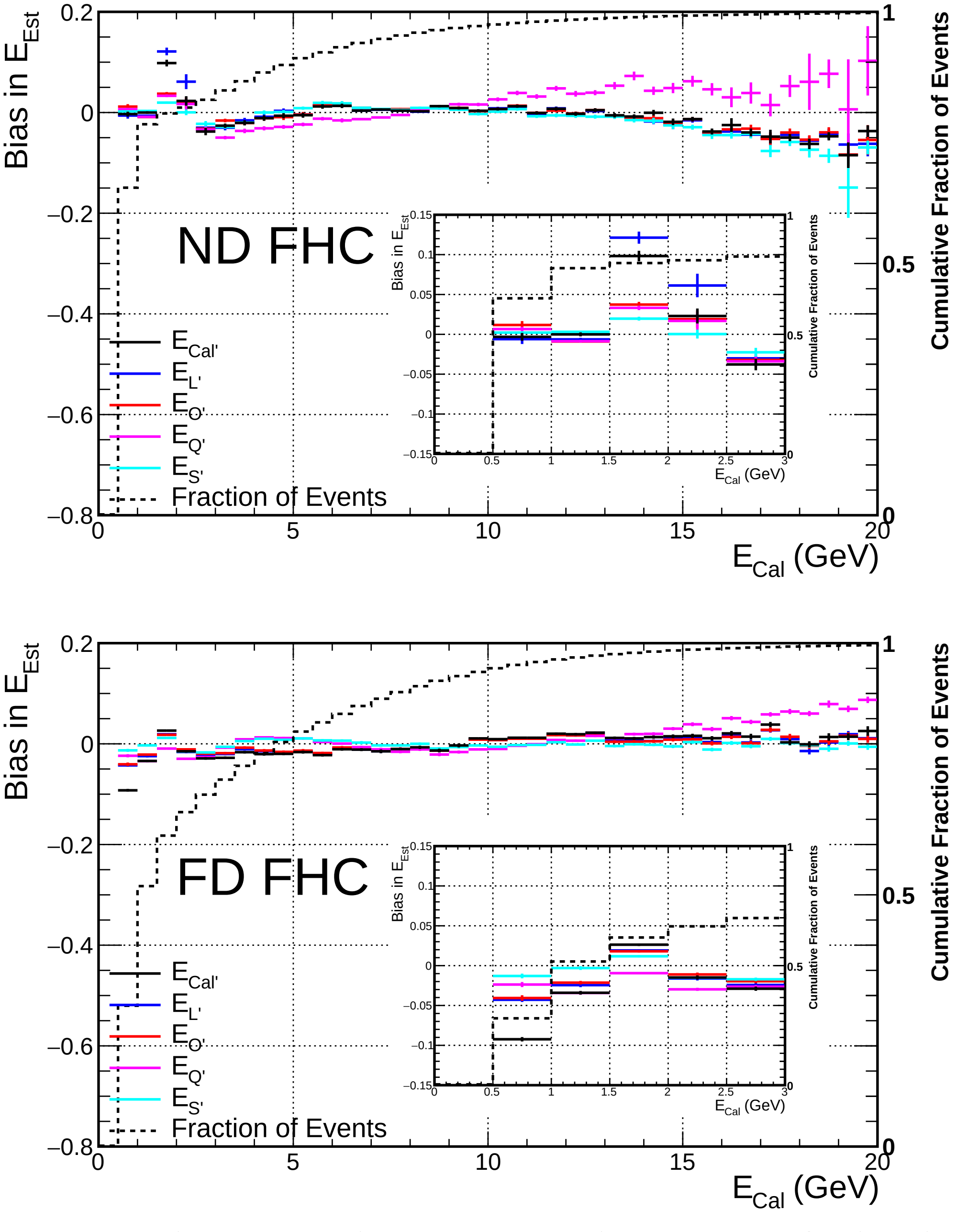

Figure 6.15: The remaining biases in E_{Est} after bias correction for the calorimetric, linear, orphaned energy, quadratic, and scaling estimators for ND (top) and FD (bottom) events. Also shown is the cumulative fraction of events bellow E_{cal}, shown with the dashed line. The inlays show a zoomed in view of the region $E_{cal} < 3\,\text{GeV}$.

mator. These distributions can be seen in Figure 6.16, and show that the bias corrected quadratic and scaling estimators are the most precise of the estimators considered in both detectors. The full widths at half max (FWHM) of the $\Delta E_{\mathrm{dep},Q'}/E_{\mathrm{dep}}$ distributions are 40% and 31% in the ND and FD respectively, while the FWHM of the $\Delta E_{\mathrm{dep},S'}/E_{\mathrm{dep}}$ distributions are 37% and 30% in the ND and FD respectively. Additionally, the bias corrected scaling estimator is has a more symmetric resolution in the ND than the bias corrected quadratic estimator.

As the bias corrected scaling estimator is most accurate and precise estimator by our metric, we select it as the energy estimator for this analysis.

6.2 Summary

We investigated several different methods of estimating the energy deposited by NC events. We found that scaling the electromagnetic and hadronic energy in an event separately had the least bias in the region where most of the NC events exist, $E_{\mathrm{Cal}} < 2\,\mathrm{GeV}$. The electromagnetic and hadronic energy is determined by prong CNN scores, and the scaling factors are found by comparing E_{cal} from simulated electromagnetic and hadronic events to E_{dep}. The estimator is further tuned based on a fit of the biases in E_S as a function of E_{cal}. The final energy estimators for the ND and FD FHC samples from

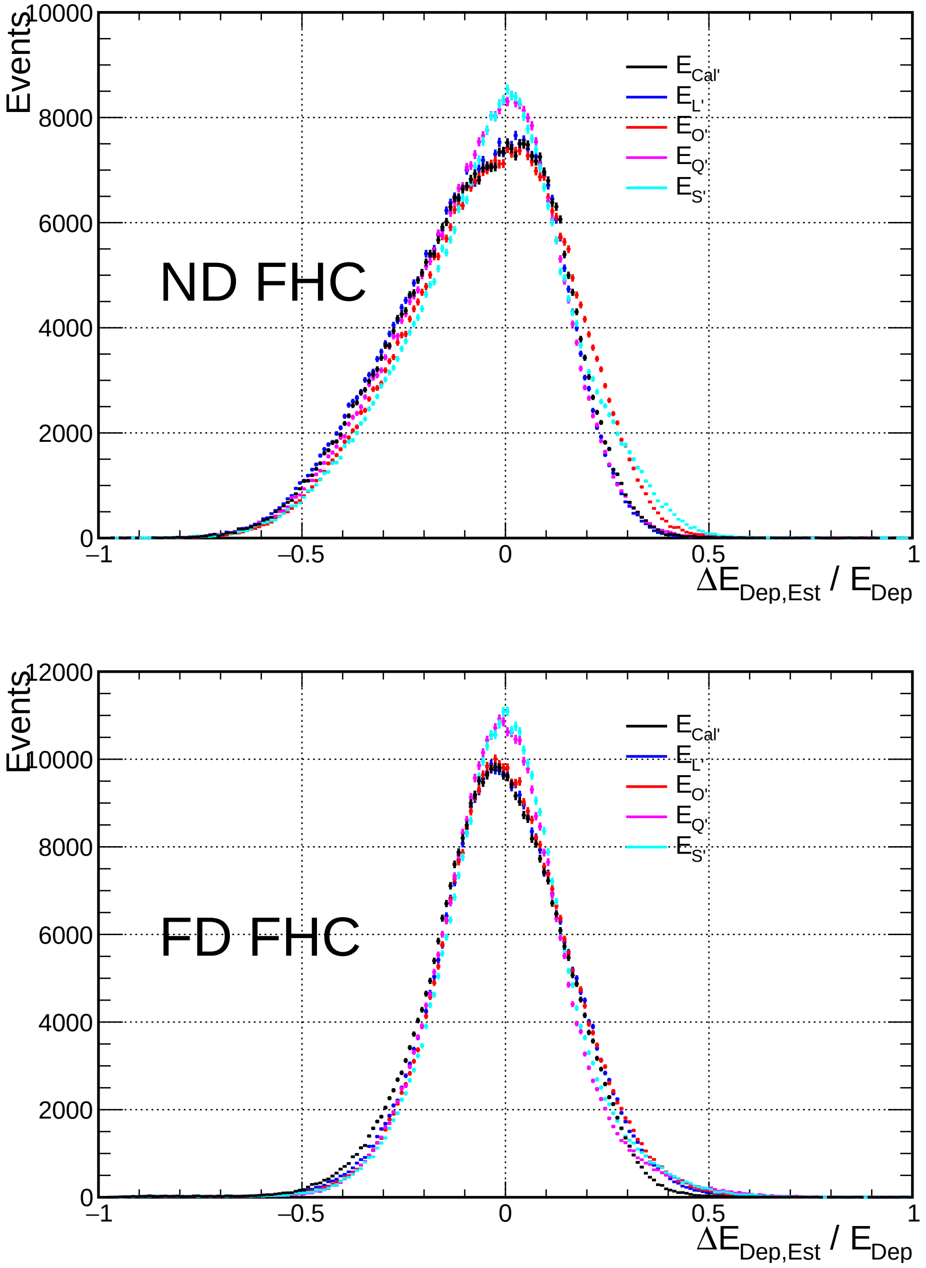

Figure 6.16: Distributions of $\Delta E_{dep,Est}/E_{dep}$ for the bias corrected calorimetric, linear, orphaned energy, quadratic, and scaling estimators for ND (top) and FD (bottom) events.

equations (6.17e) and (6.18e) are

$$E_{\mathrm{ND,FHC}} = \frac{E^{r}_{\mathrm{EM}}/1.049 + E^{r}_{\mathrm{Had}}/0.795}{0.8409 + 0.17 \times (E_{\mathrm{cal}}/\mathrm{GeV} + 0.82)^2 \times e^{-1.00 \times E_{\mathrm{cal}}/\mathrm{GeV}}},$$

$$E_{\mathrm{FD,FHC}} = \frac{E^{r}_{\mathrm{EM}}/1.025 + E^{r}_{\mathrm{Had}}/0.797}{0.9162 + 0.53 \times (E_{\mathrm{cal}}/\mathrm{GeV} - 0.26)^2 \times e^{-1.48 \times E_{\mathrm{cal}}/\mathrm{GeV}}}.$$

Chapter 7

Covariance Matrix Fitting

When we examine the effects of a sterile neutrino state on neutrino oscillations in Equation (2.36) we find a term coming from the squared sine of Δm^2_{41}. When this factor is close to zero then the effect of sterile neutrinos is negligible, while the larger it is the more significant the effect. This fact is useful as it allows us a handy way to check when neutrino oscillations in the ND start to occur. Taking $L = 1\,\mathrm{km}$, which is the distance the ND is from the beam source, and $E = 1.8\,\mathrm{GeV}$, which is the approximate peak energy of our neutrino beam, we can plot this term as a function of Δm^2_{41}. Figure 7.1 shows that for $\Delta m^2_{41} \gtrsim 0.5\,\mathrm{eV}^2/c^4$ that this term is non-negligible and that we must account for oscillations in the ND.

This analysis uses covariance matrix fitting techniques to maximize our sensitivity to sterile neutrinos at higher Δm^2_{41}. Covariance matrices allow us to correlate the systematic uncertainties between every bin in our

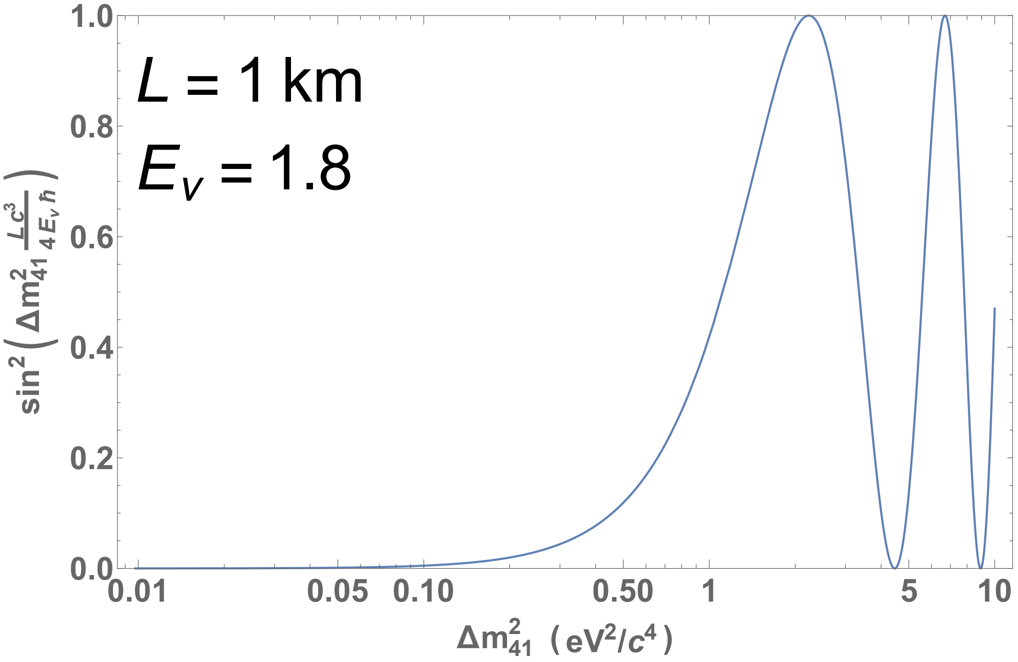

Figure 7.1: The value of $\sin^2\left(\Delta m_{41}^2 \frac{Lc^3}{4E\hbar}\right)$ at the distance of the NOvA ND, $L = 1\,\mathrm{km}$, for the energy peak of the neutrino beam, $E_\nu \approx 1.8\,\mathrm{GeV}$. For $\Delta m_{41}^2 \lesssim 0.5\,\mathrm{eV}^2/c^4$ the term is negligible and we can ignore sterile oscillations in the ND. Larger values of Δm_{41}^2 necessitate accounting for oscillations in the ND.

selected energy spectra, which allows us to use the high statistics in the ND to constrain the systematics in the FD without removing the ND selection from the analysis. Previous NOvA analyses have used a one-detector fit for sterile neutrinos, which inherently limits our sensitivity to the mass-squared splitting Δm_{41}^2 [46].

Previous NOvA analyses used ND measurements to predict the FD spectrum via an extrapolation method [47]. In a detector extrapolation analysis the ND spectra is assumed to be a measurement of the neutrinos before they have propagated far enough to oscillate and so can be used to predict the FD spectra in the presence/absence of sterile neutrino oscillations. This analytic technique is serviceable when we can assume that the ND baseline is short enough that no significant oscillation has occurred. However, as we can see from Figure 7.1, this assumption limits us to values of $\Delta m^2_{41} \lesssim 0.5\,\mathrm{eV}^2/c^4$. To this end we want to use a technique which allows us to use the ND data as part of the analysis while also taking advantage of the similarities between the detectors outlined in Chapter 3. This is precisely what a covariance matrix fit does for us.

7.1 Principals of Covariance

Covariance is the tool which we can leverage to maximize the sensitivity of our two detectors to oscillations due to sterile neutrinos. Suppose we have two variables X and Y which we can measure simultaneously in one experiment to obtain values x_1 and y_1. We may repeat the experiment to obtain measurements x_2, y_2, x_3, y_3, and so on. After N experiments we can calculate mean measurements of the two variables as

$$\bar{x} = \frac{1}{N}\sum_{i}^{N} x_i, \quad \bar{y} = \frac{1}{N}\sum_{i}^{N} y_i \tag{7.1}$$

and the *covariance* between X and Y as

$$\mathrm{Cov}(X, Y) = \frac{1}{N} \sum_{i}^{N} (x_i - \bar{x})(y_i - \bar{y}) \tag{7.2}$$

The basic interpretation of $\mathrm{Cov}(X, Y)$ is as a measurement of how X and Y are expected to vary with respect to eachother. If $\mathrm{Cov}(X, Y) > 0$ we should expect that when a measurement of X fluctuates about its true value that the measurement of Y will fluctuate in the same direction, *i.e.* if $\mathrm{Cov}(X, Y) > 0$ and $x_i > \bar{x}$ we should expect $y_i > \bar{y}$. If $\mathrm{Cov}(X, Y) < 0$ then we expect the fluctuations in x_i and y_i to act in opposite directions. When there is no covariance between two variables, *i.e.* $\mathrm{Cov}(X, Y) = 0$, then a measurement of X gives us no information about the measurement of Y. Examples demonstrating what positive, negative, and near zero covariance look like can be found in Figure 7.2.

Covariance is symmetric, $\mathrm{Cov}(X, Y) = \mathrm{Cov}(Y, X)$, and the covariance of a variable with itself is the variance in that variable

$$\mathrm{Cov}(X, X) = \frac{1}{N} \sum_{i}^{N} (x_i - \bar{x})^2 = \sigma_X^2. \tag{7.3}$$

However, it is important to note that the covariance does not capture the shape of the underlying distribution. For example, suppose the variables X and Y are chosen about the circle $X^2 + Y^2 = 1$ with some experimental uncertainty on the measurement applied. Since $\bar{x}$ and $\bar{y}$ will be near-zero,

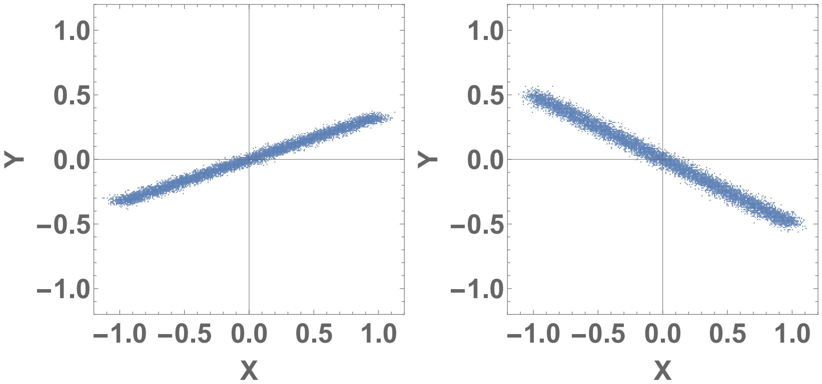

(a) $\text{Cov}(X, Y) = 0.110453$ (b) $\text{Cov}(X, Y) = -0.166053$

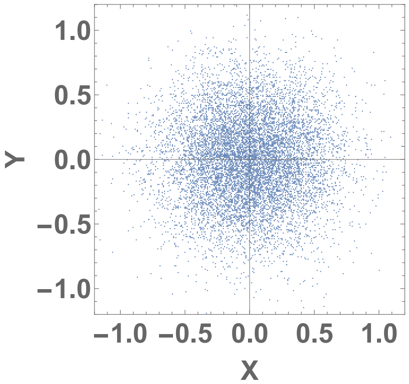

(c) $\text{Cov}(X, Y) = 0.000986901$

Figure 7.2: Example distributions with different values of $\text{Cov}(X, Y)$. Each point shows the values x_i and y_i from a single experiment. Figure 7.2a has $\text{Cov}(X, Y) = 0.110453$, Figure 7.2b has $\text{Cov}(X, Y) = -0.166053$, and Figure 7.2c has $\text{Cov}(X, Y) = 0.000986901$.

for a given x_i, $(y_i - \bar{y})$ is equally likely to be positive or negative. This leads to zero covariance. This situation is illustrated in Figure 7.3. The covariance only tells us if the data tend towards a linear relation. Note that in performing a simple linear regression on X and Y to find α and β such that $Y = \beta X + \alpha$ the ordinary least squares method finds

$$\beta = \frac{\sum_i^N (x_i - \bar{x})(y_i - \bar{y})}{\sum_i^N (x_i - \bar{x})^2} = \frac{\mathrm{Cov}(X, Y)}{\sigma_x^2}. \tag{7.4}$$

From Equation (7.4) we see that $\mathrm{Cov}(X, Y)$ is intrinsically linked to the how steep a linear relation exists between X and Y.

We encode the covariance between multiple variables, $X_1, X_2, \ldots X_M$, in a matrix C whose elements are the covariance between any two variables

$$C_{i,j} = \mathrm{Cov}(X_i, X_j). \tag{7.5}$$

Since the covariance is symmetric the covariance matrix is symmetric, and by Equation (7.3) the diagonal elements of C give us the variance of each variable. Often we want the fractional changes in the variables and so we define a fractional covariance matrix F where we normalize the covariance by the expected values

$$F_{i,j} = \frac{\mathrm{Cov}(X_i, X_j)}{\bar{x}_i \bar{x}_j}. \tag{7.6}$$

The fractional covariance matrix is useful to us because it allows us to determine how the contents of two bins will vary without making assumptions

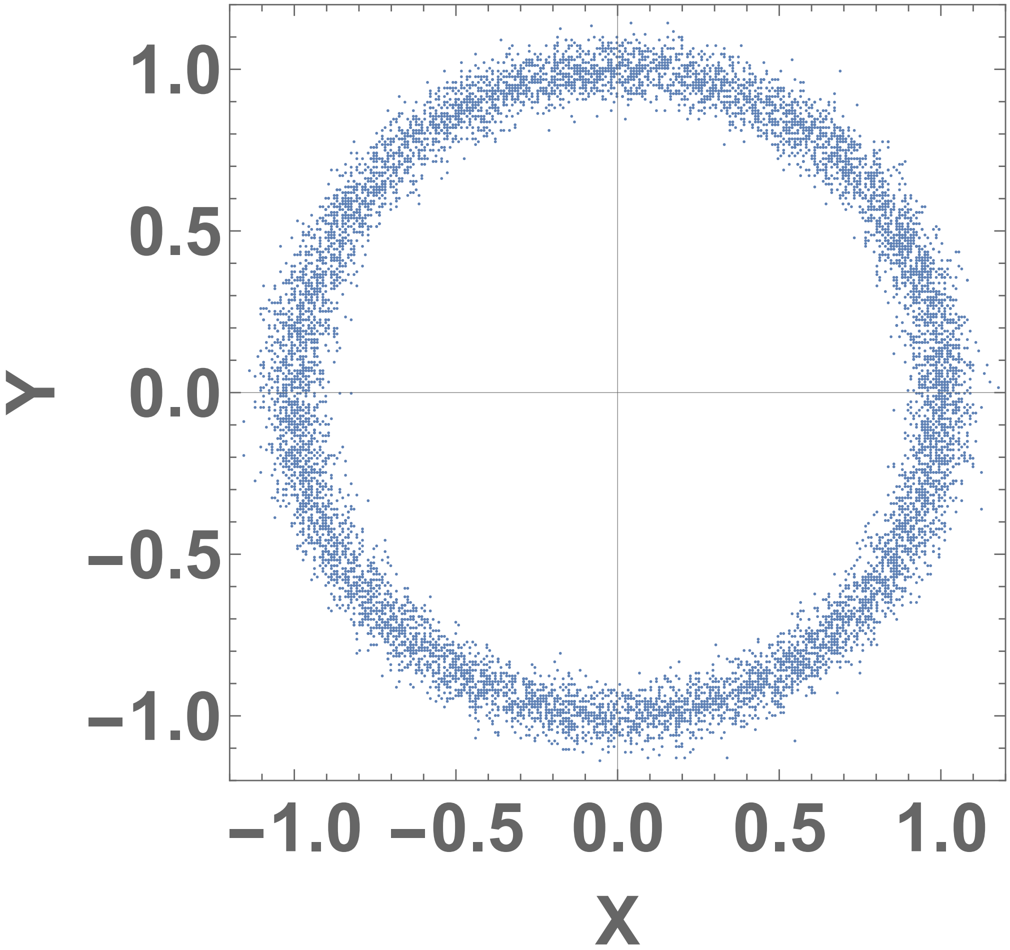

Figure 7.3: An example of data distibuted about the circle $X^2 + Y^2 = 1$. Each point shows the values x_i and y_i from a single experiment. The X and Y variables have no relation and have a covariance of -0.00143745.

on the bin content, the expectation of which depends on the choice of oscillation parameters [48]. Since we wish to use this matrix to compute χ^2 values for the data we do not want to make a priori assumptions on the spectra.

The covariance matrices are also useful since they can be generated for different systematic shifts separately and combined into a single matrix. So long as the systematic uncertainties are independent of each other we have

$$C_{\text{Total}} = C_1 + C_2 + C_3 + \cdots \,, \tag{7.7}$$

where C_i are the covariance matrices generated from independent systematic uncertainties. This property allows us to easily incorporate additional systematic uncertainties since we need only generate the covariance matrix for the new systematic uncertainties and add it to the previous total matrix. In total we consider 93 systematic parameters, each with their own covariance matrix. These systematic parameters encode the effects of our uncertainty in the POT normalization for both the ND and FD, the various components of the neutrino cross section, the effectiveness in the calibration, composition of the NuMI beam flux, and so forth [49].

7.2 Covariance Matrix Generation

To generate the covariance matrix for some systematic uncertainty we generate 2000 pseudo-experiments where the systematic uncertainty parameter is allowed to vary randomly within expected ranges [48].

The ν_μCC events are binned by reconstructed neutrino energy using the same schema as the three flavor analysis with the exception that we do not use the quality quantile binning [50]. The NC events are binned in reconstructed deposited energy E_{dep} with 14 bins from $0.5\,\text{GeV} < E_{\text{dep}} < 20\,\text{GeV}$ evenly spaced in $\log(E_{\text{dep}})$. The NC binning is identical in both the ND and FD.

To ease the creation of our matrices we present our spectra in what is called a logical binning scheme: we take the 66 bins which make up the ND ν_μCC, ND NC, FD ν_μCC, and FD NC spectra and label each bin in that order with a number from 0 to 65. This scheme allows us to consider all samples at once so we can calculate the covariance between each bin and every other bin. The logically binned spectrum for the nominal spectra in the absence of sterile neutrinos can be seen in Figure 7.4.

The systematic fluctuations are applied to a nominal spectrum generated without sterile neutrinos using NOvA's three flavor measurements for the oscillation parameters. The choice to generate our covariance matrix excluding sterile neutrinos does not impact our sensitivity [48]. The reason for this is that when we fit we use the fractional covariance matrix which

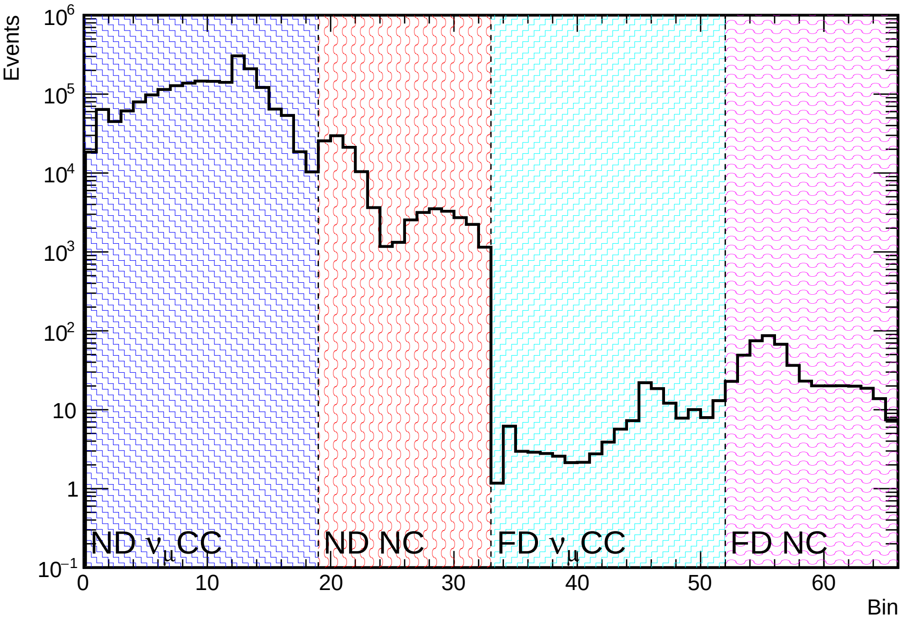

Figure 7.4: The logically binned spectrum for the Asimov spectra generated with nominal three flavor oscillation parameters. Bins 0 to 18 are bins for the ND ν_μCC selection, 19 to 33 are the ND NC selection, 34 to 52 are for the FD ν_μCC selection, and 53 to 66 are for the FD NC selection.

is resilient to the shape changes that oscillations to sterile neutrinos could cause in the spectrum.

We generate $U = 2000$ pseudo-experiments for each systematic parameter [48]. For each pseudo-experiment u we compare the fluctuated content of the i-th logical bin N_i^u to the nominal content of that bin, $\bar{N}_i$. The covariance matrix for each systematic uncertainty is thus

$$C_{i,j} = \frac{1}{U} \sum_{u}^{U} \left(N_i^u - \bar{N}_i\right)\left(N_j^u - \bar{N}_j\right), \tag{7.8}$$

and the fractional covariance matrix is

$$F_{i,j} = \frac{C_{i,j}}{\bar{N}_i \bar{N}_j}. \tag{7.9}$$

The one exception to this procedure is the covariance matrix generated to cover our flux systematic uncertainty. For that systematic we have 100 pre-generated spectra which were generated with different assumptions about the flux. We take these 100 spectra each as a single random choice of our systematic uncertainty parameters and generate a covariance matrix from them [48]. The total fractional covariance matrix used in this analysis can be seen in Figure 7.5.

7.3 Covariance Matrix Test Statistic

Once we have our covariance matrix we can use it to compare two spectra. If $N_i(\Theta)$ is the content of the i-th bin in a spectrum generated with parameters Θ and the bin contents for the (pseudo-)data are N_i^{data}, then we can construct a test statistic as

$$\chi^2 = \sum_{i,j} \left(N_i^{\text{data}} - N_i(\Theta)\right) C_{i,j}^{-1} \left(N_j^{\text{data}} - N_j(\Theta)\right), \tag{7.10}$$

where C^{-1} is the inverse of the covariance matrix C excluding the statistical component. To understand what Equation (7.10) is doing, note that $C_{i,j}^{-1} \propto \frac{1}{C_{i,j}}$, and so the larger the covariance between the two bins, the smaller the

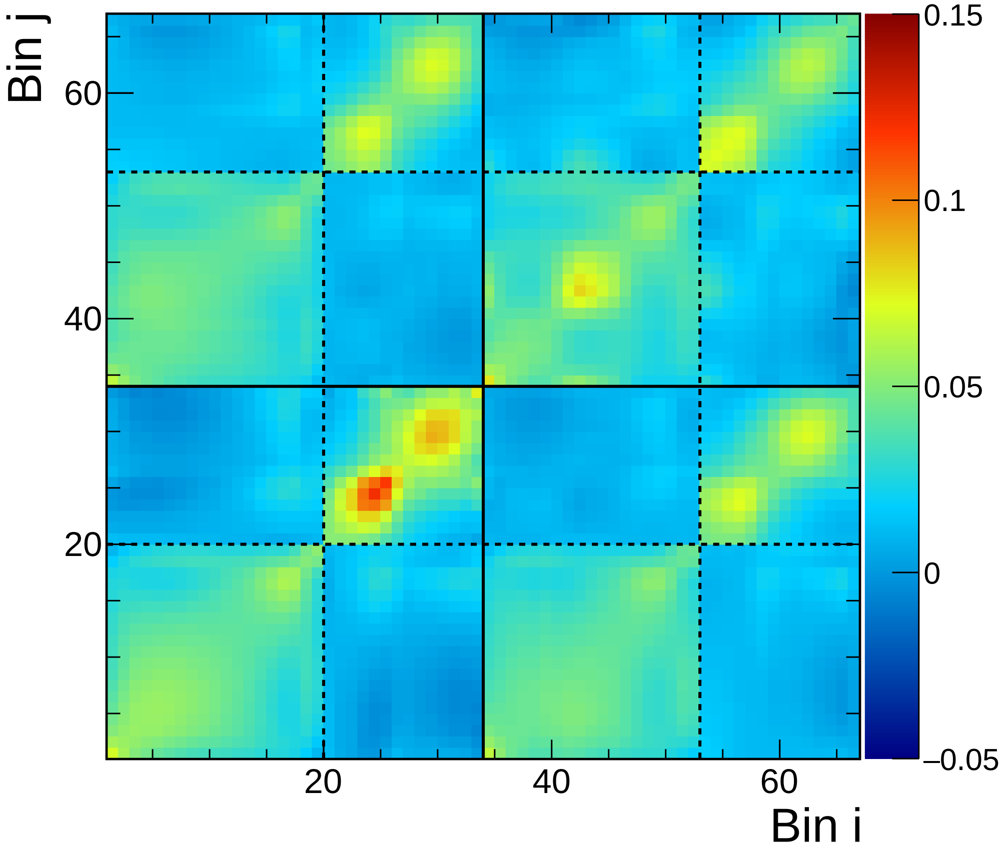

Figure 7.5: The total fractional covariance matrix. The solid lines separate the ND bins (left/down) from the FD bins (right/up). The dashed lines divide the ν_μCC and NC events in each detector with the former on left/lower side and the later on the right/upper side.

contribution to the χ^2.

We are also able to construct a covariance matrix to capture the statistical uncertainty using Equation (7.10). The canonical goodness-of-fit metric for Poisson distributed variables is the Poisson log-likelihood [16],

$$\chi^2_{\mathrm{PLL}} = 2\sum_i \left[N_i(\boldsymbol{\Theta}) - N_i^{\mathrm{data}} \left(1 - \ln \frac{N_i^{\mathrm{data}}}{N_i(\boldsymbol{\Theta})} \right) \right], \tag{7.11}$$

which cannot be replicated by Equation (7.10). However, we can instead use the Combined Neyman-Pearson χ^2 [51]

$$\chi^2_{\mathrm{CNP}} = \sum_i \frac{1}{3} \left(\frac{1}{N_i^{\mathrm{data}}} + \frac{2}{N_i(\boldsymbol{\Theta})} \right)^{-1} \left(N_i(\boldsymbol{\Theta}) - N_i^{\mathrm{data}} \right)^2, \tag{7.12}$$

Which approximates χ^2_{PLL} sufficiently well for our use [52]. This χ^2_{CNP} is compatible with Equation (7.10) with the statistical covariance matrix being

$$C^{\mathrm{statistical}}_{i,i} = \begin{cases} 3\left(\frac{1}{N_i^{\mathrm{data}}} + \frac{2}{N_i(\boldsymbol{\Theta})} \right) & N_i^{\mathrm{data}} > 0 \\ \frac{N_i(\boldsymbol{\Theta})}{2} & N_i^{\mathrm{data}} = 0 \end{cases}. \tag{7.13}$$

This diagonal covariance matrix reproduces Equation (7.12) when used in Equation (7.10) provided $N_i^{\mathrm{data}} > 0$. In the case where $N_i^{\mathrm{data}} = 0$ it instead reproduces Equation (7.11) as for a diagonal matrix $\left(C^{\mathrm{statistical}}\right)^{-1}_{i,i} = \frac{1}{C^{\mathrm{statistical}}_{i,i}}$. Thus by combining the statistical covariance matrix for the data with the total systematic covariance matrix in Figure 7.5 we can use Equation (7.10) to produce χ^2-values comparing the data to a prediction at $\boldsymbol{\Theta}$.

We also include penalty terms in our χ^2 for oscillation parameters which are constrained in the fit. For a parameter $\mu \in \boldsymbol{\Theta}$ with expected value $\bar{\mu}$ and uncertainty σ_μ we add

$$\chi^2_\mu = \frac{(\mu - \bar{\mu})}{\sigma^2_\mu} \tag{7.14}$$

to the χ^2 from Equation (7.10).

7.4 Covariance Matrix In Use

We wish to produce sensitivity contours for the case where there are no sterile neutrinos. We produce these contours by comparing a spectrum produced with fake data without sterile neutrinos to spectra generated with a variety of parameters. In this way we can show which regions of parameter space we expect to exclude under the null hypothesis. We generate many predictions for different $\boldsymbol{\Theta}$, and call the collection of them a prediction library. The predictions are generated with the central values for the systematic parameters; the oscillation parameters are spaced at regular intervals. Table 7.1 show the ranges and number of points used for the prediction libraries. Note that the degenerate values of θ_{23} are only used in the region of parameter space where $\sin^2\theta_{24} > 0.1$ and $\Delta m^2_{41} < 0.01\,\mathrm{eV}^2$. We include these points in our prediction libraries to allow for the potential degeneracy between Δm^2_{41} and Δm^2_{32} in that region.

Oscillation Parameter	Range	Points
θ_{23}	$[0.77, 0.97]$	13
θ_{23} (Degenerate)	$[1.2, \pi/2]$	13
θ_{24}	$[0, \pi/2]$	48
θ_{34}	$[0, \pi/2]$	21
Δm^2_{32} (NH) (eV^2)	$[2.46 \times 10^{-3}, 2.57 \times 10^{-3}]$	16
Δm^2_{32} (IH) (eV^2)	$[-2.66 \times 10^{-3}, -2.36 \times 10^{-3}]$	16
Δm^2_{41} (eV^2)	$[0.01, 100]$	45
δ_{24}	$[0, 2\pi]$	5

Table 7.1: Oscillation parameters varied to create the library of predicted spectra for the four-flavor analyses [48]. The points for Δm^2_{41}, θ_{24}, and θ_{34} are evenly spaced in $\log(\Delta m^2_{41})$, $\log(\sin^2\theta_{24})$, and $\log(\sin^2\theta_{34})$. The points for the remaining parameters are evenly spaced within each range. The degenerate values of θ_{23} are only used in the region of parameter space where $\sin^2\theta_{24} > 0.1$ and $\Delta m^2_{41} < 0.01\,\mathrm{eV}^2$.

7.4.1 Sensitivity

We compare the fake data spectrum to the spectra produced at each point in Table 7.1. When we wish to create sensitivity contours in, for example, the $\sin^2\theta_{24}$-Δm^2_{41} space we plot the minimum values of of χ^2 for each choice of $\sin^2\theta_{24}$ and Δm^2_{41} and subtract off the minimum value of χ^2 from all predictions. By Wilkes' theorem, for two parameters the 90% confidence level is given by $\Delta\chi^2 = \chi^2 - \chi^2_{\mathrm{min}} < 4.61$ [16]. However, the oscillation parameters governing neutrino oscillations are physically bounded by $|\Delta m^2| > 0$ and $0 < \sin^2\theta < 1$. Due to these physical boundaries we should instead use a Feldman-Cousins procedure to find the critical values of $\Delta\chi^2$ [53]. The planned implementation for our Feldman-Cousins procedure is described in §7.4.2, but is as yet unimplemented. For our fake data with no sterile

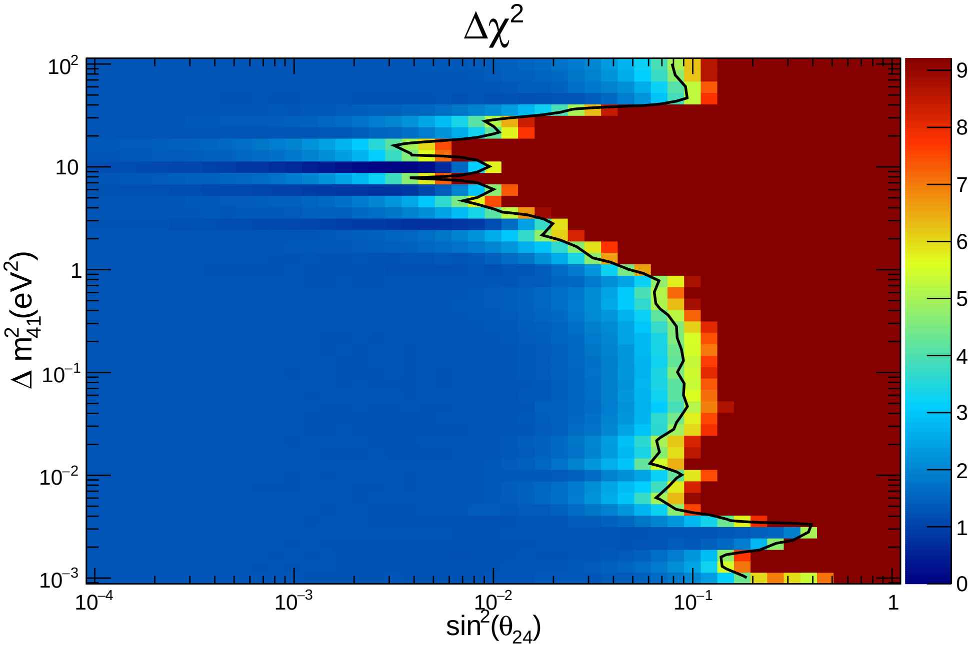

Figure 7.6: The 90% confidence level contour and $\Delta\chi^2$-values for a fake data spectrum without sterile neutrinos. The color scale shows the value of $\Delta\chi^2$ for each point of $\sin^2\theta_{24}$-Δm^2_{41} from the values in Table 7.1. The black line is the Wilks' 90% confidence level contour.

neutrinos we have the 90% confidence level contour and $\Delta\chi^2$-values for the Asimov sensitivities shown in Figure 7.6.

We also generated 500 statistically and systematically fluctuated fake data spectra without sterile neutrinos. Fitting these spectra we construct a median sensitivity by constructing the surface where each grid point takes the median of all the 500 $\Delta\chi^2$-values computed at that point. We can then construct a 90% confidence level contour from these $\Delta\chi^2$-values as seen in Figure 7.7. The median sensitivity excludes more of the parameter space than the Asimov sensitivities, but as the Asimov is only an approximation

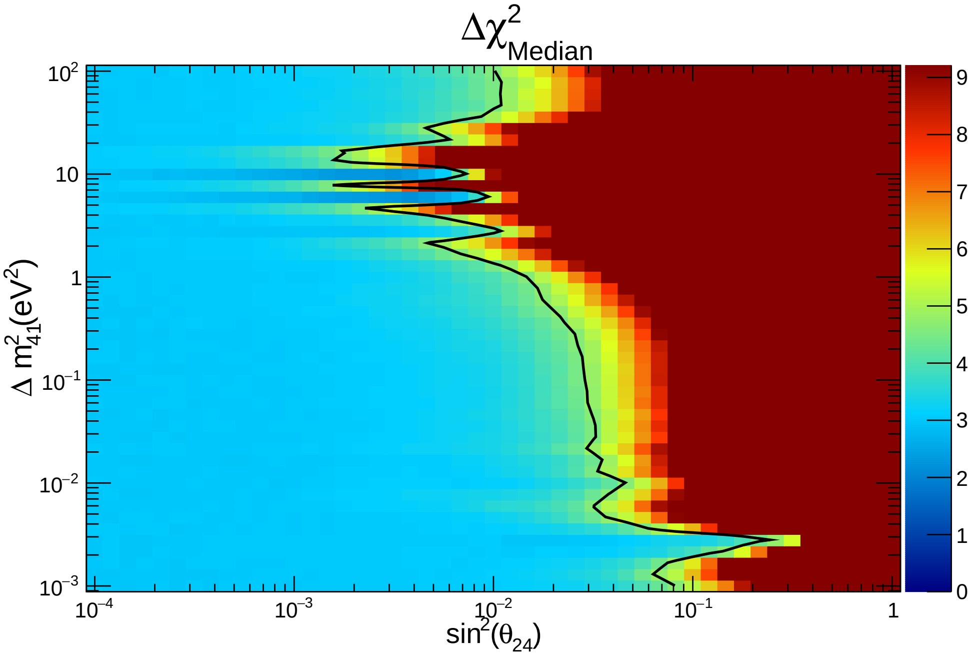

Figure 7.7: The median 90% confidence level contour and $\Delta\chi^2$-values from 500 statistically and systematically fluctuated fake data spectra without sterile neutrinos. The color scale shows the value of $\Delta\chi^2_{\mathrm{Median}}$ for each point of $\sin^2\theta_{24}$-Δm^2_{41} from the values in Table 7.1. The black line is the Median 90% confidence level contour drawn from the median value of $\Delta\chi^2$ at each grid point.

of the median sensitivity this is unsurprising [54]. We can also calculate how many of the 500 fluctuated spectra are allowed at the 90% confidence level at each grid point, as can be seen in Figure 7.8. Note that drawing the contour at $\Delta\chi^2_{\mathrm{median}} = 4.61$ is equivalent to drawing it where there are 250 allowed universes at the 90% confidence level.

Our sensitivity in the region of large Δm^2_{41} is driven by our data in the ND. As discussed at the start of Chapter 7 and shown in Figure 7.1, for $\Delta m^2_{41} \gtrsim 0.5\,\mathrm{eV}^2/c^4$ we expect oscillations to occur before the neutrinos

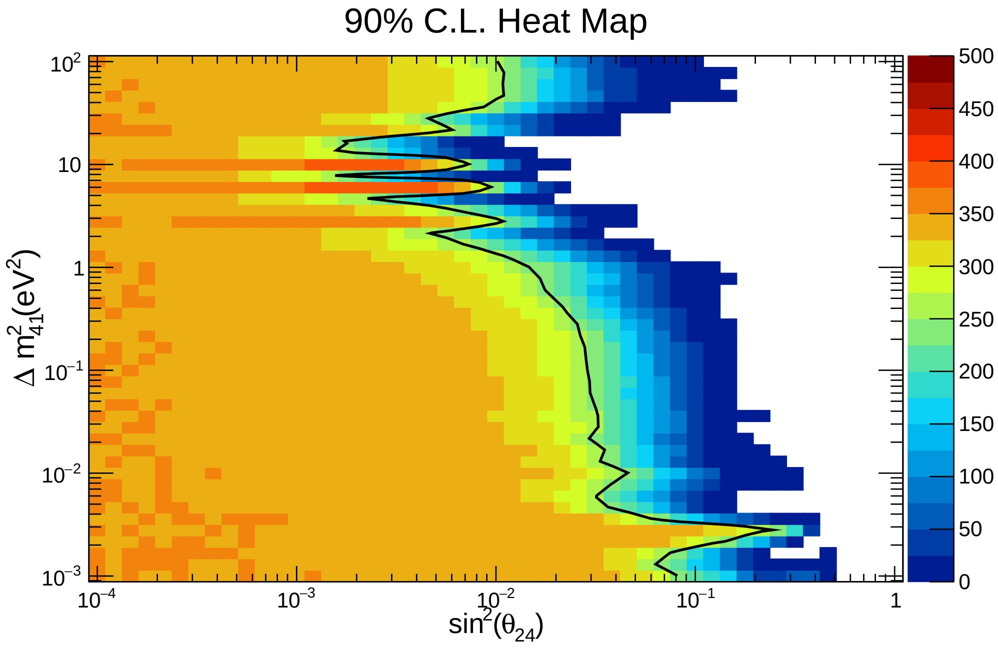

Figure 7.8: The median 90% confidence level contour and the number of statistically and systematically fluctuated fake data spectra without sterile neutrinos for which that grid point is allowed within the Wilks' 90% confidence level. The black line is the Median 90% confidence level contour drawn from the median value of $\Delta\chi^2$ at each grid point.

reach the ND. This is due to the value of L/E_ν in for the shorter ND baseline. In the FD, $\Delta m^2_{41} \gtrsim 0.5\,\mathrm{eV}^2/c^4$ causes a frequency of oscillations too rapid to be observed at our energy resolution. These rapid oscillations average out when we bin our events, and so would be unobservable. This is illustrated in Figure 7.9. From Figure 7.9 we can see that the oscillations caused by $\Delta m^2_{41} \gtrsim 0.5\,\mathrm{eV}^2/c^4$ could not be distinguished from oscillations at lower values of Δm^2_{41} with the FD alone. However, the ND allows us to discriminate between different values of Δm^2_{41} in the $\Delta m^2_{41} \gtrsim 0.5\,\mathrm{eV}^2/c^4$ regime. The effect is that the ND is what drives our sensitivity for larger values of Δm^2_{41}. Vice versa when $\Delta m^2_{41} \lesssim 0.5\,\mathrm{eV}^2/c^4$ there are no observable oscillations to sterile states occurring at the ND baseline. We can therefor split the parameter space into ND and FD dominated regions approximately separated by $\Delta m^2_{41} \sim 0.5\,\mathrm{eV}^2/c^4$.

For $\Delta m^2_{41} \sim 3 \times 10^{-3}\,\mathrm{eV}^2/c^4$ we lose sensitivity for oscillations to sterile flavors. This degradation occurs because at these values there is a degeneracy between Δm^2_{41} and Δm^2_{32} for $\sin^2\theta_{24} \sim 0.5$. At these values atmospheric neutrino oscillations can be driven in part by Δm^2_{41}. In this case the effects of the oscillations driven by the two mass-squared splittings are indistinguishable to us, and so we cannot measure Δm^2_{41}.

Our systematic uncertainties primarily degrade our sensitivity in the region where Δm^2_{41} is large. This is because the limiting factor in the FD dominated region is the low number of neutrino events we see in the FD. The primary systematic uncertainties which limit our sensitivity are due to uncertainty in the composition of the beam flux, the calibration, and our understanding of the neutrino cross section. These uncertainties are characterize by 1, 7, and 62 systematic parameters respectively.

7.4.2 Feldman-Cousins Procedure

To obtain Feldman-Cousins corrected critical values for $\Delta\chi^2$ we will generate 1000 spectra for each point in the contour space. We will use a profiled Feldman-Cousins approach, where we take the oscillation parameters, in-

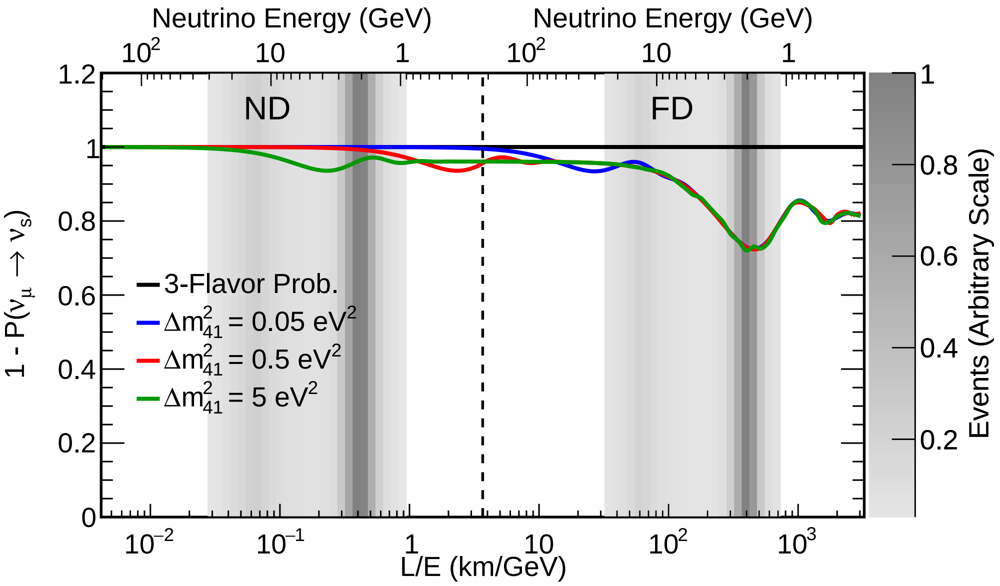

Figure 7.9: Averaged probability that muon neutrinos do not oscillate to the sterile flavor for $\Delta m^2_{41} = 0.05\,\text{eV}^2/\text{c}^4$, $0.5\,\text{eV}^2/\text{c}^4$, and $5\,\text{eV}^2/\text{c}^4$. The probabilities are averaged over the neutrino energy to mimic the effect of our limited energy resolution. Note that the probabilities are nearly identical in the region of L/E_ν that the FD sees. Image courtesy of the NOvA Collaboration.

cluding hidden parameters, to be the best fit values at that point [55]. These spectra will be systematically and statistically fluctuated in the same way we fluctuate our normal pseudo-experiements. For each spectrum we will compute the χ^2 from comparing the fluctuated universe to the Asimov prediction with those oscillation parameters. We call this χ^2-value χ^2_{Input}. We will then perform the same χ^2 minimization as described in §7.4 to obtain χ^2_{min}. For each of the 1000 spectra we will calculate $\Delta\chi^2_{\text{FC}} = \chi^2_{\text{Input}} - \chi^2_{\text{min}}$. We will take the value of $\Delta\chi^2_{\text{FC}}$ which is greater than 90% of all values of $\Delta\chi^2_{\text{FC}}$ as $\Delta\chi^2_c$. The 90% confidence level at the grid point is defined by $\Delta\chi^2 < \Delta\chi^2_c$. By calculating $\Delta\chi^2_c$ for each point in the contour space we will be able to draw

Feldman-Cousins corrected contours. These contours will account for the physical boundaries in the neutrino oscillation parameters in accordance with the Feldman-Cousins procedure [53]. At time of writing we are in the process of generating and fitting the required spectra to calculate $\Delta\chi^2_c$ at each grid point.

7.5 Data Fit

Our data spectra can be seen in Figure 7.10. The number of events in each selection can be seen in Table 7.2. Note that we do not expect that the number of events should agree even in the absence of sterile neutrinos. These predictions were made using the central values of our systematic parameters. We performed a global MINUIT minimization of the χ^2 calculated from our covariance matrix as defined in Equation (7.10). The best fit parameters are listed in Table 7.3. A comparison of the data spectra to MC generated at the best fit parameters is shown in Figure 7.11. Note that the MC spectra were generated with the central values for our systematic parameters as we do not calculate them as part of our fitting procedure—we do not expect the spectra to perfectly align. The 90% confidence level contours from the data are shown in Figure 7.12. The contours are consistent with our Asimov and median sensitivities to the three flavor model. In fact, the data contours exclude a greater region of parameter space than the Asimov or median contours. We do see an island of allowed parameter space near $\sin^2(\theta_{24}) = 0.4$,

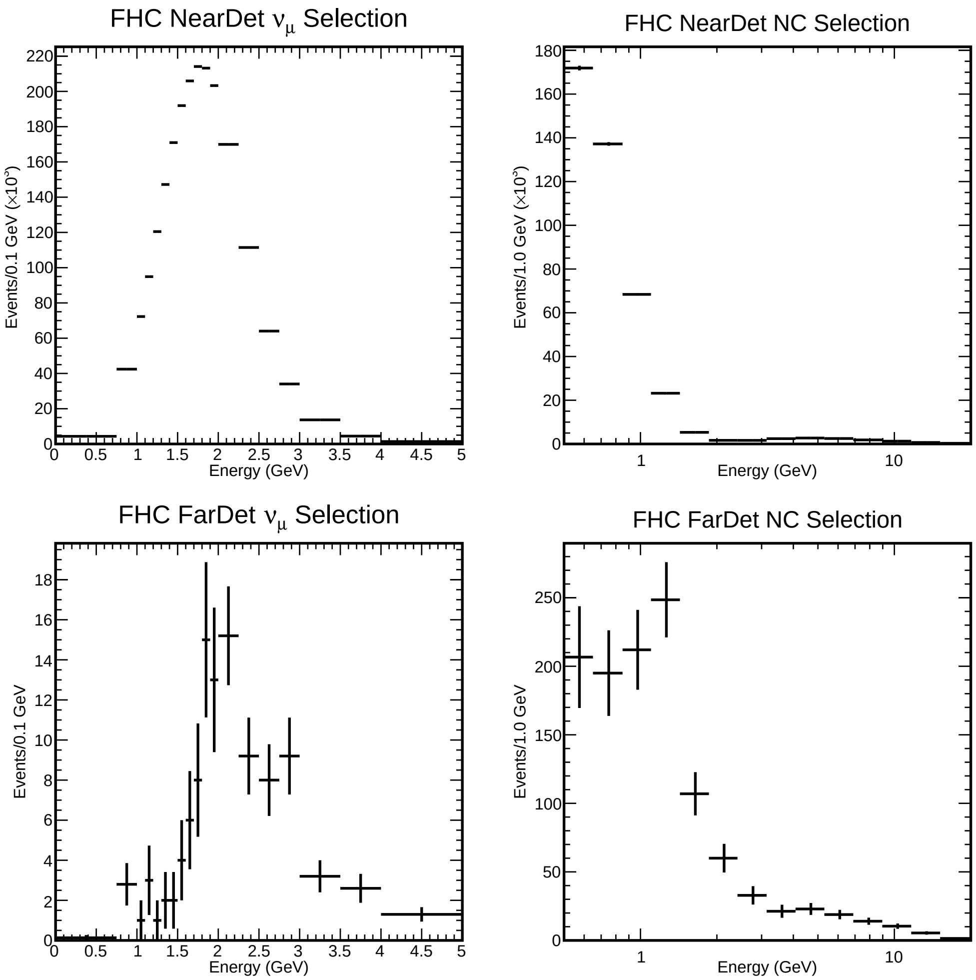
FHC NearDet ν_μ Selection

FHC NearDet NC Selection

FHC FarDet ν_μ Selection

FHC FarDet NC Selection

Figure 7.10: The data spectra for this analysis. Note that the ν_μCC spectra are normalized by the 0.1 GeV bin width while the NC spectra are normalized by a 1 GeV bin width. Additionally the NC spectra are presented with the energy on a logarithmic scale.

$\Delta m^2_{41} = 5 \times 10^{-3}\ \mathrm{eV}^2/c^4$, which is due the potential for degeneracy between Δm^2_{41} and Δm^2_{32}.

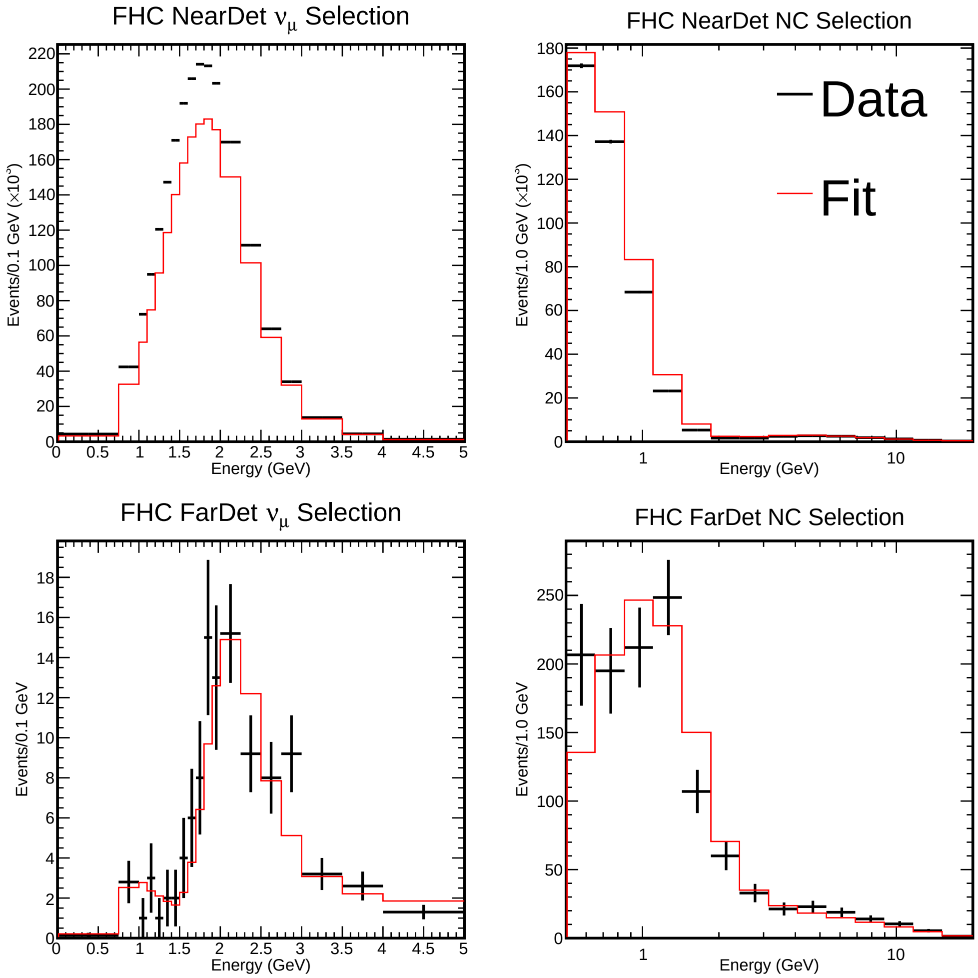

Figure 7.11: The data spectra for the ND/FD ν_μCC/NC selection. These spectra are compared to MC generated with the best fit oscillation parameters. Because our method does not fit for systematic parameters the MC was generated with the central values for all systematic parameters.

Selection	Predicted Events	Data Events	Difference
ND ν_μCC	2444833.6	2826070	−381236.4
ND NC	116739.6	103109	13630.6
FD ν_μCC	180.53	209	−28.47
FD NC	476.77	469	7.77
ND Cosmic Background	0	—	—
FD Cosmic Background	92.15	—	—

Table 7.2: The number of events predicted in each sample under the three flavor model and the number of observed events in data. Note that we do not have the number of cosmic background events in the data as such events would be part of the data samples.

	Best Fit Value
χ^2	58.61
Δm^2_{32}	$-2.42027 \times 10^{-3}\,\mathrm{eV}^2/c^4$
Δm^2_{41}	$7.39484\,\mathrm{eV}^2/c^4$
θ_{23}	0.777312
θ_{24}	0.0759573
θ_{34}	0.146648
δ_{24}	4.34316

Table 7.3: The parameters obtained from the best fit of the data spectra.

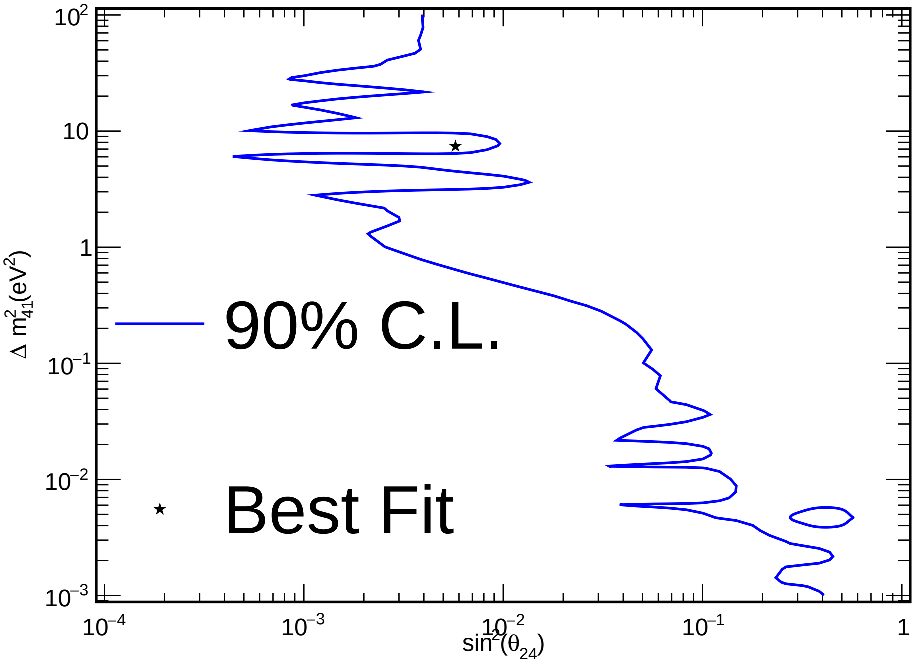

Figure 7.12: The Wilkes' Theorem 90% C.L. contours from our data fit and the location of the best fit point. The region to the right of the contour is excluded at the 90% confidence level apart from the region near $\sin^2(\theta_{24}) = 0.4$, $\Delta m^2_{41} = 5 \times 10^{-3}\ \text{eV}^2/\text{c}^4$. This island of inclusion is due to the potential for degeneracy between Δm^2_{41} and Δm^2_{32}.

Chapter 8

Conclusion

We performed a two-detector fit of the NOvA data in a search for sterile neutrinos and found a result consistent with no sterile neutrinos. This fit was performed using a covariance matrix fitting technique which allowed us to leverage the ND events in the fit to better constrain our uncertainty in the lower statistics FD sample. A two-detector fit also allows us sensitivity to a larger range of Δm^2_{41}.

The Feldman-Cousin correction procedure has been developed but not yet implemented due to the computational intensity of the process. Future work is required to obtain Feldman-Cousin corrected sensitivity contours which will accurately show how much of parameter space is excluded. Additional sensitivity could be achieved with the inclusion of NOvA's antineutrino data in a future analysis.

The results presented here are consistent with the latest sterile neutrino searches from IceCube [56] and MicroBooNE[57, 58, 59], which saw results consistent with no sterile neutrinos. However, we should be cautious comparing our sensitivities until our Feldman-Cousins corrected results are finalized.

These results show results consistent with no sterile neutrinos, and exclude a greater region of oscillation parameter space than our sensitivity studies suggested. From this result we can expect that our analysis will place strong limits on the potential for sterile neutrino flavors.

DISCARD THIS PAGE

Colophon

The font used is Vollkorn, which is published under an SIL Open Font License. More information can be found at `http://vollkorn-typeface.com/`.

The LaTeX formatting was based off of Will Benton's `wi-thesis-template` which can be found at `https://github.com/willb/wi-thesis-template`.

Bibliography

[1] Wolfgang Pauli. Pauli letter collection: letter to Lise Meitner. Typed copy. URL `https://cds.cern.ch/record/83282`.

[2] Clyde L Cowan Jr, Frederick Reines, FB Harrison, HW Kruse, and AD McGuire. Detection of the free neutrino: a confirmation. *Science*, 124(3212):103–104, 1956.

[3] R. L. Workman and Others. Review of Particle Physics. *PTEP*, 2022: 083C01, 2022. doi: 10.1093/ptep/ptac097.

[4] Per Olof Hulth. High energy neutrinos from the cosmos. `https://www.nobelprize.org/prizes/themes/high-energy-neutrinos-from-the-cosmos`, March 2005. URL `https://www.nobelprize.org/prizes/themes/high-energy-neutrinos-from-the-cosmos/`.

[5] John N. Bahcall. Solar neutrinos. i. theoretical. *Phys. Rev. Lett.*, 12: 300–302, March 1964. doi: 10.1103/PhysRevLett.12.300. URL `https://link.aps.org/doi/10.1103/PhysRevLett.12.300`.

[6] Raymond Davis. Solar neutrinos. ii. experimental. *Phys. Rev. Lett.*, 12: 303–305, March 1964. doi: 10.1103/PhysRevLett.12.303. URL `https://link.aps.org/doi/10.1103/PhysRevLett.12.303`.

[7] T. J. Haines, R. M. Bionta, G. Blewitt, C. B. Bratton, D. Casper, R. Claus, B. G. Cortez, S. Errede, G. W. Foster, W. Gajewski, K. S. Ganezer, M. Goldhaber, T. W. Jones, D. Kielczewska, W. R. Kropp, J. G. Learned, E. Lehmann, J. M. LoSecco, J. Matthews, H. S. Park, L. R. Price, F. Reines, J. Schultz, S. Seidel, E. Shumard, D. Sinclair, H. W. Sobel, J. L. Stone, L. Sulak, R. Svoboda, J. C. van der Velde, and C. Wuest. Calculation of atmospheric neutrino-induced backgrounds in a nucleon-decay search. *Phys. Rev. Lett.*, 57:1986–1989, Oct 1986. doi: 10.1103/PhysRevLett.57.1986. URL `https://link.aps.org/doi/10.1103/PhysRevLett.57.1986`.

[8] Masayuki Nakahata, Katsushi Arisaka, Takaaki Kajita, Masatoshi Koshiba, Yuichi Oyama, Atsuto Suzuki, Masato Takita, Yoji Totsuka, Tadashi Kifune, Teruhiro Suda, Nobuaki Sato, Kasuke Takahashi, and Kazumasa Miyano. Atmospheric neutrino background and pion nuclear effect for kamioka nucleon decay experiment. *Journal of the Physical Society of Japan*, 55(11):3786–3805, 1986. doi: 10.1143/JPSJ.55.3786. URL `https://doi.org/10.1143/JPSJ.55.3786`.

[9] Y. Fukuda, T. Hayakawa, E. Ichihara, K. Inoue, K. Ishihara, H. Ishino, Y. Itow, T. Kajita, J. Kameda, S. Kasuga, K. Kobayashi, Y. Kobayashi, Y. Koshio, M. Miura, M. Nakahata, S. Nakayama, A. Okada, K. Okumura,

N. Sakurai, M. Shiozawa, Y. Suzuki, Y. Takeuchi, Y. Totsuka, S. Yamada, M. Earl, A. Habig, E. Kearns, M. D. Messier, K. Scholberg, J. L. Stone, L. R. Sulak, C. W. Walter, M. Goldhaber, T. Barszczxak, D. Casper, W. Gajewski, P. G. Halverson, J. Hsu, W. R. Kropp, L. R. Price, F. Reines, M. Smy, H. W. Sobel, M. R. Vagins, K. S. Ganezer, W. E. Keig, R. W. Ellsworth, S. Tasaka, J. W. Flanagan, A. Kibayashi, J. G. Learned, S. Matsuno, V. J. Stenger, D. Takemori, T. Ishii, J. Kanzaki, T. Kobayashi, S. Mine, K. Nakamura, K. Nishikawa, Y. Oyama, A. Sakai, M. Sakuda, O. Sasaki, S. Echigo, M. Kohama, A. T. Suzuki, T. J. Haines, E. Blaufuss, B. K. Kim, R. Sanford, R. Svoboda, M. L. Chen, Z. Conner, J. A. Goodman, G. W. Sullivan, J. Hill, C. K. Jung, K. Martens, C. Mauger, C. McGrew, E. Sharkey, B. Viren, C. Yanagisawa, W. Doki, K. Miyano, H. Okazawa, C. Saji, M. Takahata, Y. Nagashima, M. Takita, T. Yamaguchi, M. Yoshida, S. B. Kim, M. Etoh, K. Fujita, A. Hasegawa, T. Hasegawa, S. Hatakeyama, T. Iwamoto, M. Koga, T. Maruyama, H. Ogawa, J. Shirai, A. Suzuki, F. Tsushima, M. Koshiba, M. Nemoto, K. Nishijima, T. Futagami, Y. Hayato, Y. Kanaya, K. Kaneyuki, Y. Watanabe, D. Kielczewska, R. A. Doyle, J. S. George, A. L. Stachyra, L. L. Wai, R. J. Wilkes, and K. K. Young. Evidence for oscillation of atmospheric neutrinos. *Phys. Rev. Lett.*, 81: 1562–1567, Aug 1998. doi: 10.1103/PhysRevLett.81.1562. URL `https://link.aps.org/doi/10.1103/PhysRevLett.81.1562`.

[10] Q. R. Ahmad, R. C. Allen, T. C. Andersen, J. D. Anglin, G. Bühler, J. C. Barton, E. W. Beier, M. Bercovitch, J. Bigu, S. Biller, R. A. Black, I. Blevis,

R. J. Boardman, J. Boger, E. Bonvin, M. G. Boulay, M. G. Bowler, T. J. Bowles, S. J. Brice, M. C. Browne, T. V. Bullard, T. H. Burritt, K. Cameron, J. Cameron, Y. D. Chan, M. Chen, H. H. Chen, X. Chen, M. C. Chon, B. T. Cleveland, E. T. H. Clifford, J. H. M. Cowan, D. F. Cowen, G. A. Cox, Y. Dai, X. Dai, F. Dalnoki-Veress, W. F. Davidson, P. J. Doe, G. Doucas, M. R. Dragowsky, C. A. Duba, F. A. Duncan, J. Dunmore, E. D. Earle, S. R. Elliott, H. C. Evans, G. T. Ewan, J. Farine, H. Fergani, A. P. Ferraris, R. J. Ford, M. M. Fowler, K. Frame, E. D. Frank, W. Frati, J. V. Germani, S. Gil, A. Goldschmidt, D. R. Grant, R. L. Hahn, A. L. Hallin, E. D. Hallman, A. Hamer, A. A. Hamian, R. U. Haq, C. K. Hargrove, P. J. Harvey, R. Hazama, R. Heaton, K. M. Heeger, W. J. Heintzelman, J. Heise, R. L. Helmer, J. D. Hepburn, H. Heron, J. Hewett, A. Hime, M. Howe, J. G. Hykawy, M. C. P. Isaac, P. Jagam, N. A. Jelley, C. Jillings, G. Jonkmans, J. Karn, P. T. Keener, K. Kirch, J. R. Klein, A. B. Knox, R. J. Komar, R. Kouzes, T. Kutter, C. C. M. Kyba, J. Law, I. T. Lawson, M. Lay, H. W. Lee, K. T. Lesko, J. R. Leslie, I. Levine, W. Locke, M. M. Lowry, S. Luoma, J. Lyon, S. Majerus, H. B. Mak, A. D. Marino, N. McCauley, A. B. McDonald, D. S. McDonald, K. McFarlane, G. McGregor, W. McLatchie, R. Meijer Drees, H. Mes, C. Mifflin, G. G. Miller, G. Milton, B. A. Moffat, M. Moorhead, C. W. Nally, M. S. Neubauer, F. M. Newcomer, H. S. Ng, A. J. Noble, E. B. Norman, V. M. Novikov, M. O'Neill, C. E. Okada, R. W. Ollerhead, M. Omori, J. L. Orrell, S. M. Oser, A. W. P. Poon, T. J. Radcliffe, A. Roberge, B. C. Robertson, R. G. H. Robertson, J. K. Rowley,

V. L. Rusu, E. Saettler, K. K. Schaffer, A. Schuelke, M. H. Schwendener, H. Seifert, M. Shatkay, J. J. Simpson, D. Sinclair, P. Skensved, A. R. Smith, M. W. E. Smith, N. Starinsky, T. D. Steiger, R. G. Stokstad, R. S. Storey, B. Sur, R. Tafirout, N. Tagg, N. W. Tanner, R. K. Taplin, M. Thorman, P. Thornewell, P. T. Trent, Y. I. Tserkovnyak, R. Van Berg, R. G. Van de Water, C. J. Virtue, C. E. Waltham, J.-X. Wang, D. L. Wark, N. West, J. B. Wilhelmy, J. F. Wilkerson, J. Wilson, P. Wittich, J. M. Wouters, and M. Yeh. Measurement of the rate of $\nu_e + \mathrm{d} \to \mathrm{p} + \mathrm{p} + \mathrm{e}^-$ interactions produced by $^8\mathrm{b}$ solar neutrinos at the sudbury neutrino observatory. *Phys. Rev. Lett.*, 87:071301, Jul 2001. doi: 10.1103/PhysRevLett.87.071301. URL `https://link.aps.org/doi/10.1103/PhysRevLett.87.071301`.

[11] Herbert H. Chen. Direct approach to resolve the solar-neutrino problem. *Phys. Rev. Lett.*, 55:1534–1536, September 1985. doi: 10.1103/PhysRevLett.55.1534. URL `https://link.aps.org/doi/10.1103/PhysRevLett.55.1534`.

[12] A. Aguilar, L. B. Auerbach, R. L. Burman, D. O. Caldwell, E. D. Church, A. K. Cochran, J. B. Donahue, A. Fazely, G. T. Garvey, R. M. Gunasingha, R. Imlay, W. C. Louis, R. Majkic, A. Malik, W. Metcalf, G. B. Mills, V. Sandberg, D. Smith, I. Stancu, M. Sung, R. Tayloe, G. J. VanDalen, W. Vernon, N. Wadia, D. H. White, and S. Yellin. Evidence for neutrino oscillations from the observation of $\overline{\nu}_e$ appearance in a $\overline{\nu}_\mu$ beam. *Phys. Rev. D*, 64:112007, Nov 2001. doi: 10.1103/PhysRevD.64.112007. URL

https://link.aps.org/doi/10.1103/PhysRevD.64.112007.

[13] Precision electroweak measurements on the z resonance. *Physics Reports*, 427(5):257–454, 2006. ISSN 0370-1573. doi: https://doi.org/10.1016/j.physrep.2005.12.006. URL `https://www.sciencedirect.com/science/article/pii/S0370157305005119`.

[14] Harry Hausner and Brian Rebel. 2020 NC Energy Estimation. `https://nova-docdb.fnal.gov/cgi-bin/sso/RetrieveFile?docid=46448&filename=ncEnergyCorrectionTechNote.pdf&version=2`, July 2020. URL `https://nova-docdb.fnal.gov/cgi-bin/sso/RetrieveFile?docid=46448&filename=ncEnergyCorrectionTechNote.pdf&version=2`.

[15] Jorge S. Díaz and V. Alan Kostelecký. Lorentz- and cpt-violating models for neutrino oscillations. *Phys. Rev. D*, 85:016013, Jan 2012. doi: 10.1103/PhysRevD.85.016013. URL `https://link.aps.org/doi/10.1103/PhysRevD.85.016013`.

[16] P.A. Zyla et al. Review of Particle Physics. *PTEP*, 2020(8):083C01, 2020. doi: 10.1093/ptep/ptaa104.

[17] André de Gouvêa, James Jenkins, and Boris Kayser. Neutrino mass hierarchy, vacuum oscillations, and vanishing $|U_{e3}|$. *Phys. Rev. D*, 71:113009, Jun 2005. doi: 10.1103/PhysRevD.71.113009. URL `https://link.aps.org/doi/10.1103/PhysRevD.71.113009`.

[18] G.L. Fogli, E. Lisi, A. Marrone, D. Montanino, and A. Palazzo. Neutrino mixing phenomenology. *Nuclear Physics B - Proceedings Supplements*, 111(1):106–115, 2002. ISSN 0920-5632. doi: https://doi.org/10.1016/S0920-5632(02)01691-2. URL `https://www.sciencedirect.com/science/article/pii/S0920563202016912`.

[19] H. A. Bethe. Possible explanation of the solar-neutrino puzzle. *Phys. Rev. Lett.*, 56:1305–1308, Mar 1986. doi: 10.1103/PhysRevLett.56.1305. URL `https://link.aps.org/doi/10.1103/PhysRevLett.56.1305`.

[20] Ziro Maki, Masami Nakagawa, and Shoichi Sakata. Remarks on the Unified Model of Elementary Particles. *Progress of Theoretical Physics*, 28 (5):870–880, 11 1962. ISSN 0033-068X. doi: 10.1143/PTP.28.870. URL `https://doi.org/10.1143/PTP.28.870`.

[21] H. Fritzsch and J. Plankl. Mixing of quark flavors. *Phys. Rev. D*, 35: 1732–1735, Mar 1987. doi: 10.1103/PhysRevD.35.1732. URL `https://link.aps.org/doi/10.1103/PhysRevD.35.1732`.

[22] Carlo Giunti and Chung Wook. Kim. *Fundamentals of Neutrino Physics and Astrophysics*. Oxford University Press, 2016.

[23] D. S. Ayres et al. The NOvA Technical Design Report. 10 2007. doi: 10.2172/935497.

[24] P. Adamson et al. The NuMI neutrino beam. *Nuclear Instruments and Methods in Physics Research Section A: Accelerators, Spectrometers, De-*

tectors and Associated Equipment, 806:279–306, 2016. ISSN 0168-9002. doi: https://doi.org/10.1016/j.nima.2015.08.063. URL `https://www.sciencedirect.com/science/article/pii/S016890021501027X`.

[25] D. Ayres. Nova proposal to build a 30 kiloton off-axis detector to study neutrino oscillations in the fermilab numi beamline, 2005.

[26] P. Adamson et al. First measurement of neutrino oscillation parameters using neutrinos and antineutrinos by nova. *Phys. Rev. Lett.*, 123: 151803, October 2019. doi: 10.1103/PhysRevLett.123.151803. URL `https://link.aps.org/doi/10.1103/PhysRevLett.123.151803`.

[27] Accelerator Division — Operations Department. Concepts rookie book. `https://operations.fnal.gov/rookie_books/concepts.pdf`, 2020. URL `https://operations.fnal.gov/rookie_books/concepts.pdf`.

[28] D. S. Ayres et al. The NOvA Technical Design Report. October 2007. doi: 10.2172/935497.

[29] S. Mufson, B. Baugh, C. Bower, T.E. Coan, J. Cooper, L. Corwin, J.A. Karty, P. Mason, M.D. Messier, A. Pla-Dalmau, and M. Proudfoot. Liquid scintillator production for the NOvA experiment. *Nuclear Instruments and Methods in Physics Research Section A: Accelerators, Spectrometers, Detectors and Associated Equipment*, 799:1–9, 2015. ISSN 0168-9002.

doi: https://doi.org/10.1016/j.nima.2015.07.026. URL `https://www.sciencedirect.com/science/article/pii/S0168900215008554`.

[30] Luke Vinton. Calorimetric Energy Scale Calibration of the NOvA Detectors. `https://nova-docdb.fnal.gov/cgi-bin/private/RetrieveFile?docid=13579&filename=CalorimetricEnergyScale.pdf&version=35`, July 2015. URL `https://nova-docdb.fnal.gov/cgi-bin/private/RetrieveFile?docid=13579&filename=CalorimetricEnergyScale.pdf&version=35`.

[31] Christopher Backhouse, Alexander Radovic, Prabhjot Singh, and Medbh Campbell. The Attenuation and Threshold Calibration of the NOvA Detectors. `https://nova-docdb.fnal.gov/cgi-bin/sso/RetrieveFile?docid=13579&filename=calib_technote_3rdana.pdf&version=35`, September 2017. URL `https://nova-docdb.fnal.gov/cgi-bin/sso/RetrieveFile?docid=13579&filename=calib_technote_3rdana.pdf&version=35`.

[32] Prabhjot Singh. Attenuation Calibration of the NOvA Detectors. `https://nusoft.fnal.gov/nova/blessedplots/#!/doc/15472`, June 2016. URL `https://nusoft.fnal.gov/nova/blessedplots/#!/doc/15472`.

[33] Luke Vinton. Calorimetric Energy Scale Calibration. `https://nusoft.fnal.gov/nova/blessedplots/#!/doc/13607`, July 2015. URL `https://nusoft.fnal.gov/nova/blessedplots/#!/doc/13607`.

[34] Diana Patricia Méndez. Second Analysis Calorimetric Energy Scale Calibration of the NOvA detectors. `https://nova-docdb.fnal.gov/cgi-bin/sso/RetrieveFile?docid=13579&filename=calib_technoteSA.pdf&version=35`, April 2016. URL `https://nova-docdb.fnal.gov/cgi-bin/sso/RetrieveFile?docid=13579&filename=calib_technoteSA.pdf&version=35`.

[35] Erika Catano-Mur, Bannanje Nitish Nayak, Andrew Thomas Cleve Sutton, and Thomas Warburton. Event selection for the 2020 3-flavor analysis. `https://nova-docdb.fnal.gov/cgi-bin/sso/RetrieveFile?docid=44040&filename=2020_Ana_3_flavor_selection_technote.pdf&version=2`, March 2020. URL `https://nova-docdb.fnal.gov/cgi-bin/sso/RetrieveFile?docid=44040&filename=2020_Ana_3_flavor_selection_technote.pdf&version=2`.

[36] Michael D. Baird. A Side By Side Comparison of Slicer, Cosmic Slicer, and Slicer4D. `https://nova-docdb.fnal.gov/cgi-bin/sso/RetrieveFile?docid=9195&filename=Slicer4D_technote.pdf&version=1`, March 2013. URL `https://nova-docdb.fnal.gov/cgi-bin/sso/RetrieveFile?docid=9195&filename=Slicer4D_technote.pdf&version=1`.

[37] Robert MacCoun and Saul Perlmutter. Blind analysis: Hide results to seek the truth. *Nature*, 526(7572):187–189, October 2015. doi: 10.1038/526187a. URL `https://doi.org/10.1038/526187a`.

[38] Michael Baird. Tech Note for the Multi-Hough Transform. `https://nova-docdb.fnal.gov/cgi-bin/sso/RetrieveFile?docid=8241&filename=MultiHoughTransform.pdf&version=1`, November 2012. URL `https://nova-docdb.fnal.gov/cgi-bin/sso/RetrieveFile?docid=8241&filename=MultiHoughTransform.pdf&version=1`.

[39] Michael Baird. Vertex reconstruction based on elastic arms. `https://nova-docdb.fnal.gov/cgi-bin/sso/RetrieveFile?docid=7530&filename=ElasticArms.pdf&version=4`, June 2012. URL `https://nova-docdb.fnal.gov/cgi-bin/sso/RetrieveFile?docid=7530&filename=ElasticArms.pdf&version=4`.

[40] Evan Niner. Technical note of FuzzyKVertex reconstruction. `https://nova-docdb.fnal.gov/cgi-bin/sso/RetrieveFile?docid=7648&filename=fuzzykreport.pdf&version=2`, July 2012. URL `https://nova-docdb.fnal.gov/cgi-bin/sso/RetrieveFile?docid=7648&filename=fuzzykreport.pdf&version=2`.

[41] Kanika Sachdev. CalE Scale For ν_e. `https://nova-docdb.fnal.gov/cgi-bin/sso/RetrieveFile?docid=11528&filename=cale_scale_2014_06_28.pdf&version=1`, June 2014. URL `https://nova-docdb.fnal.gov/cgi-bin/sso/RetrieveFile?docid=11528&filename=cale_scale_2014_06_28.pdf&version=1`.

[42] A. Aurisano, A. Radovic, D. Rocco, A. Himmel, M.D. Messier, E. Niner, G. Pawloski, F. Psihas, A. Sousa, and P. Vahle. A convolutional neural

network neutrino event classifier. *Journal of Instrumentation*, 11(09): P09001–P09001, sep 2016. doi: 10.1088/1748-0221/11/09/p09001. URL `https://doi.org/10.1088/1748-0221/11/09/p09001`.

[43] A. Hoecker, P. Speckmayer, J. Stelzer, J. Therhaag, E. von Toerne, H. Voss, M. Backes, T. Carli, O. Cohen, A. Christov, D. Dannheim, K. Danielowski, S. Henrot-Versille, M. Jachowski, K. Kraszewski, A. Krasznahorkay Jr. au2, M. Kruk, Y. Mahalalel, R. Ospanov, X. Prudent, A. Robert, D. Schouten, F. Tegenfeldt, A. Voigt, K. Voss, M. Wolter, and A. Zemla. TMVA - Toolkit for Multivariate Data Analysis, 2009.

[44] Sijith Edayath. NC Visible Energy Correction. `https://nova-docdb.fnal.gov/cgi-bin/sso/RetrieveFile?docid=22508&filename=Ecorr_v3.pdf&version=3`, August 2017. URL `https://nova-docdb.fnal.gov/cgi-bin/sso/RetrieveFile?docid=22508&filename=Ecorr_v3.pdf&version=3`.

[45] Shiqi Yu and Zelimir Djurcic. Energy Reconstruction for 2020 ν_e Appearance Analysis. `https://nova-docdb.fnal.gov/cgi-bin/sso/RetrieveFile?docid=43814&filename=Technote_NueEnergy_2020%20%281%29.pdf&version=3`, May 2020. URL `https://nova-docdb.fnal.gov/cgi-bin/sso/RetrieveFile?docid=43814&filename=Technote_NueEnergy_2020%20%281%29.pdf&version=3`.

[46] P. Adamson et al. Search for active-sterile neutrino mixing using

neutral-current interactions in NOvA. *Phys. Rev. D*, 96(7):072006, 2017. doi: 10.1103/PhysRevD.96.072006.

[47] Louise Suter. Extrapolation techniques and systematic uncertainties in the noa muon neutrino disappearance analysis, 2015. URL `https://arxiv.org/abs/1511.00181`.

[48] Tom Carroll, Harry Hausner, Adam Lister, Brian Rebel, and Jennifer Thomas. Four-flavor oscillation fitting using the covariancematrixfit framework technote. `https://nova-docdb.fnal.gov/cgi-bin/sso/RetrieveFile?docid=47698&filename=orientation_5.pdf&version=3`, March 2020. URL `https://nova-docdb.fnal.gov/cgi-bin/sso/RetrieveFile?docid=47698&filename=orientation_5.pdf&version=3`.

[49] Gavin S. Davies Adam Aurisano and Brian Rebel. Executive Summary: Sterile Analysis - 2022, March 2022. URL `https://nova-docdb.fnal.gov/cgi-bin/sso/RetrieveFile?docid=54138&filename=Executive_Summary__Sterile_2022.pdf&version=1`.

[50] Luke Vinton. Sensitivity with custom neutrino energy binning and hadronic energy fraction binning, October 2016. URL `https://nova-docdb.fnal.gov/cgi-bin/sso/RetrieveFile?docid=16332&filename=NumuCollabMeeting_resBinning_energyBinShare_CustomBinning.pdf&version=2`.

[51] Xiangpan Ji, Wenqiang Gu, Xin Qian, Hanyu Wei, and Chao Zhang. Combined neyman–pearson chi-square: An improved approximation to the poisson-likelihood chi-square. *Nuclear Instruments and Methods in Physics Research Section A: Accelerators, Spectrometers, Detectors and Associated Equipment*, 961:163677, 2020. ISSN 0168-9002. doi: https://doi.org/10.1016/j.nima.2020.163677. URL `https://www.sciencedirect.com/science/article/pii/S0168900220302436`.

[52] Adam Lister. Covariancematrixfit: Mostly stats. `https://nova-docdb.fnal.gov/cgi-bin/sso/RetrieveFile?docid=40986&filename=2019-10-08-Covarianvce%20Matrix%20Fit_%20Mostly%20Stats%20%281%29.pdf&version=1`, October 2019. URL `https://nova-docdb.fnal.gov/cgi-bin/sso/RetrieveFile?docid=40986&filename=2019-10-08-Covarianvce%20Matrix%20Fit_%20Mostly%20Stats%20%281%29.pdf&version=1`.

[53] Gary J. Feldman and Robert D. Cousins. Unified approach to the classical statistical analysis of small signals. *Physical Review D*, 57 (7):3873–3889, apr 1998. doi: 10.1103/physrevd.57.3873. URL `https://doi.org/10.1103%2Fphysrevd.57.3873`.

[54] Glen Cowan, Kyle Cranmer, Eilam Gross, and Ofer Vitells. Asymptotic formulae for likelihood-based tests of new physics. *Eur. Phys. J. C Part. Fields*, 71(2):1–19, February 2011.

[55] M. A. Acero, B. Acharya, P. Adamson, L. Aliaga, N. Anfimov, A. Antoshkin, E. Arrieta-Diaz, L. Asquith, A. Aurisano, A. Back, C. Backhouse, M. Baird, N. Balashov, P. Baldi, B. A. Bambah, S. Bashar, A. Bat, K. Bays, R. Bernstein, V. Bhatnagar, D. Bhattarai, B. Bhuyan, J. Bian, A. C. Booth, R. Bowles, B. Brahma, C. Bromberg, N. Buchanan, A. Butkevich, S. Calvez, T. J. Carroll, E. Catano-Mur, A. Chatla, R. Chirco, B. C. Choudhary, S. Choudhary, A. Christensen, T. E. Coan, M. Colo, L. Cremonesi, G. S. Davies, P. F. Derwent, P. Ding, Z. Djurcic, M. Dolce, D. Doyle, D. Dueñas Tonguino, E. C. Dukes, A. Dye, R. Ehrlich, M. Elkins, E. Ewart, G. J. Feldman, P. Filip, J. Franc, M. J. Frank, H. R. Gallagher, R. Gandrajula, F. Gao, A. Giri, R. A. Gomes, M. C. Goodman, V. Grichine, M. Groh, R. Group, B. Guo, A. Habig, F. Hakl, A. Hall, J. Hartnell, R. Hatcher, H. Hausner, M. He, K. Heller, V Hewes, A. Himmel, B. Jargowsky, J. Jarosz, F. Jediny, C. Johnson, M. Judah, I. Kakorin, D. M. Kaplan, A. Kalitkina, J. Kleykamp, O. Klimov, L. W. Koerner, L. Kolupaeva, S. Kotelnikov, R. Kralik, Ch. Kullenberg, M. Kubu, A. Kumar, C. D. Kuruppu, V. Kus, T. Lackey, K. Lang, P. Lasorak, J. Lesmeister, S. Lin, A. Lister, J. Liu, M. Lokajicek, J. M. C. Lopez, R. Mahji, S. Magill, M. Manrique Plata, W. A. Mann, M. T. Manoharan, M. L. Marshak, M. Martinez-Casales, V. Matveev, B. Mayes, B. Mehta, M. D. Messier, H. Meyer, T. Miao, V. Mikola, W. H. Miller, S. Mishra, S. R. Mishra, A. Mislivec, R. Mohanta, A. Moren, A. Morozova, W. Mu, L. Mualem, M. Muether, K. Mulder, D. Naples, A. Nath, N. Nayak, S. Nelleri, J. K.

Nelson, R. Nichol, E. Niner, A. Norman, A. Norrick, T. Nosek, H. Oh, A. Olshevskiy, T. Olson, J. Ott, A. Pal, J. Paley, L. Panda, R. B. Patterson, G. Pawloski, D. Pershey, O. Petrova, R. Petti, D. D. Phan, R. K. Plunkett, A. Pobedimov, J. C. C. Porter, A. Rafique, L. R. Prais, V. Raj, M. Rajaoalisoa, B. Ramson, B. Rebel, P. Rojas, P. Roy, V. Ryabov, O. Samoylov, M. C. Sanchez, S. Sánchez Falero, P. Shanahan, P. Sharma, S. Shukla, A. Sheshukov, I. Singh, P. Singh, V. Singh, E. Smith, J. Smolik, P. Snopok, N. Solomey, A. Sousa, K. Soustruznik, M. Strait, L. Suter, A. Sutton, S. Swain, C. Sweeney, A. Sztuc, B. Tapia Oregui, P. Tas, B. N. Temizel, T. Thakore, R. B. Thayyullathil, J. Thomas, E. Tiras, J. Tripathi, J. Trokan-Tenorio, Y. Torun, J. Urheim, P. Vahle, Z. Vallari, J. Vasel, T. Vrba, M. Wallbank, T. K. Warburton, M. Wetstein, D. Whittington, D. A. Wickremasinghe, T. Wieber, J. Wolcott, M. Wrobel, W. Wu, Y. Xiao, B. Yaeggy, A. Yallappa Dombara, A. Yankelevich, K. Yonehara, S. Yu, Y. Yu, S. Zadorozhnyy, J. Zalesak, Y. Zhang, and R. Zwaska. The profiled feldman-cousins technique for confidence interval construction in the presence of nuisance parameters, 2022. URL `https://arxiv.org/abs/2207.14353`.

[56] M. G. Aartsen, K. Abraham, M. Ackermann, J. Adams, J. A. Aguilar, M. Ahlers, M. Ahrens, D. Altmann, K. Andeen, T. Anderson, I. Ansseau, G. Anton, M. Archinger, C. Argüelles, T. C. Arlen, J. Auffenberg, S. Axani, X. Bai, S. W. Barwick, V. Baum, R. Bay, J. J. Beatty, J. Becker Tjus, K.-H. Becker, S. BenZvi, P. Berghaus, D. Berley, E. Bernardini, A. Bernhard, D. Z. Besson, G. Binder, D. Bindig, E. Blaufuss, S. Blot, D. J.

Boersma, C. Bohm, M. Börner, F. Bos, D. Bose, S. Böser, O. Botner, J. Braun, L. Brayeur, H.-P. Bretz, A. Burgman, J. Casey, M. Casier, E. Cheung, D. Chirkin, A. Christov, K. Clark, L. Classen, S. Coenders, G. H. Collin, J. M. Conrad, D. F. Cowen, A. H. Cruz Silva, J. Daughhetee, J. C. Davis, M. Day, J. P. A. M. de André, C. De Clercq, E. del Pino Rosendo, H. Dembinski, S. De Ridder, P. Desiati, K. D. de Vries, G. de Wasseige, M. de With, T. DeYoung, J. C. Díaz-Vélez, V. di Lorenzo, H. Dujmovic, J. P. Dumm, M. Dunkman, B. Eberhardt, T. Ehrhardt, B. Eichmann, S. Euler, P. A. Evenson, S. Fahey, A. R. Fazely, J. Feintzeig, J. Felde, K. Filimonov, C. Finley, S. Flis, C.-C. Fösig, T. Fuchs, T. K. Gaisser, R. Gaior, J. Gallagher, L. Gerhardt, K. Ghorbani, W. Giang, L. Gladstone, T. Glüsenkamp, A. Goldschmidt, G. Golup, J. G. Gonzalez, D. Góra, D. Grant, Z. Griffith, A. Haj Ismail, A. Hallgren, F. Halzen, E. Hansen, K. Hanson, D. Hebecker, D. Heereman, K. Helbing, R. Hellauer, S. Hickford, J. Hignight, G. C. Hill, K. D. Hoffman, R. Hoffmann, K. Holzapfel, A. Homeier, K. Hoshina, F. Huang, M. Huber, W. Huelsnitz, K. Hultqvist, S. In, A. Ishihara, E. Jacobi, G. S. Japaridze, M. Jeong, K. Jero, B. J. P. Jones, M. Jurkovic, A. Kappes, T. Karg, A. Karle, U. Katz, M. Kauer, A. Keivani, J. L. Kelley, A. Kheirandish, M. Kim, T. Kintscher, J. Kiryluk, T. Kittler, S. R. Klein, G. Kohnen, R. Koirala, H. Kolanoski, L. Köpke, C. Kopper, S. Kopper, D. J. Koskinen, M. Kowalski, K. Krings, M. Kroll, G. Krückl, C. Krüger, J. Kunnen, S. Kunwar, N. Kurahashi, T. Kuwabara, M. Labare, J. L. Lanfranchi, M. J. Larson, D. Lennarz, M. Lesiak-Bzdak, M. Leuermann, L. Lu, J. Lüne-

mann, J. Madsen, G. Maggi, K. B. M. Mahn, S. Mancina, M. Mandelartz, R. Maruyama, K. Mase, R. Maunu, F. McNally, K. Meagher, M. Medici, M. Meier, A. Meli, T. Menne, G. Merino, T. Meures, S. Miarecki, E. Middell, L. Mohrmann, T. Montaruli, M. Moulai, R. Nahnhauer, U. Naumann, G. Neer, H. Niederhausen, S. C. Nowicki, D. R. Nygren, A. Obertacke Pollmann, A. Olivas, A. Omairat, A. O'Murchadha, T. Palczewski, H. Pandya, D. V. Pankova, J. A. Pepper, C. Pérez de los Heros, C. Pfendner, D. Pieloth, E. Pinat, J. Posselt, P. B. Price, G. T. Przybylski, M. Quinnan, C. Raab, M. Rameez, K. Rawlins, M. Relich, E. Resconi, W. Rhode, M. Richman, B. Riedel, S. Robertson, C. Rott, T. Ruhe, D. Ryckbosch, D. Rysewyk, L. Sabbatini, J. Salvado, S. E. Sanchez Herrera, A. Sandrock, J. Sandroos, S. Sarkar, K. Satalecka, P. Schlunder, T. Schmidt, S. Schöneberg, A. Schönwald, D. Seckel, S. Seunarine, D. Soldin, M. Song, G. M. Spiczak, C. Spiering, M. Stamatikos, T. Stanev, A. Stasik, A. Steuer, T. Stezelberger, R. G. Stokstad, A. Stößl, R. Ström, N. L. Strotjohann, G. W. Sullivan, M. Sutherland, H. Taavola, I. Taboada, J. Tatar, S. Ter-Antonyan, A. Terliuk, G. Tešić, S. Tilav, P. A. Toale, M. N. Tobin, S. Toscano, D. Tosi, M. Tselengidou, A. Turcati, E. Unger, M. Usner, S. Vallecorsa, J. Vandenbroucke, N. van Eijndhoven, S. Vanheule, M. van Rossem, J. van Santen, J. Veenkamp, M. Voge, M. Vraeghe, C. Walck, A. Wallace, N. Wandkowsky, Ch. Weaver, C. Wendt, S. Westerhoff, B. J. Whelan, K. Wiebe, L. Wille, D. R. Williams, L. Wills, H. Wissing, M. Wolf, T. R. Wood, E. Woolsey, K. Woschnagg,

D. L. Xu, X. W. Xu, Y. Xu, J. P. Yanez, G. Yodh, S. Yoshida, and M. Zoll. Searches for sterile neutrinos with the icecube detector. *Phys. Rev. Lett.*, 117:071801, Aug 2016. doi: 10.1103/PhysRevLett.117.071801. URL `https://link.aps.org/doi/10.1103/PhysRevLett.117.071801`.

[57] MicroBooNE Collaboration, P. Abratenko, R. An, J. Anthony, L. Arellano, J. Asaadi, A. Ashkenazi, S. Balasubramanian, B. Baller, C. Barnes, G. Barr, V. Basque, L. Bathe-Peters, O. Benevides Rodrigues, S. Berkman, A. Bhanderi, A. Bhat, M. Bishai, A. Blake, T. Bolton, J. Y. Book, L. Camilleri, D. Caratelli, I. Caro Terrazas, F. Cavanna, G. Cerati, Y. Chen, D. Cianci, G. H. Collin, J. M. Conrad, M. Convery, L. Cooper-Troendle, J. I. Crespo-Anadon, M. Del Tutto, S. R. Dennis, P. Detje, A. Devitt, R. Diurba, R. Dorrill, K. Duffy, S. Dytman, B. Eberly, A. Ereditato, L. Escudero-Sanchez, J. J. Evans, R. Fine, G. A. Fiorentini Aguirre, R. S. Fitzpatrick, B. T. Fleming, N. Foppiani, D. Franco, A. P. Furmanski, D. Garcia-Gamez, S. Gardiner, G. Ge, V. Genty, S. Gollapinni, O. Goodwin, E. Gramellini, P. Green, H. Greenlee, W. Gu, R. Guenette, P. Guzowski, L. Hagaman, O. Hen, C. Hilgenberg, G. A. Horton-Smith, A. Hourlier, R. Itay, C. James, X. Ji, L. Jiang, J. H. Jo, R. A. Johnson, Y. J. Jwa, D. Kalelo, D. Kalra, N. Kamp, N. Kaneshige, G. Karagiorgi, W. Ketchum, M. Kirby, T. Kobilarcik, I. Kreslo, R. LaZur, I. Lepetic, K. Li, Y. Li, K. Lin, A. Lister, B. R. Littlejohn, W. C. Louis, X. Luo, K. Manivannan, C. Mariani, D. Marsden, J. Marshall, D. A. Martinez Caicedo, K. Mason, A. Mastbaum, N. McConkey, V. Meddage, T. Mettler, K. Miller,

J. Mills, K. Mistry, T. Mohayai, A. Mogan, J. Moon, M. Mooney, A. F. Moor, C. D. Moore, L. Mora Lepin, J. Mousseau, M. Murphy, D. Naples, A. Navrer-Agasson, M. Nebot-Guinot, R. K. Neely, D. A. Newmark, J. Nowak, M. Nunes, O. Palamara, V. Paolone, A. Papadopoulou, V. Papavassiliou, S. F. Pate, N. Patel, A. Paudel, Z. Pavlovic, E. Piasetzky, I. Ponce-Pinto, S. Prince, X. Qian, J. L. Raaf, V. Radeka, A. Rafique, M. Reggiani-Guzzo, L. Ren, L. C. J. Rice, L. Rochester, J. Rodriguez Rondon, M. Rosenberg, M. Ross-Lonergan, B. Russell, G. Scanavini, D. W. Schmitz, A. Schukraft, W. Seligman, M. H. Shaevitz, R. Sharankova, J. Shi, J. Sinclair, A. Smith, E. L. Snider, M. Soderberg, S. Soldner-Rembold, S. R. Soleti, P. Spentzouris, J. Spitz, M. Stancari, J. St. John, T. Strauss, K. Sutton, S. Sword-Fehlberg, A. M. Szelc, W. Tang, K. Terao, M. Thomson, C. Thorpe, D. Totani, M. Toups, Y. T. Tsai, M. A. Uchida, T. Usher, W. Van De Pontseele, B. Viren, M. Weber, H. Wei, Z. Williams, S. Wolbers, T. Wongjirad, M. Wospakrik, K. Wresilo, N. Wright, W. Wu, E. Yandel, T. Yang, G. Yarbrough, L. E. Yates, H. W. Yu, G. P. Zeller, J. Zennamo, and C. Zhang. Search for an excess of electron neutrino interactions in microboone using multiple final state topologies, 2021. URL `https://arxiv.org/abs/2110.14054`.

[58] P. Abratenko, R. An, J. Anthony, L. Arellano, J. Asaadi, A. Ashkenazi, S. Balasubramanian, B. Baller, C. Barnes, G. Barr, V. Basque, L. Bathe-Peters, O. Benevides Rodrigues, S. Berkman, A. Bhanderi, A. Bhat, M. Bishai, A. Blake, T. Bolton, J. Y. Book, L. Camilleri, D. Caratelli, I. Caro

Terrazas, F. Cavanna, G. Cerati, Y. Chen, D. Cianci, G. H. Collin, J. M. Conrad, M. Convery, L. Cooper-Troendle, J. I. Crespo-Anadón, M. Del Tutto, S. R. Dennis, P. Detje, A. Devitt, R. Diurba, R. Dorrill, K. Duffy, S. Dytman, B. Eberly, A. Ereditato, J. J. Evans, R. Fine, G. A. Fiorentini Aguirre, R. S. Fitzpatrick, B. T. Fleming, N. Foppiani, D. Franco, A. P. Furmanski, D. Garcia-Gamez, S. Gardiner, G. Ge, V. Genty, S. Gollapinni, O. Goodwin, E. Gramellini, P. Green, H. Greenlee, W. Gu, R. Guenette, P. Guzowski, L. Hagaman, O. Hen, C. Hilgenberg, G. A. Horton-Smith, A. Hourlier, R. Itay, C. James, X. Ji, L. Jiang, J. H. Jo, R. A. Johnson, Y.-J. Jwa, D. Kalra, N. Kamp, N. Kaneshige, G. Karagiorgi, W. Ketchum, M. Kirby, T. Kobilarcik, I. Kreslo, I. Lepetic, K. Li, Y. Li, K. Lin, B. R. Littlejohn, W. C. Louis, X. Luo, K. Manivannan, C. Mariani, D. Marsden, J. Marshall, D. A. Martinez Caicedo, K. Mason, A. Mastbaum, N. McConkey, V. Meddage, T. Mettler, K. Miller, J. Mills, K. Mistry, A. Mogan, T. Mohayai, J. Moon, M. Mooney, A. F. Moor, C. D. Moore, L. Mora Lepin, J. Mousseau, M. Murphy, D. Naples, A. Navrer-Agasson, M. Nebot-Guinot, R. K. Neely, D. A. Newmark, J. Nowak, M. Nunes, O. Palamara, V. Paolone, A. Papadopoulou, V. Papavassiliou, S. F. Pate, N. Patel, A. Paudel, Z. Pavlovic, E. Piasetzky, I. D. Ponce-Pinto, S. Prince, X. Qian, J. L. Raaf, V. Radeka, A. Rafique, M. Reggiani-Guzzo, L. Ren, L. C. J. Rice, L. Rochester, J. Rodriguez Rondon, M. Rosenberg, M. Ross-Lonergan, G. Scanavini, D. W. Schmitz, A. Schukraft, W. Seligman, M. H. Shaevitz, R. Sharankova, J. Shi, J. Sinclair, A. Smith, E. L. Snider,

M. Soderberg, S. Söldner-Rembold, P. Spentzouris, J. Spitz, M. Stancari, J. St. John, T. Strauss, K. Sutton, S. Sword-Fehlberg, A. M. Szelc, W. Tang, K. Terao, C. Thorpe, D. Totani, M. Toups, Y.-T. Tsai, M. A. Uchida, T. Usher, W. Van De Pontseele, B. Viren, M. Weber, H. Wei, Z. Williams, S. Wolbers, T. Wongjirad, M. Wospakrik, K. Wresilo, N. Wright, W. Wu, E. Yandel, T. Yang, G. Yarbrough, L. E. Yates, H. W. Yu, G. P. Zeller, J. Zennamo, and C. Zhang and. Search for an anomalous excess of charged-current quasielastic ν_e interactions with the MicroBooNE experiment using deep-learning-based reconstruction. *Physical Review D*, 105(11), jun 2022. doi: 10.1103/physrevd.105.112003. URL `https://doi.org/10.1103%2Fphysrevd.105.112003`.

[59] MicroBooNE Collaboration, P. Abratenko, R. An, J. Anthony, L. Arellano, J. Asaadi, A. Ashkenazi, S. Balasubramanian, B. Baller, C. Barnes, G. Barr, V. Basque, L. Bathe-Peters, O. Benevides Rodrigues, S. Berkman, A. Bhanderi, A. Bhat, M. Bishai, A. Blake, T. Bolton, J. Y. Book, L. Camilleri, D. Caratelli, I. Caro Terrazas, F. Cavanna, G. Cerati, Y. Chen, D. Cianci, J. M. Conrad, M. Convery, L. Cooper-Troendle, J. I. Crespo-Anadon, M. Del Tutto, S. R. Dennis, P. Detje, A. Devitt, R. Diurba, R. Dorrill, K. Duffy, S. Dytman, B. Eberly, A. Ereditato, L. Escudero-Sanchez, J. J. Evans, R. Fine, G. A. Fiorentini Aguirre, R. S. Fitzpatrick, B. T. Fleming, N. Foppiani, D. Franco, A. P. Furmanski, D. Garcia-Gamez, S. Gardiner, G. Ge, S. Gollapinni, O. Goodwin, E. Gramellini, P. Green, H. Greenlee, W. Gu, R. Guenette, P. Guzowski, L. Hagaman, O. Hen,

C. Hilgenberg, G. A. Horton-Smith, A. Hourlier, R. Itay, C. James, X. Ji, L. Jiang, J. H. Jo, R. A. Johnson, Y. J. Jwa, D. Kalra, N. Kamp, N. Kaneshige, G. Karagiorgi, W. Ketchum, M. Kirby, T. Kobilarcik, I. Kreslo, R. LaZur, I. Lepetic, K. Li, Y. Li, K. Lin, A. Lister, B. R. Littlejohn, W. C. Louis, X. Luo, K. Manivannan, C. Mariani, D. Marsden, J. Marshall, D. A. Martinez Caicedo, K. Mason, A. Mastbaum, N. McConkey, V. Meddage, T. Mettler, K. Miller, J. Mills, K. Mistry, T. Mohayai, A. Mogan, J. Moon, M. Mooney, A. F. Moor, C. D. Moore, L. Mora Lepin, J. Mousseau, M. Murphy, D. Naples, A. Navrer-Agasson, M. Nebot-Guinot, R. K. Neely, D. A. Newmark, J. Nowak, M. Nunes, O. Palamara, V. Paolone, A. Papadopoulou, V. Papavassiliou, S. F. Pate, N. Patel, A. Paudel, Z. Pavlovic, E. Piasetzky, I. Ponce-Pinto, S. Prince, X. Qian, J. L. Raaf, V. Radeka, A. Rafique, M. Reggiani-Guzzo, L. Ren, L. C. J. Rice, L. Rochester, J. Rodriguez Rondon, M. Rosenberg, M. Ross-Lonergan, G. Scanavini, D. W. Schmitz, A. Schukraft, W. Seligman, M. H. Shaevitz, R. Sharankova, J. Shi, J. Sinclair, A. Smith, E. L. Snider, M. Soderberg, S. Soldner-Rembold, S. R. Soleti, P. Spentzouris, J. Spitz, M. Stancari, J. St. John, T. Strauss, K. Sutton, S. Sword-Fehlberg, A. M. Szelc, W. Tang, K. Terao, M. Thomson, C. Thorpe, D. Totani, M. Toups, Y. T. Tsai, M. A. Uchida, T. Usher, W. Van De Pontseele, B. Viren, M. Weber, H. Wei, Z. Williams, S. Wolbers, T. Wongjirad, M. Wospakrik, K. Wresilo, N. Wright, W. Wu, E. Yandel, T. Yang, G. Yarbrough, L. E. Yates, H. W. Yu, G. P. Zeller, J. Zennamo, and C. Zhang. Search for an anomalous excess of charged-current

ν_e interactions without pions in the final state with the microboone experiment, 2021. URL https://arxiv.org/abs/2110.14065.

[60] MicroBooNE Collaboration, P. Abratenko, R. An, J. Anthony, L. Arellano, J. Asaadi, A. Ashkenazi, S. Balasubramanian, B. Baller, C. Barnes, G. Barr, V. Basque, L. Bathe-Peters, O. Benevides Rodrigues, S. Berkman, A. Bhanderi, A. Bhat, M. Bishai, A. Blake, T. Bolton, J. Y. Book, L. Camilleri, D. Caratelli, I. Caro Terrazas, F. Cavanna, G. Cerati, Y. Chen, D. Cianci, J. M. Conrad, M. Convery, L. Cooper-Troendle, J. I. Crespo-Anadon, M. Del Tutto, S. R. Dennis, P. Detje, A. Devitt, R. Diurba, R. Dorrill, K. Duffy, S. Dytman, B. Eberly, A. Ereditato, J. J. Evans, R. Fine, G. A. Fiorentini Aguirre, R. S. Fitzpatrick, B. T. Fleming, N. Foppiani, D. Franco, A. P. Furmanski, D. Garcia-Gamez, S. Gardiner, G. Ge, S. Gollapinni, O. Goodwin, E. Gramellini, P. Green, H. Greenlee, W. Gu, R. Guenette, P. Guzowski, L. Hagaman, O. Hen, C. Hilgenberg, G. A. Horton-Smith, A. Hourlier, R. Itay, C. James, X. Ji, L. Jiang, J. H. Jo, R. A. Johnson, Y. J. Jwa, D. Kalra, N. Kamp, N. Kaneshige, G. Karagiorgi, W. Ketchum, M. Kirby, T. Kobilarcik, I. Kreslo, I. Lepetic, K. Li, Y. Li, K. Lin, B. R. Littlejohn, W. C. Louis, X. Luo, K. Manivannan, C. Mariani, D. Marsden, J. Marshall, D. A. Martinez Caicedo, K. Mason, A. Mastbaum, N. McConkey, V. Meddage, T. Mettler, K. Miller, J. Mills, K. Mistry, T. Mohayai, A. Mogan, J. Moon, M. Mooney, A. F. Moor, C. D. Moore, L. Mora Lepin, J. Mousseau, M. Murphy, D. Naples, A. Navrer-Agasson, M. Nebot-Guinot, R. K. Neely, D. A. Newmark, J. Nowak,

M. Nunes, O. Palamara, V. Paolone, A. Papadopoulou, V. Papavassiliou, S. F. Pate, N. Patel, A. Paudel, Z. Pavlovic, E. Piasetzky, I. Ponce-Pinto, S. Prince, X. Qian, J. L. Raaf, V. Radeka, A. Rafique, M. Reggiani-Guzzo, L. Ren, L. C. J. Rice, L. Rochester, J. Rodriguez Rondon, M. Rosenberg, M. Ross-Lonergan, B. Russell, G. Scanavini, D. W. Schmitz, A. Schukraft, W. Seligman, M. H. Shaevitz, R. Sharankova, J. Shi, J. Sinclair, A. Smith, E. L. Snider, M. Soderberg, S. Soldner-Rembold, P. Spentzouris, J. Spitz, M. Stancari, J. St. John, T. Strauss, K. Sutton, S. Sword-Fehlberg, A. M. Szelc, W. Tang, K. Terao, C. Thorpe, D. Totani, M. Toups, Y. T. Tsai, M. A. Uchida, T. Usher, W. Van De Pontseele, B. Viren, M. Weber, H. Wei, Z. Williams, S. Wolbers, T. Wongjirad, M. Wospakrik, K. Wresilo, N. Wright, W. Wu, E. Yandel, T. Yang, G. Yarbrough, L. E. Yates, H. W. Yu, G. P. Zeller, J. Zennamo, and C. Zhang. Search for an anomalous excess of inclusive charged-current ν_e interactions in the microboone experiment using wire-cell reconstruction, 2021. URL `https://arxiv.org/abs/2110.13978`.

[61] Haim Harari and Miriam Leurer. Recommending a standard choice of cabibbo angles and km phases for any number of generations. *Physics Letters B*, 181(1):123 – 128, 1986. ISSN 0370-2693. doi: https://doi.org/10.1016/0370-2693(86)91268-2. URL `http://www.sciencedirect.com/science/article/pii/0370269386912682`.

[62] P. Adamson et al. Search for Sterile Neutrinos Mixing with Muon

Neutrinos in MINOS. *Phys. Rev. Lett.*, 117:151803, October 2016. doi: 10.1103/PhysRevLett.117.151803. URL `https://link.aps.org/doi/10.1103/PhysRevLett.117.151803`.

[63] P. Adamson et al. First measurement of muon-neutrino disappearance in nova. *Phys. Rev. D*, 93:051104, March 2016. doi: 10.1103/PhysRevD.93.051104. URL `https://link.aps.org/doi/10.1103/PhysRevD.93.051104`.

[64] Samoil Bilenky. *Introduction to the Physics of Massive and Mixed Neutrinos*. Springer, 2010.

[65] J.J. Sakurai and J. Napolitano. *Modern Quantum Mechanics*. Cambridge University Press, 2017. ISBN 9781108527422.